Università degli Studi di Ferrara

Dottorato di Ricerca in
Fisica

Ciclo XXVI

Coordinatore: Prof. Guidi Vincenzo

Organic Light Emitting Transistors: A Platform for the Integration of Innovative Nanophotonic Structures

Settore Scientifico Disciplinare: FIS/01 Fisica Sperimentale

Dottoranda
Dott.ssa Cavallini Susanna

Tutore interno
Prof. Guidi Vincenzo

Tutori esterni
Dott. Toffanin Stefano

Dott. Muccini Michele

Anni 2010/2013

.. dedicated to Iohani

List of Publications

Journal articles

- **Low-threshold blue lasing from silk fibroin thin films**
  S. Toffanin, S. Kim, S. Cavallini, M. Natali, V. Benfenati, J. J. Amsden, D. L. Kaplan, R. Zamboni, M. Muccini and F. G. Omenetto
  Applied Physics Letters, **101**, 091110 (2012)

- **Organic light-emitting transistors with voltage-tunable lit area and full channel illumination**
  S. Toffanin, R. Capelli, W. Koopman, G. Generali, S. Cavallini, A. Stefani, D. Saguatti, G. Ruani and M. Muccini
  Laser and Photonics reviews, **7**, 1011 (2013)

- **Synthesis by MW-assisted direct arylation, side-arms driven self- assembly and functional properties of 9,10-dithienylanthracene materials**
  M. Melucci, M. Durso, C. Bettini, M. Gazzano, L. Maini, S. Toffanin, S. Cavallini, M. Cavallini, D. Gentili, V. Biondo, G. Generali, F. Gallino and R. Capelli
  Accepted to *Journal of Materials Chemistry C*

- **Selective MW-assisted surface chemical tailoring of hydrotalcites for fluorescent and biocompatible nanocomposites**
  T. Posati, M. Melucci, V. Benfenati, M. Durso, M. Nocchetti, S. Cavallini, S. Toffanin, A. Sagnella, A. Pistone, M. Muccini, G. Ruani and R. Zamboni
  Submitted to *Royal Society of Chemistry*

Proceedings of international conferences with acceptance based on full paper submission

- **Naturally Functionalized Silk as Useful Material for Photonic Applications**
  S. Cavallini, S. Toffanin, C. Chieco, A. Sagnella, A. Pistone, T. Posati, M. Natali, V. Benfenati, N. Di Virgilio, G. Ruani, M. Muccini, R. Zamboni and F. Rossi
  Conference proceeding for the 4^{th} *International Conference of natural fibres composites*

- **SILK.IT PROJECT: Silk Italian technology for industrial biomanufacturing**
  V. Benfenati, S. Toffanin, N. Di Virgilio, C. Chieco, A. Sagnella, S. Cavallini, T. Posati, A. Pistone, G. Varchi, G. Ruani, M. Muccini, F. Rossi and R. Zamboni
  Conference proceeding for the 4^{th} *International Conference of natural fibres composites*

Contents

List of Figures

LIST OF FIGURES

List of Tables

ASE	Amplified Spontaneous Emission
BC	Bottom Contact configuration
BG	Bottom Gate configuration
BO	Born-Oppenheimer approximation
CW	Continuous Wave
DBR	Distributed Bragg Reflectors
DFB	Distributed Feedback structure
EL	Electroluminescence
EQE	External Quantum Efficiency
FET	Field Effect Transistor
FWHM	Full Width at Half Maximum
HOMO	Higher Occupied Molecular Orbital
LCAO	Linear Combinations of Atomic Orbitals
LUMO	Lower Unoccupied Molecular Orbital
ML	Multilayers
MW	Molecular Weight
MO	Molecular Orbital
OEG	OptoElectronic Gate (dielectric)
OFET	Organic Field Effect Transistor
OLED	Organic Light Emitting Diodel
OLET	Organic Light Emitting Transistor
PL	Photoluminescence
PMA	Photonic Multichannel Analyzer
PMT	PhotoMultiplier Tube
PVD	Physical Vapor Deposition
RSF	Regenerated Silk Fibroin
SF	Superfluorescence
TC	Top Contact configuration
TG	Top Gate configuration
TIR	Total Internal Reflection
QY	Photoluminescence Quantum Yield
WF	Work Function

1

Introduction

Organic opto-electronic devices have been extensively studied in recent years, and are now used in circuits, displays and products for lighting (1).
They employ organic semiconductors, that are carbon-based materials having a solid state structure governed by weak *van der Waals* and dipole-dipole interactions.
These binding forces are different with respect to the strong cohesion forces found in inorganic semiconductors, and are responsible for most of their peculiar physical and mechanical properties in solid state; indeed, organic materials are flexible, processable at low temperatures, light weight and low cost (2).
Despite light-emission and charge transport performances are less developed with respect to inorganic materials, the versatility of the synthetic techniques and the wide gamut of available semiconducting compounds offer the possibility to increase the control of the device performances through an accurate molecular design and device engineering (3). Furthermore, many classes of organic compounds show multi-functional properties as they are capable of light emission and light sensing.
Intriguing devices based on such multifunctional properties are *Organic Light Emitting Transistors* (OLETs), that have attracted much attention in the last ten years given the high quantum-efficiency for light generation inherent to the device structure.
OLETs combine the switching properties of transistors with the emission properties of light-emitting diodes (4) (5); hence, they are considered excellent test systems to investigate physical processes such as charge-carrier injection, transport, and electroluminescence in organic semiconductors (6).
The research developed in this PhD thesis is focused on the investigation of light formation process and light extraction capability in non-standard architecture OLETs, aiming at fully disclosing the potentiality of OLETs in terms of external quantum effi-

ciency and brightness.
Firstly, a detailed study of the mechanisms that are responsible for light scattering and light loss in OLET device structure has been performed, and then suitable photonic structures to be inserted within device platform for enhancing light collection have been designed and fabricated. Indeed, it was exploited the ease of integration of photonic structures for light guiding, confinement and extraction into OLET planar architecture (7).
This kind of organic and hybrid nanopatterned photonic structures have aroused strong interest in recent years because they offer novel prospects for studying the interaction of light and matter (8), and they can be used to fabricate mirrors and non conventional optically-pumped lasers (9).
Given the recent results in the fabrication of bright, efficient and reliable devices, it is expected in the near future that the full compatibility of field-effect light-emitting devices with well established photonic planar technologies may allow the development of optical communication and integrated opto-electronic systems.
Moreover, the use of biocompatible and biodegradable materials in the realization of photonic structures is a fundamental step for the fabrication of multifunctional field-effect devices for optical sensing and biodiagnostics.

The thesis is organized as follow: Chapter 2 is a review of the basic electrical and optical properties of organic materials. The lasing action principles, with a brief mention on *Amplified Spontaneous Emission* (ASE) process in conjugated organic semiconductors are also described, followed by the introduction of the basic properties of one-dimensional photonic structures.
In Chapter 3 the working principles of *Organic Field Effect Transistors* are treated, and are introduced the emission properties of *Organic Light Emitting Transistors*, in an unique device configuration (named trilayer OLET) which allows to enhance the opto-electronic performances in terms of efficiency and brightness.
The study of the light formation and extraction in unprecedented full-channel illuminate trilayer OLETs is reported in Chapter 4. In this chapter it is also described the implementation of a specific planar photonic structure (*Distributed Bragg Reflector*) in order to control the directionality and emission wavelength of the device electroluminescence.
The manufacture of a *Distributed Feedback Laser* (DFB) obtained from suitably-doped natural biopolymer (silk) is reported in Chapter 5. The fabrication steps and photonic characterization of the biocompatible and biodegradable laser are discussed in details.

In the final part of the chapter, a new route for producing optically-active silk by direct feeding the silkworms with dye molecules is suggested.
In Chapter 6 are described the experimental setups used to investigate and characterize OLETs and photonic structures, and in Chapter 7 are reported the conclusions of this research.

Bibliography

[1] J.Zamuseil et al., *Adv.Mat.* **18**, 2708 (2006) 1

[2] A.Facchetti, *Mat.Today.* **10(3)**, 28 (2007) 1

[3] C.Reese et al., *Mat.Today.* **10(3)**, 20 (2007) 1

[4] J.Zamuseil et al., *J.App.Phys.* **103**, 064517 (2008) 1

[5] M.Muccini, *Nat.Mat.* **5**, 605 (2006) 1

[6] M.Muccini et al., *Laser Photonics Rev.* **6**, 258 (2012) 1

[7] E.B.Namdas et al., *Adv.Mater* **XX**, 1 (2011) 2

[8] R.Brückner et al., *Nat.Phot.* **6**, 322 (2012) 2

[9] J.Zamuseil et al., *Phys.Rew.A* **83**, 023801 (2011) 2

[10] V.Bulovic et al., *Science* **279**, 553 (1998)

[11] M.C.Gwinner et al., *Adv.Funct.Mater.* **19**, 1360 (2009)

2

Organic semiconductors

The term *organic semiconductors* denotes a class of semiconductors based on carbon. These materials exhibit attractive opto-electronic properties that are mainly due to the carbon atoms feature: in the ground state, its electronic structure is $1s^2 2s^2 2p^2$ with the two s electrons paired and the two p electrons unpaired.
Since the s orbitals are totally filled, a carbon atom should form only two bonds involving the electrons in $2p$ orbitals.

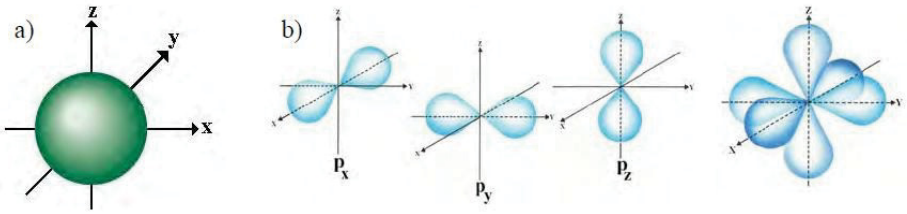

Figure 2.1: Representation of the spherical s orbital (a) and of the three p orbitals (b) with their original mutually orthogonal spatial combination.

Instead, carbon can be tetravalent and forms four bonds by mixing the $2s$ and the three $2p$ orbitals, creating a set of four equivalent degenerate orbitals and a different electronic configuration named hybridization sp^3. The additional energy required to place the four valence electrons in the tetrahedrally disposed sp^3 orbitals is provided by the energy gained in making four bonds to ligands around the carbon atom.
It is also possible for the s and p orbitals to combine to form three sp^2 orbitals (sp^2 hybridization). In this case, one of the three atomic p orbital remains unaltered, while the $2s$ orbitals mixes with the other p orbitals, resulting in three hybrids coplanar orbitals directed about 120°apart from each other, with the unaltered p orbital disposed perpendicularly to the sp^2 hybridization plane.

The bonds formed from the sp^2 orbitals of different carbon atoms are called σ-bonds, while the ones formed from the overlapping between unaltered p orbitals are called π-bonds.
There are fundamental differences between these two kinds of bonds: the σ-bond are typically very strong and generates highly localized electron density in the plane of the sp^2 orbitals. The σ-electrons are not involved in charge transport mechanism but form the skeleton of the structure, being responsible of the geometrical arrangement of the resulting molecule or polymer.
On the contrary, π-bonds are weaker and the electrons involved can freely move across the entire molecule, establishing a delocalized electron density above and below the nodal plane coinciding with the plane of the molecule.
The term *conjugated* refers to the alternating sequence of single and double bonds in the molecule; this term is usually used to indicate carbon-based compounds despite the fact that it is known that all the bonds length among the carbon atoms are essentially the same. The delocalization of the electron density enhance the stability of the molecule over what would be the case of conjugation (1).

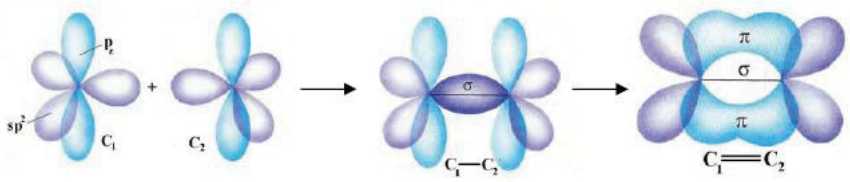

Figure 2.2: Formation of σ and π-bonds between two hybridized sp^2 carbon atoms.

2.1 Bohr-Oppenheimer approximation and Molecular Orbital theory

The macroscopic properties of a system can be deduced from its wavefunction Ψ obtained solving the Shrödinger equation:

$$H\Psi = E\Psi \tag{2.1}$$

Where H is the Hamiltonian operator, which is the sum of the energy operators terms of the system. This equation is exactly solvable only for hydrogen molecule; for other molecules, the wavefunction Ψ can be obtained using approximations.
The first one that is generally used is the Born-Oppenheimer (BO) approximation, that

derives from the fact that there is a large disparity between the electronic and nuclear masses, and assumes that the electrons can be considered to respond instantaneously to a change in the configuration of the nuclei, while the changes in the nuclei distance are almost negligible over the time period required to effect an electronic transition.
Within this approximation, the most studied mathematical method to analyze the energy levels of a molecule is the *Molecular Orbital* (MO) theory, that asserts that a molecule largely preserves the structure of the wavefunctions of its initial atoms, and thus it is possible to calculate a molecular wavefunction starting from a *Linear Combinations of Atomic Orbitals* (LCAO) (2).
Using the Bohrn-Oppenheimer separability condition, the total wavefunction Ψ_T of the molecule can be written as the product of the wavefunctions:

$$\Psi_T = \psi'_e \psi_v \psi_r \tag{2.2}$$

with the corresponding energy:

$$E_T = E_e + E_v + E_r \tag{2.3}$$

where the subscripts e, v and r refer to electronic, vibrational and rotational components, respectively (1).
In the simplest MO treatment of delocalized carbon systems, the total molecular electronic wavefunction is given as:

$$\psi'_e = \psi_\sigma \psi_\pi \tag{2.4}$$

with the wavefunctions containing the electrons constituting the σ-bond and those that form the π-bond, as explained previously.
Most of the electronic transitions from the filled to the unfilled levels involve π-electrons while the nuclei and the σ-electrons are considered to generate a fixed potential.
A wavefunction of a π-MO in the LCAO approximation can be written as:

$$\psi_\pi = \sum_{l=1}^{N} a_l \phi_l \tag{2.5}$$

where the ϕ_l terms are the atomic orbitals, and the a_l terms are the coefficients determined by minimizing the total energy of the system. The sum in Eq. 2.5 is over all N carbon atoms of the molecules, and the resulting N molecular wavefunctions have different a_l coefficients and can accommodate two electrons according to the Pauli's principle.

The filling of the levels is done according to increasing energy; when a molecule is in its ground state, the unfilled MO's are called *antibonding* MO's (π*-orbitals) and the occupied ones are called *bonding* MO's. A molecular excited state is formed by promoting one of the bonding electrons to an unfilled antibonding MO.

2.1.1 Energy levels of sold state molecular aggregates

The discussion of the energy levels of a molecule will be now extended to aggregates of molecules.

2.1.1.1 Physical dimer

The simplest molecular aggregate system that can be consider is a *physical dimer*, that indicates a special arrangement between two identical molecules, that are close to each other but do not form a chemical bond.
The ground-state electronic wavefunction of a dimer can be approximated as:

$$\Psi_G = \psi_1\psi_2 \tag{2.6}$$

where ψ_1 and ψ_2 are the ground state wavefunctions of the two molecules, that are assumed to be obtained through MO calculations.
Within the approximation of Eq. 2.6, the ground state energy is given by:

$$E_G = E_1 + E_2 + < \psi_1\psi_2|V_{12}|\psi_1\psi_2 > \tag{2.7}$$

where E_1 and E_2 are the energies corresponding to the monomer states ψ_1 and ψ_2, and the last term denotes the coulombic binding energy for the pair:

$$W =< \psi_1\psi_2|V_{12}|\psi_1\psi_2 > \tag{2.8}$$

with V_{12} that represents the intermolecular interaction energy.
Let us consider that ψ_1^* and ψ_2^* are the equivalent excited electronic molecular states; then, to a first approximation, both $\psi_1^*\psi_2$ and $\psi_1\psi_2^*$ have the same electronic energy if V_{12} is neglected.
For $V_{12}\neq 0$, instead, the energy of the two configurations are different between each other, and the difference depends on the interaction energy and therefore on the relative orientation of the molecules.
In the case of identical molecules, the dimer energies are given by:

$$E_\pm = E_1^* + E_2^* + W' \pm < \psi_1^*\psi_2|V_{12}|\psi_1\psi_2^* > \tag{2.9}$$

where W' is the coulombic energy of interaction of the charge distributions of the excited state of molecule 1 with the ground state of molecule 2, and the last term indicates the resonance interaction energy that determines the splitting between the two energy states:

$$J =< \psi_1^* \psi_2 | V_{12} | \psi_1 \psi_2^* > \tag{2.10}$$

as it is represented in Figure 2.3.
The corresponding stationary excited states are:

$$\Psi^*(E_\pm) = \frac{1}{\sqrt{2}}(\psi_1^* \psi_2 \pm \psi_1 \psi_2^*) \tag{2.11}$$

For these stationary states the excitation is shared between the two molecules, while if the excitation is initially localized on one molecule, then it will be transferred back and forth between the two molecules in a wavelike manner (1).

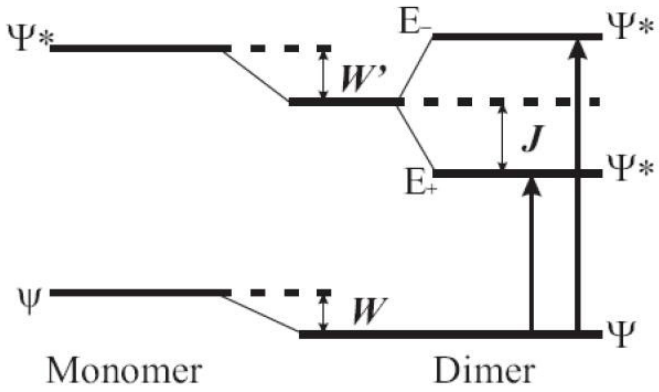

Figure 2.3: (left) Energy level scheme for the ground and first excited state of a monomer; (right) Energy levels for a physical dimer. The splitting of the first excited state correspond to 2xJ; single arrow lines indicate optical transitions.

2.1.1.2 Molecular crystals

A dimer can be extended to an array of identical molecules that represents a molecular crystal, in which a unit cell with N molecules is repeated in the three dimensions to generate the solid.
Assuming only electrostatic interactions, in the case of infinite number of molecules, in addition to a wavefunction Ψ_0 which indicates the product of ground state molecular wavefunctions, there is an infinite number of interacting electronically excited states.

Thus, a huge number of levels with different energies are present. These levels form a band, and the excitation energy that is initially localized to one molecule is shared between all the molecules in the crystal, to form a *crystal exciton band*.
From this simplified analysis emerges the concept of *exciton* as an electronically excited and mobile state of an insulating solid. This concept will be treated in Section 2.3.1.
Here, we extend the above mathematical description of a dimer for the case of a crystal with N molecules, h unit cells and $Z = N/h$ translational equivalent molecules. The basis functions for the exciton states can be written as:

$$\Psi_{ip}^{r} = \psi_{11}^{r}..\psi_{ip}^{r}..\psi_{hZ}^{r} \tag{2.12}$$

where ψ_{ip}^{r} denotes the excited state wavefunction of the *i-th* molecule in the *r-th* excited state and p refers to the class of translationally equivalent molecules.
The exciton wavefunctions can be constructed from linear combinations of functions Ψ_{ip}^{r}, taking into account the periodic boundary conditions. Indeed, the basis functions are multiplied by the phase factor $e^{i\mathbf{k}r}$ where $\boldsymbol{k}$ is the wavevector, that also label irreducible representations of the translation group.
Thus, exciton wavefunctions are:

$$\Psi_{i}^{r}(\mathbf{k}) = \frac{\sum_{p} e^{i\mathbf{k}r}\Psi_{ip}^{r}}{\sqrt{Z}} \tag{2.13}$$

The determinant must be solved in order to obtain the energy eingenvalues:

$$| < \Psi_{i}^{r}|V|\Psi_{j}^{r} > -(< \Psi_{G}|V|\Psi_{G} > +\Delta E)\delta_{ij}| = 0 \tag{2.14}$$

in which V is the electrostatic interaction operator and Ψ_G is the ground-state crystal eigenstate.
The determinant can be reduced in block form, and the following diagonal and off-diagonal elements result:

$$D^{r} + J_{ii}^{r} - \Delta E \qquad Diagonal \quad element \tag{2.15}$$

$$J_{ij}^{r} \qquad\qquad Off - Diagonal \quad element \tag{2.16}$$

which can be analytically determined (3):

$$D^{r} = \sum_{n}^{n\neq m} [(< \Psi_{m}^{r}\Psi_{n}|V_{mn}|\Psi_{m}^{r}\Psi_{n} >) - (< \Psi_{m}\Psi_{n}|V_{mn}|\Psi_{m}\Psi_{n} >)] \tag{2.17}$$

$$J_{ii}^{r} = \sum_{q}^{q \neq p} (< \Psi_{ip}^{r} \Psi_{iq} | V_{ip,iq} | \Psi_{ip} \Psi_{iq}^{r} >) \tag{2.18}$$

$$J_{ij}^{r} = \sum_{p} (< \Psi_{ip}^{r} \Psi_{jp} | V_{ip,jp} | \Psi_{ip} \Psi_{jp}^{r} >) \tag{2.19}$$

D^r is the electrostatic interaction energy that correspond to W' in the dimer case, J_{ii}^{r} is the sum of resonant coupling energies between translationally equivalent molecules, whereas J_{ij}^{r} refers to inequivalent ones.
The effect of diagonal and off-diagonal elements on the molecular levels of a crystal are represented in Figure 2.4.
The diagonal interaction elements J_{ii}^{r} form the exciton band, whereas the off-diagonal interaction elements J_{ij}^{r} are responsible for the excited state splitting (called *Davydov splitting*).
Thus, the Davydov splitting is due to translationally inequivalent molecules in the unit cell, whereas the mean energy displacement downwards depends on interactions between equivalent molecules. The width of each Davydov band depends on both types of intermolecular interactions.

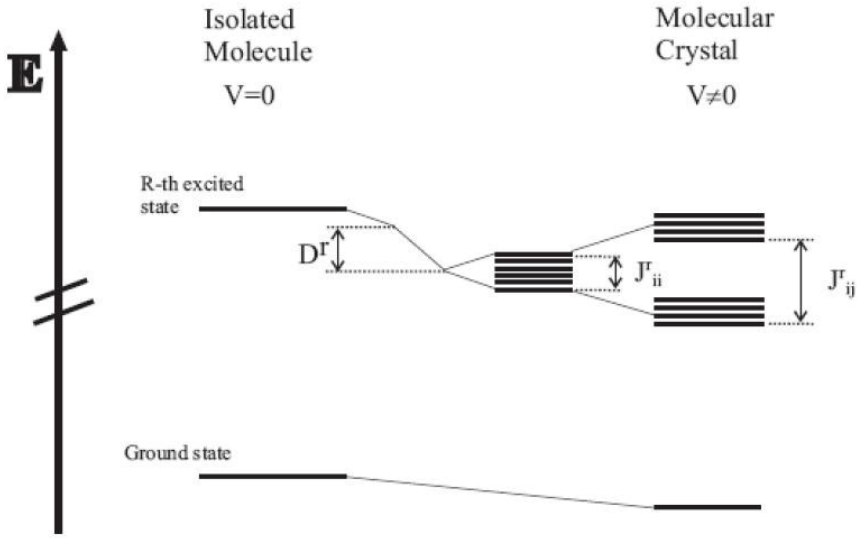

Figure 2.4: Energy level diagram for an isolated molecule and of the corresponding molecular crystal with two translationally inequivalent molecules per unit cell. The variation in energy of the ground and *r-th* excited state are displayed with the contribution of diagonal and off-diagonal elements.

2.2 Electrical properties of organic materials

In a molecular system, the filled level with the highest energy is called *Highest Occupied Molecular Orbital* (HOMO) and the lowest energy empty level is defined *Lowest Unoccupied Molecular Orbital* (LUMO); the energy difference between HOMO and LUMO is termed *band gap* energy.
In analogy with the inorganic semiconductor theory, the total set of occupied levels can be compared to the states of the valence band, while the set of unoccupied levels can be compared to states in the conduction band.
The difference with inorganics is due to the fact that for these materials, the next-neighbor interaction is strong due to strong chemical bondings, and thus the valence and conduction bands present energy widths of several electron volts; the strong binding interactions influence also their physical and mechanical properties, making inorganic materials rigid, brittle and reasonably stable to degradation processes with water and oxygen.
In contrast, the weak intramolecular interaction displayed in organic materials, that are held together principally by van der Waals forces and dipole-dipole interactions, leads to HOMO and LUMO orbitals which are mostly localized at the respective molecules, and show a bandwidth of around 0.1 eV (4). The weak molecule-molecule binding energy make organic materials flexible and lightweight, but less stable in ambient conditions; moreover, it is to be expected that the properties of the individual molecules and their spatial arrangement in the solid largely affect the macroscopic properties of the material.

We usually distinguish two main classes of organic semiconductors according to their *Molecular Weight* (MW). Low MW materials are usually named small molecules, whereas polymers are composed of a long molecular chain, and have a MW that reaches many thousands of g/mol.
On a microscopic scale, a thin film of a polymer often looks amorphous. The material can be disordered due to the irregular packing of the chains that can have twists, kinks, and defects; moreover, the functional side groups that are attached to the carbon backbone add further degree of freedom to the overall system.

2.2.1 Charge transport

It is possible to make a clear distinction between the charge transport in highly ordered organic single crystals and the one that occurs in amorphous films: in the first

case, charge transport can be described by *band-like transport*, whereas for amorphous films experimental data suggest *hopping* of charges through a distribution of localized states or shallow traps. Nevertheless, the exact nature of charge transport in organic semiconductors is still an open debate (5).

2.2.1.1 Band transport

When a very large number of strongly interacting molecules are brought together, the overlap of molecular wavefunctions is enough that energy levels become so closely spaced that they become indistinct. This lead to a description of those levels in terms of a family of continuous functions, called energy bands (6).
On the basis of the filling of the bands, solids can be divided into insulators, in which the highest occupied band is completely filled and the lowest unoccupied band is completely empty, and metals in which the conduction band is partly filled.
Semiconductors are a particular case of insulators in which, at nonzero temperature, an appreciable number of states at the top of the highest occupied band are empty and the equivalent number of states at the bottom of the lowest unoccupied band are filled.
Organic semiconductors are inherently insulators, that can be converted into a semiconductor if free charge carriers are generated by either injection, by doping, or by optical excitation.
In these materials, only if the interaction between nearest neighbor is sufficiently large with respect to others present in the system (such as the ones generated by dynamic and static disorder), the charge transport can take place through a band. In this case, the charge carrier delocalizes to form a propagating Bloch wave that may be scattered by phonons (lattice vibration) or impurities (7).
The simplest model for describing charge transport in bands is the Drude model, which assumes that the carriers are free to move under the influence of an applied electric field but subject to collisional damping forces.
According to this model, the velocity with which charge carriers move under the applied field, called mobility, can be defined as:

$$\mu = \frac{q\lambda}{m^* v_{th}} \tag{2.20}$$

in which q is the elemental charge, m^* is the charge effective mass, v_{th} is the electron thermal velocity and λ is the electron mean free path.
The temperature dependence of the mobility varies according to the nature of the scattering centers. However, in all cases it is found that the dependence follows the

general law:

$$\mu(T) \propto T^{-n} \tag{2.21}$$

with n positive in most practical cases so that the mobility increases when the temperature decreases.
Band transport in molecular crystals can only occur if the charge carrier mobility exceeds roughly $qa^2W = hkT$, where a is the lattice constant, and W is the bandwidth. If we consider $W \simeq 10\ kT$ and $a \simeq 1$ nm, band transport occurs when $\mu \simeq 10\ cm^2/Vs$ (7). This happen in very pure molecular crystals like naphthalene or perylene, where evidence of band transport is often claimed to be brought when is observed a temperature dependence of the mobility that follow Eq. 2.21 (8).
At higher temperatures, intra- and intermolecular vibrations destroy the coherence between adjacent sites and the transport is better explained by uncorrelated hops between a broad density of states (9).

2.2.1.2 Hopping

The previously described band transport model fails also to account for polarization. This phenomenon happens when a charge carrier residing on a molecular site tends to polarize also its neighbors; as a consequence there is a polarization cloud that moves together with the charge and the traveling charge is no longer a single entity, but a quasi-particle called *polaron*.
In order to estimate the stability of the polaron, two typical times are defined: the *residence time*, which corresponds to the average time a charge resides on a molecule, and the *electronic polarization time*, which is the time that the polarization cloud need to form around the charge.
Strong polarization effects characterize the electrical properties of organic solids since charges do not move so fast to prevent the polarization cloud to have time to form in the molecular site.
In these conditions, transport is allowed by the jump of the charge carriers from a molecule to its nearest neighbor or from one trap to the next.
There are different models for describing hopping transport, depending on how is characterized the density of localized states in between the carriers are moving.
For example, Bässler et al. have described it by a Gaussian distribution in which the width of the function is related to the spatial and energetic disorder within the material (10).

Another option is given by Vissemberg and Matters, that assumed an exponential distribution of states and a mobility that is dependent on the charge density (11). This model is an useful tool for describing transport in disordered semiconductors.
In the case of most molecular crystals, the deformation of the lattice induced by the charge is localized to nearest-neighbor molecules (*small polaron*) and the charge carrier can be viewed as residing in a potential well centered at the equilibrium position located at the energy minimum. Here, the stabilization energy associated with the polaron is maximized (12).
To move from one site to another, the polaron has to overcome an energy barrier as shown in Figure 2.5.

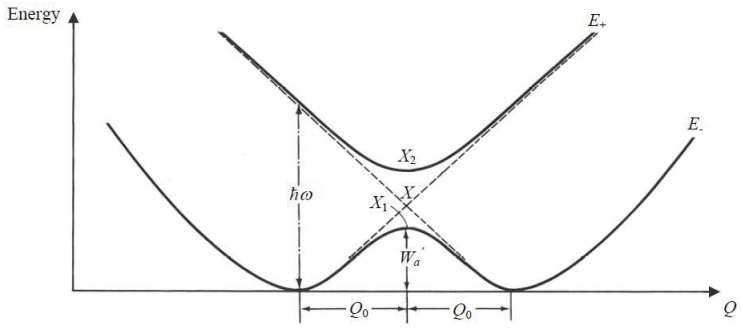

Figure 2.5: Energy of a small polaron in a two-site system as a function of the configurational coordinate Q. W_a' is the activation energy, ΔE the bandwidth and $\hbar\omega$ is the energy required for phonon assisted hopping (1).

It is appropriate to consider the motion as a sequence of uncorrelated hops. In these condition, the mobility is given by (13):

$$\mu(T) \propto \frac{qa^2}{kT} T^{-m} exp(-W_a'/kT) \tag{2.22}$$

where W_a' is a function of the spacing between hopping sites, a.
At low temperatures, the exponential term dominates Eq. 2.22 so that, in contrast to the prediction of band theory, mobility is expected to decrease sharply.
On the contrary, at high temperatures the pre-exponential T^{-m} dependence dominates the function as in the band transport theory. For this reason, in this range of temperatures it is difficult to differentiate band and hopping transport from their temperature-dependence.

These models are useful to describe the transport of charges in an organic material. However, the free charges are generally not present in the semiconductor, but have to be injected through contacts, as it will be shortly explained in the next section.

2.2.2 Charge injection

To inject carriers it is usually used a direct metal -semiconductor junction without any doping.
The starting point to describe the injection process is to define the energy difference between the respective Fermi energy levels of the isolated materials (the so called *built-in potential*, V_{bi}, see Figure 2.6).
When the the contact is made, equilibrium dictates that charge flows from one material to the other, until the Fermi levels align.

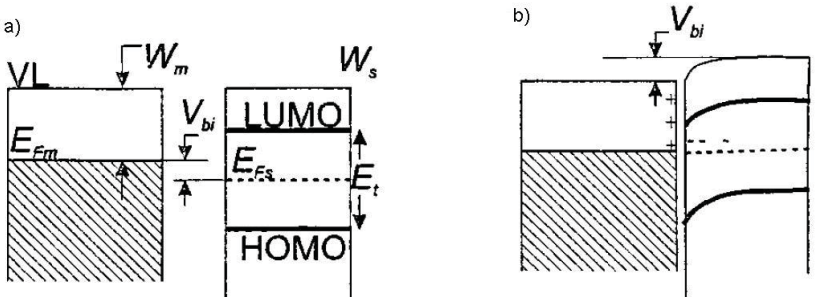

Figure 2.6: Formation of a metal-semiconductor contact. a) Non equilibrium situation before contact is made. All energies are referred to a common vacuum level, *VL*. The potential differences between Fermi energies (named built in potential, V_{bi}) is equal to the difference in the work functions, W_m and W_s. b) The case in which the vacuum levels align at the interface and the potential difference is accommodate across a charge depletion zone (15).

There are two extreme case to consider, depending on whether the transferred charge forms an interfacial dipole within the first molecular layers of the semiconductor, or occupies only dopant levels in the bulk.
The latter case can be treated as a Mott-Schottky barrier. In this condition, the vacuum levels align at the interface and the additional charge resides in a depletion zone created by ionizing donor or acceptor dopants; this charge causes band bending of the energy levels of the organic material, and the formation of the depletion zone obstructs further charges movements.
Comparing the *Work Functions* (WF) of the injecting metal with the HOMO/LUMO levels of a semiconductor can help to determine whether it is possible to obtain a good

ohmic contact with low contact resistance, or a potential barrier has to be expected with the consequence of poor charge injection.
Thus, the simple Mott-Schottky model can provide a guideline for choosing appropriate injection electrodes, but it is not sufficient to describe charge injection in organic semiconductors. In fact, in real experiments the condition of collision-free charge injection implied by Schottky theory is violated (7).
Hence, other charge injection models that take into account an additional interfacial dipole barrier, and that include thermally assisted tunneling have been proposed (16) (17) .

2.3 Linear optical properties of organic materials

In Section 2.1 we have seen that the properties of an isolated molecule can be deduced from its wavefunction Ψ_T, that can be divided into the product of the electronic, vibrational and rotational wavefunctions, as it is indicated in Eq. 2.2.
For a given electronic state, the vibrational levels represents vibrational states of increasing energies, that are of the order of 1000 cm^{-1} (near IR).
The energy range of the rotational components is $\simeq$ 10 cm^{-1} (far IR), whereas electronic transition energies are usually in the UV/visible region of the electromagnetic spectrum; that means that following the absorption of light, an electron can end up in a state of excitation.
The event of absorption of light involves the interaction of the electromagnetic field of the wave with the static and dynamic electrical components of the molecule, and it has a finite probability P_{if}^2 defined as:

$$P_{if}^2 \propto | < \Psi_i' | M | \Psi_f' > |^2 \tag{2.23}$$

where the subscripts refer to the initial and final states, and M is the dipole moment vector of the molecule.
The electronic wavefunction ψ_e' of Eq. 2.2 can be divided into two terms, non interacting between each other to a first order approximation:

$$\psi_e' = \psi_e \psi_s \tag{2.24}$$

The first term depends only on the spatial coordinates of the electron, and the other depends on the spin coordinates. Substituting Eq. 2.2 in Eq. 2.23, the probability of

exciting the molecule becomes:

$$P_{if}^2 \propto | < \psi_{ei}|M|\psi_{ef} > |^2 | < \psi_{vi}|\psi_{vf} > |^2 | < \psi_{si}|\psi_{sf} > |^2 \tag{2.25}$$

having ignored the rotational wavefunction.

In Eq. 2.25 the dipole moment operator appears only in the electronic term because the nuclei cannot respond to optical frequencies, and the spin is insensitive to electric field.

If any of the terms of Eq. 2.25 results zero, the optical transition will be forbidden. A forbidden transitions is defined according to *selection rules* and involves states of different multiplicity.

The multiplicity indicates the orientation of the angular spin momenta S in degenerate wavefunctions, and it is defined as $2S+1$; when the electrons are paired, the angular spin momentum $S=0$ and the multiplicity is equal to one (*singlet state*), while unpaired electrons have $S=1$ and multiplicity equal to three (*triplet state*).

Consequently, the singlet-singlet transition is spin allowed since an electron in an excited singlet state is paired to a second electron in the ground-state, whereas a triplet-singlet transition is forbidden.

2.3.1 Excited states of molecular aggregates

The discussion of excitation processes will be broaden at the case of aggregates of molecules.

The spectral changes that can be observed experimentally for aggregates are *i)* a spectral displacement of emission and absorption bands, *ii)* splitting of spectral lines and changes in polarization properties, *iii)* variation of the selection rules and *iv)* changes in molecular vibrational frequencies (1).

The collective response under excitation can be explained introducing a quasi-particle called *exciton*, that is a bound state of an electron (e^-) and an electron hole (h^+) which are held together by the electrostatic Coulomb force. This quantum of excitation can move on different molecular units in solids with proper long-range translational order.

We can distinguish two extreme type of excitons: a *Frenkel exciton* is an highly localized quasi-particle characterized by a a strong binding energy between the pair ($\simeq$ 1 eV); this kind of exciton is considered as a neutral particle that can diffuse from site to site, where e^- and h^+ are separated with a radius smaller than the intermolecular distance, typically ≤ 5 $\mathring{A}$.

The opposite case is represented by an exciton that is not restricted to excitations producing electrons and hole pairs located on the same molecular site, but where the

electron may be several molecules away from the hole. In this case, known as *Wannier exciton*, the binding energy between the pair reduces to about 10 meV and the exciton radius is more than an order of magnitude larger than the intermolecular separation, and ranges from 40 $\mathring{A}$ to 100 $\mathring{A}$.
An intermediate case occurs when the electron and the hole occupy adjacent molecules, and it is called *charge-transfer exciton*. This kind of exciton is neither very extended, nor tightly bond to a single molecular site.
Many theoretical and experimental works have underlined that in van der Waals solids the fundamental excitations are Frenkel excitons and charge-transfer excitons, whereas the Wannier excitons are more adequate to be used to describe the optical properties of inorganic semiconductors, in which the strong overlap between neighboring lattice atoms reduces the Coulombic interaction between the e^--h^+ pair.

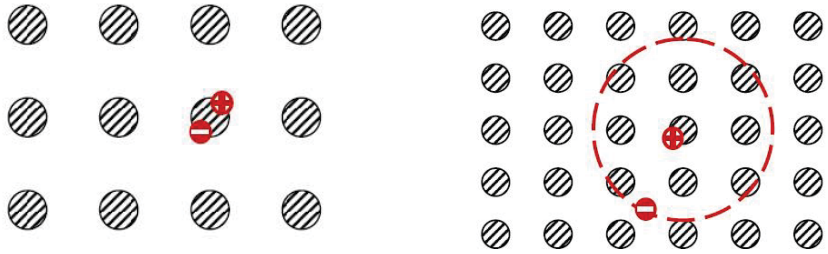

Figure 2.7: Schematic representation of Frenkel and Wannier excitons.

In real van der Waals solids, however, are present impurities, lattice imperfections and surface states that lead to the formation of more electronic energy states than the one described in the theory. Thus, electrons and holes can exist in a whole spectrum of energy states, from the tightly-bond e^--h^+ pair, through charge transfer and Wannier excitons, to surface charges, traps and free to move charge carriers.

2.3.1.1 Excitons generation, diffusion and relaxation

Exciton generation

There are various ways to generate excitons, but the most convenient is to excite a semiconductor with an electromagnetic wave.
Then, the excited state relaxes eventually to the ground state, and the time scale for the relaxation depends on the possibility that have the transition to a lower-lying level to take place.
To promote an electron into an higher state, the frequency of the exciting wave must be resonant with the energy gap of the material, with the right polarization in respect

to the transition dipole moments; moreover optical selection rules must be satisfied.
This is a limitation for the formation of excitons through direct optical excitation, since sometimes the desired state is a forbidden transition from the ground state, or the transition absorption coefficient is small.
Another option is to generate excitons in an electrical way by charge carriers recombination. This process involves the injection of electrons and holes in the material by means of electrodes, their diffusion in the presence of an electric field, exciton formation and charge recombination.
In this case both triplet and singlet exciton are created with a ratio 3/1, respectively, while in case of optical excitation only singlet exciton can be generated, since the transition to a triplet state from the ground state is in principle spin forbidden.
Light emission of electrically generated excitons is called *Electroluminescence* (EL), which is a process typically present in opto-electronic devices such as *Organic Light Emitting Diodes* (OLEDs) and transistors (OLETs), that will be described in Chapter 3.

Exciton diffusion

Excitons can transport energy without involving the migration of net electric charge; this process can be done via a *radiative transport*, where an exciton emits a photon that is absorbed in another part of the solid to create another exciton, or via different *non-radiative transport* processes.
The first one is defined *electromagnetic wave packed transport*, and is a coherent process useful to describe a situation where the exciton binding energy is large compared to the intermolecular hopping potential.
Coherence refers to the fact that the wavelength of light which is absorbed to create excitons is much larger than the lattice spacing, and therefore all the generated excitons initially have a well defined phase relationship.
For coherent transport, the time required to transfer energy from one molecule to the next is much shorter than the time it takes for the atomic nuclei to rearrange. The excitation motion is thus not accompanied by lattice distortion and the exciton can move over several molecular sites before being scattered in time τ_c, defined as the *coherence time* (21). This non radiative transport can happen in highly ordered single crystal, for which the typical values of the exciton diffusion coefficients are 10^{-3}-10^{-5} cm^2/s.
However, because of the interactions with defects, surface states and phonons, coherence may be lost.

For time greater that the coherence time the exciton is viewed as a localized excitation undergoing a random hopping-like motion, where it can experience sites with energy lower than the exciton band edge. In this case, if the thermal energy is not sufficient to promote the hopping, the exciton is trapped. Then it can relax with emission of radiation or with a non radiative pathway.
Another kind of exciton migration process imply a series of energy transfer via *resonant Förster dipole-dipole interaction.*
This is a long range process ($\leq$ 100 $\mathring{A}$) that involves one donor molecule D and one acceptor molecule A (see Figure 2.8), where the donor molecule have a fluorescence emission spectrum that overlaps with the absorption spectrum of the acceptor molecule. During the process, the excited donor transfers its energy to the acceptor, that in turn is promoted to an excited state:

$$D^* + A \rightarrow D + A^* \tag{2.26}$$

The process is primarily a result of dipole-dipole interactions between the donor and the acceptor; the spin of both the molecules are conserved, thus the triplet-singlet transition are in principle forbidden.

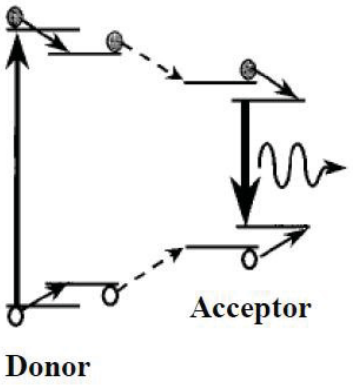

Figure 2.8: Energy level diagram of donor-acceptor system illustrating the excitation of acceptor molecules by means of non-radiative Förster energy transfer.

The rate of energy transfer depends upon the extend of the overlap of the emission spectrum of the donor with the absorption spectrum of the acceptor molecule, the relative orientation of the transition dipole moments and the distance between the molecules, as it is reported in the formula:

$$k_{ET}(R) = \frac{1}{\tau_D}\left(\frac{R_0}{R}\right)^6 \tag{2.27}$$

where R_0 defines the Förster radius, and τ_D the donor exciton lifetime for recombination in absence of quencher.
Generally, it is more convenient to use the observed donor lifetime τ instead of the natural lifetime τ_D. Since $\tau = \Phi_F \tau_D$ where Φ_F is the fluorescence yield of the donor in the absence of the acceptor, a new characteristic distance R_0' can be defined such that:

$$k_{ET}(R) = \frac{1}{\tau}\left(\frac{R_0'}{R}\right)^6 \tag{2.28}$$

where R_0' is the donor-acceptor distance at which the energy transfer probability is equal to the probability of de-excitation of D^* by means of radiative or radiationless decay processes.
For organic systems such as pyrene in naphthalene, typical values of R_0' are $\simeq 30$ $\mathring{A}$ (1).

Exciton radiative and non-radiative relaxation processes

In the absence of any chemical changes, an exciton returns to the ground state giving up its energy via *photoluminescence*, *phosphorescence* or heat.
These decay processes are represented in the Jablonski diagram (Figure 2.9).

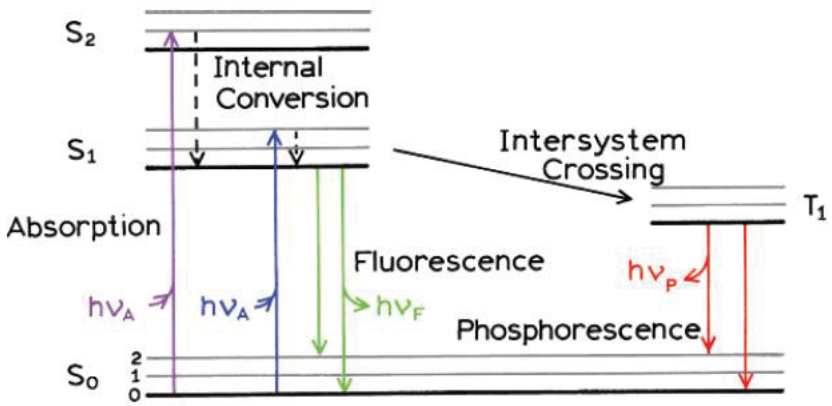

Figure 2.9: Representation of the Jablonsky diagram (18).

In the picture are also sketched the electronic states, represented with a bold line: S_0 is the fundamental, S_1 and S_2 are the first two singlet excited states whereas T_1 is the first triplet state; for any electronic state are drawn the vibrational levels (grey lines labeled v = 0,1,2..) representing vibrational states of increasing energy.
The transitions between states are depitched as vertical lines to illustrate the instantaneous nature of light absorption, that happens in about 10^{-15}s. This time is too short

for a significant displacement of nuclei, that during the transition are considered as being in a fixed position, according to the *Frank-Condon principle*.
Following light absorption, a fluorophore is excited to some higher vibrational level of either S_1 or S_2. With a few rare exceptions, molecules rapidly relax (in 10^{-12}s or less) to the lowest vibrational level of S_1; this process is called *internal conversion*.
From this level, according to the *Kasha's rule* (that states that photon emission occurs in appreciable yield only from the lowest excited state of a given multiplicity) the excited molecule can return to the fundamental state via a radiative decay called *fluorescence*, that occurs in a time range in between 10^{-6}s and 10^{-9}s.
Molecules can also undergo a spin conversion (*intersystem crossing*) to the first triplet state T_1; this internal relaxation can happen in between 10^{-11}s and 10^{-6}s.
Emission from T_1, named *phosphorescence*, is in principle forbidden since involves states of different multiplicity, but it can happen in molecules with high spin-orbit interaction; for this reason, phosphorescence lifetime are typically longer in respect to the fluorescence lifetime, and can vary from 10^{-3}s to seconds (19).
Phosphorescence emission occurs to a longer wavelength than those of fluorescence since the position of T_1 is at lower energy in respect to S_1. This is due to the fact that in a triplet state, where the electrons are located in different orbitals, the electron-electron repulsion is less than in a singlet state where electrons are paired in the same orbital. Hence, the position of the first excited singlet state always lyes at higher energy than that of the first excited triplet state.

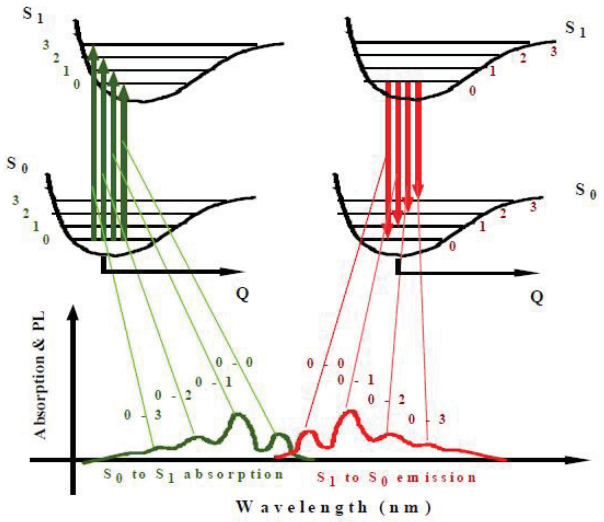

Figure 2.10: Frank-Condon diagram representing the potential energy surfaces associate with a given electronic state; the Q coordinate is the distance between nuclei (20).

According to the Frank-Condon principle, the nuclei dynamics is decoupled from that of electrons, since nuclei are enormously heavy compared to electrons. For this reason, it can be approximated that nuclei rearrange themselves in the excited state geometry after absorption takes place, and this readjustment brings them into vibration. This process is illustrated by the potential energy diagrams reported in Figure 2.10.
The arrows connecting all the vibrational levels and sublevels of the ground and the excited states sketched in picture 2.10 indicate that the absorption and the fluorescence processes are going to be practically continuous all over the bands. In the case of small displacement of the nucleus position, this is going to result in the absorption and the emission bands that are mirror images, with the emission band displaced to lower energies. The energy difference between the 0-0 in absorption and in emission is called *Stokes shift*.

In addition to the already described processes of internal conversion and intersystem crossing, radiationless deactivation pathway can be due to other unimolecular processes like auto-ionization or dissociation of the molecule.
Moreover, bimolecular processes that involve the interaction of the mobile exciton with free or trapped excitons, with a foreign molecule or with crystal defects might affect the lifetime of the excited state.
To define how efficiently a fluorophore is emitting and to quantify the ratio of radiative and non radiative transition rates it is used the *photoluminescence Quantum Yield*:

$$\Phi_{QY} = \frac{k_r}{k_r + k_{nr}} \tag{2.29}$$

k_r indicates the rate constant of the radiative processes and k_{nr} of the non radiative ones. These rates are defined as the inverse of the photoluminescence lifetime τ, that is the average time available for a molecule to spend in an excited state:

$$\tau = \frac{1}{k_r + k_{nr}} \tag{2.30}$$

2.4 Laser action principles in organics

In the previous sections, we have discussed the electrical and optical properties of molecules and aggregates of organic molecules, introducing the concept of excitons and describing the exciton relaxation processes. Now we can consider the role played by these radiative processes in lasers.

The first theoretical proposal of *Light Amplification by Stimulated Emission of Radiation* (LASER) occurred in 1958, and the subsequent experimental demonstration of an optically pumped laser made with ruby was obtained in 1960 (22) (23).
Two years later, Keyes and Quist were the first to report that electrical power could be converted into radiation by the injection of carriers at a Ga/As *p-n* junction; this was followed by the observation of coherent laser emission (24).
Since that moment, laser fabrication techniques have advanced very rapidly, and nowadays the development of new type of lasers is one of the major research activity around the world.
Organic semiconductor are a class of material attracting considerable attention in this research field, since they can offer tunability of the emission wavelength through the control of the chemical structure. Many of these materials are plastics, and can combine the scope for simple shaping and manufacturing of plastics with favourable optoelectronic properties such as high solid state photoluminescence quantum yield, strong absorption and gain and broad spectra (25). Moreover, organic materials are suitable for the realization of novel lasing structure as microcavity and *Distributed Feedback* (DFB) structures (26).

2.4.1 Absorption, stimulated and spontaneous emission

To introduce the basic principles of lasing emission, let us consider we have a material with two energy levels E_1 and E_2. For simplicity we will assume that E_1 is the ground level, and that all the molecules are initially in the ground state so that they will remain in this level unless some external stimulus is applied to the material.
The optical transition this material can undergo are *stimulated absorption* and two possible radiative emissions: *spontaneous* or *stimulated* (27).
Stimulated absorption can occur when the material absorbs a photon of energy $h\nu$= E_2 - E_1, where h is Plank's constant and ν the frequency of the incoming photon.
The probability per second of stimulated absorption, dP_{12}/dt, is proportional to the number of photons of energy $h\nu$ per unit of volume:

$$\frac{dP_{12}}{dt} = B_{12}N_1\rho(\nu) \tag{2.31}$$

where B_{12} is the Einstein coefficient for induced absorption, N_1 is the ground state population and $\rho(\nu)$ is the spectral energy density of the radiation field, that depends on the electronic wavefunctions of the two involved energy levels.
An excited molecule in the state E_2 may also spontaneously convert its excitation energy into an emitted photon $h\nu$. This radiation is emitted in an arbitrary direction

$\boldsymbol{k}$, and its probability is dependent on the structure of the molecule and on the selected transition $E_2 \rightarrow E_1$, but it is independent on the external radiation field:

$$\frac{dP_{21}^{spont}}{dt} = A_{21}N_2 \tag{2.32}$$

The constant factor A_{21} is the Einstein coefficient for spontaneous emission. Light produced in this process is random in space and time (*incoherent*).
An interesting event occurs when a photon of energy $h\nu$ impinges on a molecule while it is still in the excited state. In this case, the molecule is immediately stimulated to make its transition to the ground state and gives off another photon of the same wavelength, in phase with the incident radiation. This process is called stimulated emission, and it is the main mechanism for lasing.
The probability of stimulated emission is given by:

$$\frac{dP_{21}}{dt} = B_{21}N_2\rho(\nu) \tag{2.33}$$

where the constant factor B_{21} is the Einstein coefficient for stimulated emission.
This process has two interesting properties: first, one photon in input is needed and it becomes two photons in output (*optical gain*). Second, the two photons are in phase, and the light output is coherent.
This is a fundamental difference with the case of spontaneous emission, where the photons are incoherent. Moreover, in the case of stimulated emission, the incident wave determines the direction of the emitted wave, and the emission is not isotropic.
Now, we can find out the relationship between the Einstein coefficients.
According to Planck's distribution, the spectral energy density $\rho(\nu)$ can be written as:

$$\rho(\nu) = \frac{8\pi h\nu^3}{c^3}\frac{1}{e^{h\nu/kT} - 1} \tag{2.34}$$

where k is the Boltzmann constant and c the speed of light.
In equilibrium, the ratio of electron concentrations residing in states E_1 and E_2 are related to their energies given by the Boltzmann statistics:

$$\frac{N_2}{N_1} = e^{-\Delta E/kT} = e^{-h\nu/kT} \tag{2.35}$$

Since the radiation is stationary, the absorption rate must be the same as the emission rate:

$$B_{12}N_1\rho(\nu) = [B_{21}\rho(\nu) + A_{21}]N_2 \tag{2.36}$$

Substituting Eq. 2.34 into Eq. 2.36 we obtain:

$$\frac{8\pi h\nu^3}{c^3[e^{-h\nu/kT}-1]}\frac{A_{21}}{B_{12}e^{h\nu/kT}-B_{21}} \tag{2.37}$$

In order that this equation holds for all temperatures, the conclusion is that the probability of induced emission is equal to that of induced absorption:

$$B_{12} = B_{21} \tag{2.38}$$

On the contrary, the relationship between induced and spontaneous emission is given by:

$$A_{21} = \frac{8\pi h\nu^3}{c^3}B_{21} \tag{2.39}$$

In laser action, the spontaneous emission for incoherent light is weak and it can be ignored. The net optical output is given by stimulated emission minus the absorption:

$$B_{21}N_2\rho(\nu) - B_{12}N_1\rho(\nu) = (N_2 - N_1)B_{21}\rho(\nu) \tag{2.40}$$

It is seen here that the net optical gain is positive only if $N_2 > N_1$, a condition that is called *population inversion*, so that there is more population in the excited state than in the ground state.
According to Eq. 2.35 population inversion does not occur naturally under thermal equilibrium (28). Some external mean is needed to create this state, but even under strong pumping condition, it is physically impossible to achieve it in a system with only two energy levels, since in that case the population will be equally divided between E_1 and E_2.
A material in which is possible to obtain population inversion is called *active material*, and possess at least three available energy levels (29).

2.4.2 Basic elements of lasers

In addition to the active material, two other components are needed to build a laser: the optical resonator and the energy pump.
The resonator is useful to obtain optical feedback, and usually it is composed of two opposite mirrors, one which is made partially transparent so that output light can be extracted.
The pump selectively puts energy into the active medium, and generates a population distribution *N(E)* that deviates from the Boltzmann distribution that exists at thermal

equilibrium.
At sufficiently high pump power, population inversion is reached and the population density of an upper level, N_3, exceeds the one of a lower level, N_2. In this condition, the induced emission rate $B_{32}N_3\rho(\nu)$ for the transition $E_3 \rightarrow E_2$ exceeds the absorption rate $B_{23}N_2\rho(\nu)$.
Thus, an electromagnetic wave passing through this active medium is amplified instead being attenuated, according to the formula:

$$\alpha_{23}(\nu) = \sigma_{23}(\nu)[N_2 - (g_2/g_3)N_3] \tag{2.41}$$

where α_{23} $[cm^{-1}]$ is the absorption coefficient for the transition $E_2 \rightarrow E_3$, σ_{23} $[cm^2]$ represents the absorption cross section and g_2, g_3 are the levels statistical weights.
When this active medium is placed between two mirrors, the wave is reflected backward and forward traversing the amplified medium many times, and thus increasing the total amplification. Moreover, the resonator selects the emission wavelength that is concentrated within few resonant modes, the ones that are allowed to form a stationary wave.
It is possible to calculate the total gain factor per single round trip:

$$G(\nu) = e^{-2\alpha(\nu)L} \tag{2.42}$$

where L is the length of the resonator.
This formula does not take into account the losses of the process, that can be due to the reflectivity of the mirrors that reflect only a fraction of the incident wave, to self-absorption operated by the active medium, scattering of light and dust.
All these factors can be summarized in a *loss coefficient* γ which gives the fractional energy loss per round trip. If we assume the losses are equally distributed along the resonator length, the intensity of light I decrease as:

$$I = I_0 e^{-\gamma} \tag{2.43}$$

The previous relationship implies that, to obtain amplification, the gain has to overcomes the losses per round trip:

$$2\alpha(\nu)L > \gamma \tag{2.44}$$

Substituting in Equation 2.44 the absorption cross section from Equation 2.41, we

find the threshold condition for lasing emission:

$$\Delta N_{th} = \frac{\gamma}{2\sigma(\nu)L} \tag{2.45}$$

Equation 2.45 states that, when the population on the upper level is larger than ΔN_{th} with respect to the one on the lower level, a wave that is reflected between the mirrors is amplified.
Thus, lasing emission starts with a spontaneous emission from an excited atom in the active medium and, above the threshold, creates a photon avalanche which grows until the depletion of the population inversion is reached (30).

2.4.3 Optically-pumped organic laser

Actually, an increasing number of optically-pumped organic lasers have been successfully developed, for example dye lasers, where the active material is constituted of an highly fluorescent small molecule that is dispersed in a polymeric matrix.
It seems possible to use both fluorescence and phosphorescence processes to obtain laser emission, but in phosphorescence process triplet-triplet absorption bands are generally very broad, and the probability that they will overlap with the phosphorescence emission band introducing self absorption is very high.
Moreover, a transfer process can happen from the triplet excited state to the triplet ground state of oxygen that is present in the film; oxygen is a very reactive molecule that can favor the quenching of dye emission.
For these reasons, all the effort has gone into building an organic laser exploiting the fluorescence emission.
In general, by implementing organic small-molecules and polymers as active materials, the population inversion can be reached between the first two singlet levels, as it is sketched in Figure 2.11 (b).
The transition from the excited vibrational levels of S_1 to the ground level of S_1 is much faster than the transition from S_1 to some vibrational state in S_0; moreover, these vibrational states of S_0 will also depopulate very fast to the bottom of the ground state. This difference in decay rates likely suitable to achieve population inversion between the bottom of the S_1 state and the vibrational levels in S_0.

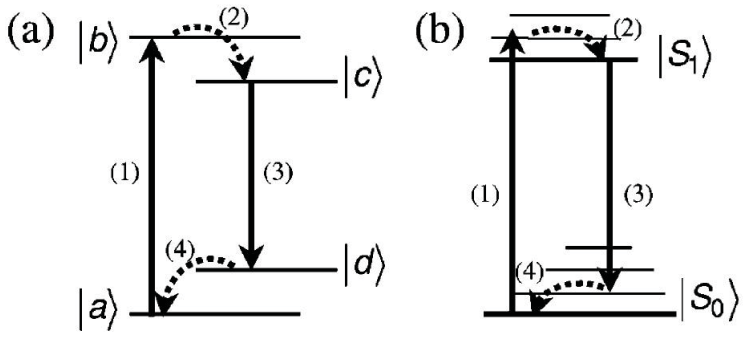

Figure 2.11: Energy level diagrams for optical gain media: a) for a generic four-level system; b) for an organic semiconductor. Transitions 1 and 3 are optical absorption and emission, whereas 2 and 4 are thermal relaxations. Lasing emission in organic materials occurs from the bottom of the S_1 state to a vibrational level in S_0 (25).

2.5 Superfluorescence and Amplified Spontaneous Emission

Superfluorescence (SF) and *Amplified Spontaneous Emission* (ASE) are two phenomena that present some optical and spectroscopic characteristics similar to lasing. They are collective processes related to phase-coherent light amplification (32).
The SF process starts at time t=0 by ordinary spontaneous emission, where the oscillating dipoles of the emitters present random phases. Then, the field arising from spontaneous emission induces phase correlation between the ensembles of the emitters and the systems evolves toward a state of correlated emission.
The relation 2.46 gives the limiting condition for this process to take place:

$$\frac{L}{c} < T_c < T_1, T_2 \tag{2.46}$$

L being the active volume length c the speed of light and T_c the self-induced correlation time of SF. T_1 is the spontaneous decay time and T_2 the dephasing time.
The duration of the process can be short compared with the upper-state lifetime of a single atom (shorter than that of normal fluorescence).
In the ASE case, coherent light amplification is given by the single pass amplification of photons gaining intensity by transversing the active volume of an inverted medium.
It is possible to distinguish between SF and ASE processes, since SF can only build up for very short excitation pulses ($\sim$ 100 fs) that keep the phase correlation.
Moreover, in the case of ASE the process does not require close proximity and coherent excitation, and it is based only on fluorescence and stimulated emission.

ASE is dependent on the film thickness and on the size of the excitation area: furthermore, the emitted light can have an high degree of polarization and the process usually doesn't have a clear threshold behavior (35).
ASE emission will results in a sharp peak with a *Full Width at Half Maximum* (FWHM) of about 10 nm, that occurs around the wavelength where the gain of the material is maximum.
This phenomenon can also be confused with lasing, since it can acquire many properties of laser light such as narrower linewidth, polarization and directionality.
The differences are due to the fact that in lasing light *i)* the spectral line narrowing coincides with resonant cavity modes selected by the resonator, *ii)* the FWHM of the peak is $\leq$ 1nm and *iii)* the output power has a non linear dependence on the input power, with a kink at the lasing threshold as it is shown in Figure 2.12.
The fulfillment of all these conditions, together with the generation of spatially and temporally coherent light, are used to define laser emission (36).

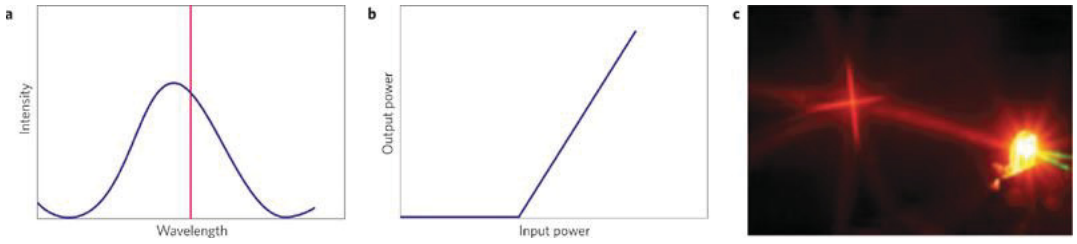

Figure 2.12: Output characteristic of a laser: a) the light output changes from a broad spectrum below threshold (blue) to a narrow line (red) above threshold; b) the output power has a non-linear dependence on the imput power; c) the light emission is a beam (36).

2.6 Photonic structures

The description made in the previous sections has underlined that the implementation of cavity is a fundamental step in the realization of a laser.
However, besides the conventional laser cavities made of two mirrors, there is the possibility to obtain optically pumped lasers using a wide variety of different resonant structures, including microscopic resonators, planar, cylindrical, and spherical microcavities, optical waveguide based cavities, and a remarkable range of diffractive structures.
While some of them appear quite different from the generic cavities, their basic function in providing resonant feedback through the gain medium is fundamentally the same.

The different geometries of these cavities, however, can be used to produce highly efficient devices that show a rich variety of spectral and spatial properties.

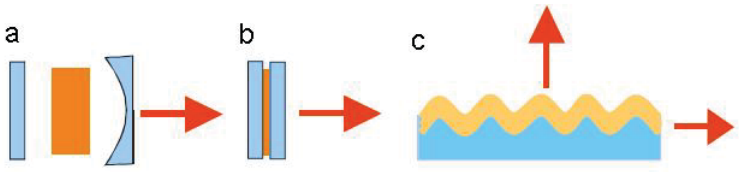

Figure 2.13: Examples of resonant structures: a) external cavity; b) planar microcavity; c) Distributed Feedback structure. The red arrows represent the laser emission.

Two interesting structure that have been intensively studied in my research are *Distributed Feedback lasers* (DFB) and *Distributed Bragg Reflectors* (DBR), that are 1-D photonic crystals that can modify the propagation of light.
A photonic crystal can be defined as the optical analogues of a semiconductors, where the periodicity in the atomic potential generates an electronic band gap. In a photonic structure, the periodic variation of the refractive index on a length scale comparable to the wavelength of interest, can generate a photonic band gap and forbid the propagation of photons.

2.6.1 Generation of a photonic band gap

A rigorous mathematical treatment is required to account for the opening of a photonic band gap (37).
This is an effect associated with the propagation of the electromagnetic radiation in a periodic media and it can be treated expanding the electromagnetic fields in plane waves and solving the Maxwell equations.
To analyze the problem, let us consider a non magnetic dielectric system ($\mu_r = 1$), in which free charges and polarization charges are absent ($\rho_{tot} = 0$).
After some algebra, the electric field $\boldsymbol{E}$ deduced by Maxwell equations can be reduced to the wave equation:

$$\nabla^2 \mathbf{E} = \left(\frac{\omega^2}{c^2}\right) \varepsilon \frac{\partial^2 \mathbf{E}}{\partial t^2} \tag{2.47}$$

were $\varepsilon = \varepsilon_0 \varepsilon_r$ is the dielectric function of the material. The equation for the magnetic field $\boldsymbol{H}$ can be deduced using the same formalism.
The solutions of Eq. 2.47 in free space are of the form:

$$\mathbf{E}, \mathbf{H} \sim e^{i(\mathbf{k}\,\mathbf{r} - \omega t)} \tag{2.48}$$

and establish the correlation between angular frequency of photons ω and wave vector $\boldsymbol{k}$ (38).
In a non absorbing material that is periodic in one direction (as the one illustrated in Figure 2.14) the dielectric function results $\varepsilon_r(x) = \varepsilon_r(x+a)$, where a is the lattice constant of the periodic media.
Thus, $\varepsilon_r(x)$ can be expanded in a Fourier series as follows:

$$\varepsilon_r(x) = \sum_{m=-\infty}^{\infty} k_m e^{i2\pi m x/a} \tag{2.49}$$

where m is an integer and k_m are the Fourier coefficients.
Given the periodicity of $\varepsilon_r(x)$, the problem may be solved in the context of Bloch-Floquet theorem, and the electric field can be written as (39):

$$E(x,t) = E_k(x,t) = u_k(x)e^{i(kx-\omega t)} \tag{2.50}$$

where $u_k(\mathrm{x}) = u_k(\mathrm{x}+\mathrm{a})$ is the periodic Bloch function.

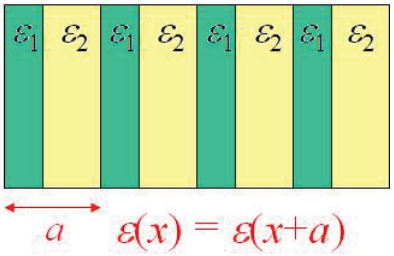

Figure 2.14: 1D photonic crystal formed by a stack of two different materials with dielectric constants ε_1 and ε_2, respectively. The optical axis is along the x direction while a is the lattice constant.

Here we skip the details of calculation, that are properly developed in Ref.(40), and we report the resulted eigenfrequencies $\omega_\pm$ obtained introducing the periodic dielectric function ε_r and the electric field E into a scalar wave equation:

$$\omega_\pm \approx \frac{\pi c}{a}\sqrt{k_0 \pm |k_1|} \pm \frac{ac}{\pi|k_1|}\left(k_0^2 - \frac{|k_1|^2}{2}\right)\left(k - \frac{k}{a}\right)^2 \tag{2.51}$$

as far as $(k-\pi/a)^2 \ll \pi/a$, there is no mode in the interval:

$$\frac{\pi c}{a}\sqrt{k_0 - |k_1|} < \omega < \frac{\pi c}{a}\sqrt{k_0 + |k_1|} \tag{2.52}$$

Thus a photonic gap opens up, and it can disappear only in the case of k_1=0.
The resulting band that represents the trend of the angular frequency ω as a function

of the wavevector k is depicted in Figure 2.15, where the dispersion relation for the 1D photonic crystal is compared with the dispersion relation obtained for a homogeneous material.

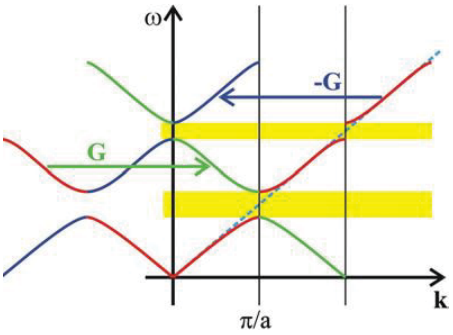

Figure 2.15: Dispersion relation for an homogeneous material (dashed straight line) and for a periodic material with lattice constant a. The yellow parts are the photonic band gaps whereas **G** are the reciprocal lattice vectors (41).

Due to the periodicity of the system, the two states with wavevectors k differing by 2π/a represent exactly the same state; the coupling of the modes with $k \approx \pi/a$ and $k \approx -\pi/a$ in the presence of the periodic modulation of the dielectric constant, causes a frequency splitting and the generation of the gap. For this wavevector there are two energy solutions $\omega_{\pm}$, one above and one below the gap (42).

In general, any material having periodic dielectric function falls in the category of photonic band gap structures. Periodicity can be made to occur in one, two or three directions, and the stop band width is mainly determined by the dielectric contrast: the greater the contrast the wider the gap.
As already mentioned, the length scale in which the variation take places (lattice parameter) determines the spectral range of use of the photonic crystal.
Thus, a photonic crystal working in the microwave range will present a dielectric function modulation in a period of the order of 1 cm, one working in the optical range of the electromagnetic spectrum will have a periodicity $\leq 1\mu m$, whereas the one used in the X-rays range is a solid-state crystals with a periodic modulation of some Ångstrom.

Bibliography

[1] M.Pope and C.E.Swenberg, *Electronic processes in Organic Crystals and Polymers*, Oxford University Press, New York (1999) ix, 8, 9, 11, 17, 20, 24

[2] R.S. Mulliken, *Ann.Rev.Phys.Chem*, **29** (1978) 9

[3] D.P. Craig and S H. Walmsley, *Excitons in molecular crystals: Theory and Applications*, W.A.Benjamin Inc., Amsterdam (1968) 12

[4] Thorsten U.Kampen, *Low Molecular Weight Organic Semiconductors*, WILEY-VCH, Weinheim (2010) 14

[5] J.Zamuseil and H.Sirringhaus, *Chem.Rev.*, **107**, 1296 (2007) 15

[6] N.W.Ashcroft and N.D.Mermin, *Solid State Physics*, Tomson Learning Inc., New Delhi (1976) 15

[7] H.Bässler and A.Köhler, *Charge transport in organic semiconductors*, Springer-Verlag Berlin Heidelberg (2011) 15, 16, 19

[8] W.W.Stehle et al., *Appl Phys A* **36**, 163 (1985) 16

[9] E.A.Silinsh and V.Cpek, *Organic molecular crystals: Interaction, localization and transport properties*, AIP press, New York (1994) 16

[10] H.Bässler, *Phys. Status Solidi B* **15**, 175 (1993) 16

[11] M.Vissenberg, M.Matters, *Phys. Rev. B* **57**, 12964 (1998) 17

[12] J.D.Wright, *Molecular crystals*; Cambridge University Press, Great Britain (1987) 17

[13] J.Yamashita and T.Kurosawa, *J.Phys.Chem.Solids* **5**, 34 (1958) 17

[14] P.G.Le Comber and E.Spear, *Phys.Rev.Lett.* **25**, 509 (1970)

BIBLIOGRAPHY

[15] J.C.Scott, *J.Vac.Sci.Technol.A* **21**, 521 (2003) ix, 18

[16] M.A.Abkowitz and R.A.Mizes, *Appl.Phys.Lett.* **66**, 1288 (1995) 19

[17] E.M.Conwell and M.W.Wu, *Appl.Phys.Lett.* **70**, 1867 (1997) 19

[18] J.R.Lackowitz, *Principles of fluorescence spectroscopy*, Springer science, New York (2006) ix, 24

[19] L.Moggi, A.Giuri and M.T.Gandolfi, *Manuale del fotochimico*, Bononia University Press, Bologna (2006) 25

[20] D.D.C.Bradley, *Molecular electronic materials and devices* (2004) x, 25

[21] R.Farchioni and G.Grosso, *Organic Electronic Materials* Springer science 22

[22] A.L.Schawlow and C.H.Townes, *Phys.Rev.*, **112**, 1940 (1958) 27

[23] T.H.Maimann, *Nature* , **187**, 494 (1960) 27

[24] T.S.Moss et al., *Semiconductor opto-electronics*, Butterworths e Co., London (1973) 27

[25] I.D.W.Samuel and G.A.Turnbull, *Chem.Rev.* **107**, 1272 (2007) x, 27, 32

[26] G.Kranzelbinder and G.Leising, *Rep.Prog.Phys.* **63**, 729 (1999) 27

[27] W.Demtröder, *Laser Spectroscopy 1*, Springer (2008) 27

[28] S.M.Sze and Kwok K.Ng, *Physics of semiconductor devices*, Wiley-Interscience, New Jersey (2007) 29

[29] O.Svelto, *Principles of lasers*, Springer (2010) 29

[30] A.E.Siegman, *Lasers*, University Science Books, Sausalito, CA (1986) 31

[31] P.W.Milonni and J.H.Eberly, *Lasers*, Wiley and sons (1988)

[32] R.Bonifacio and L.A.Lugiato, *Phys.Rev.A.* **11**, 1507 (1975) 32

[33] J.P.Dowling et al., *J.App.Phys.* **94**, 1896 (1994) 72

[34] M.Salerno et al., *App.Phys.Lett.* **90**, 111110 (2007)

[35] S.V.Frolov et al. *Phys.Rev.Lett***78**, 729 (1997) 33

[36] I.D.W.Samuel et al., *Nat.Phot* **3**, 547 (2009) x, 33

[37] P.Bassi, lectures notes for the course *Waveguide Engineering*, University of Bologna (2012) 34

[38] S.Meng and T.Kyu, Cap 26 of *Introduction to Organic Electronic and Optoelectronic Materials and Devices*, CRC Press (2008) 35

[39] J.D.Joannopoulos et al. *Photonic Crystals, molding the flow of light*, Princeton Univ.Press, New jersey (1995) 35

[40] K.Sakoda, *Optical Properties of Photonic Crystals*, Springer, Berlin (2001) 35

[41] C.Lopez, *Adv.Mat* **20** 1679 (2003) x, 36

[42] C.Lopez, *J.of Optics A* **8** R1 (2006) 36

3

Organic Field Effect Transistors and Organic Light Emitting Transistors

A transistor is a semiconductor device commonly used as an amplifier or as electrically controlled switch.
A *Field Effect Transistor* (FET) is a transistor where an electric field is used to control the flow of charge carriers in the semiconducting material; thus, the conductivity of the device and the amplification of the signal depends on the portion of the channel open to the current flow.
The first FET was invented in 1947 by John Bardeen, William Shockley and Walter Brattain (1).
Since their discovery, this kind of transistors have dominated the mainstream microelectronics industry becoming the fundamental building block of electronic circuits.
In 1986 the first transistor that uses an organic semiconductor as active material, called *Organic Field Effect Transistor* (OFET) was reported by A.Tsumara (2).
Nowadays, mobility in OFETs ranges between 0.01 and 10 cm^2/Vs, which is still lower than that found in inorganic FET (mobility is around 100 cm^2/Vs in crystalline silicon). For this reason, instead of competing with conventional transistors, OFETs may find nice applications in low performances radio frequency technologies (3), sensors (4) and light emitting devices that can be integrated in displays(5) (6).
Organic semiconductors for OFETs are technologically attractive because offer broad possibilities of rational structural tailoring, lightweight, low temperature and low cost deposition and good compatibility with various substrates, including flexible plastics

(7).

3.1 OFETs device structure

3.1.1 Configurations

The main constituting elements of an OFET are: three contacts (source, drain and gate) an active semiconducting material and a dielectric layer working as a capacitor, that allows current modulation by means of the gate voltage.
These key elements can be differently combined to obtain various device structures as it is shown in Figure 3.1.

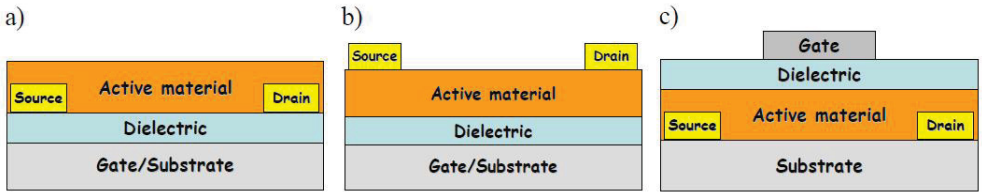

Figure 3.1: Typical OFET structures: a) bottom gate - bottom contact, drain and source are directly grown on the dielectric and the gate also functions as a substrate; b) bottom gate - top contact, drain and source are grown on the active material, and once again the gate works also as a substrate; c) top gate - bottom contact, the gate is on top of the structure and it is grown on the dielectric.

In the most common conguration, a thin film of organic semiconductor is deposited on top of a dielectric with an underlying gate electrode (*Bottom Gate* (BG)). Charge-injecting source-drain electrodes providing the contacts are deposited either on top of the organic film (*Top Contact* (TC) configuration) or on the surface of the dielectric (*Bottom Contact* (BC) configuration).
One of the major differences between these devices geometries arises from the fact that in the BG - BC configuration, charges are directly injected into the channel at the semiconductor/dielectric interface and do not have to travel several tenth of nanometer in the semiconductor active layer; moreover, this device configuration is easier to process, and the the active layer is not damaged by the growth of the electrodes (8).
On the other hand, the contact resistance is usually higher with respect to the BG - TC case, since source and drain are in contact with both the organic semiconductor and the dielectric layer, forming two interfaces where charges can be trapped; furthermore, in this configuration is more difficult to control the organic growth and to improve the OFET performances by treating the dielectric surface.

It is also possible to grown directly the semiconductor onto the substrate where the drain and the source contacts are already present, then the dielectric is deposited and the gate electrode is placed on top of it. This configuration is called BC - TG, it is used especially in the case of polymeric OFETs and has some interesting advantage compared to the BG configurations: *i)* the injecting contacts can be patterned by photolitography on the substrate and not on the active layer (that is not damaged) and *ii)* it is possible to use different polymeric dielectrics that can be solution coated on the semiconducting layer; this also offer protection and encapsulation to the semiconductor (9). Moreover, as in the BG - BC case, the charge are injected from all the electrodes surface and not only from the edge of them.

In Figure 3.2 it is shown the BG - TC configuration with indicated the channel length (L) and the channel width (W), that are fixed physical dimensions that can strongly influence the properties of the device.

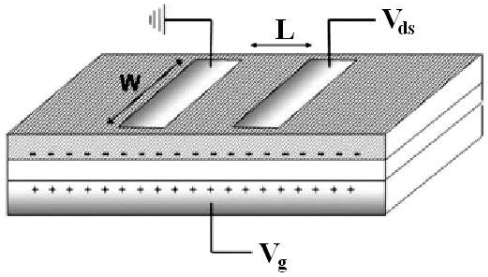

Figure 3.2: Classic BG-TC geometry with indicated the channel length (L) and the channel width (W).

3.1.2 Materials

3.1.2.1 Active layer

An OFET can be based on small molecules or polymer semiconductors.
In the first case, a plethora of organic compounds can be used: aromatic hydrocarbons as pentacene and perylene, organo-metallic complexes such as metalphtalocyanines and oxy-quinoline, fullerenes and dendrimers. However, the largest part of small molecules is represented by oligomers (formed by a finite number of monomer units) as for example oligo-phenylenes or oligo-thiopenes (see Figure 3.3) (10).
Generally, molecular materials are processed by vacuum sublimation. This technique allows to reach high chemical purity and high molecular order; the resulting films are

mainly poly-crystalline, and their growth (and consequently the morphology of the film) can be partially controlled acting on the vacuum sublimation parameters and selecting the nature of the dielectric.

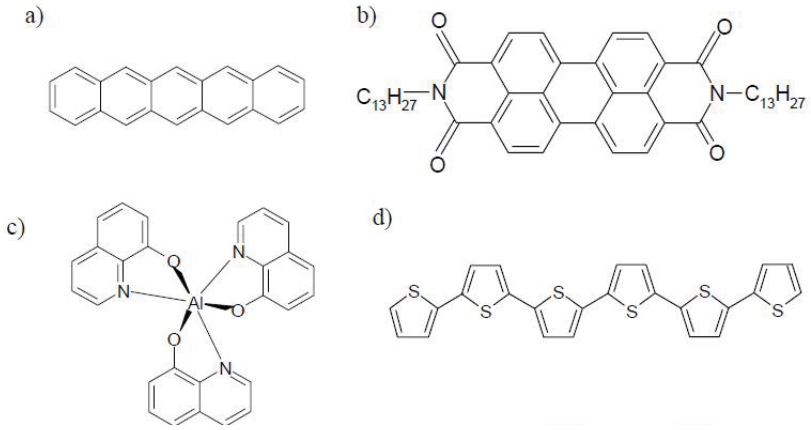

Figure 3.3: Chemical structure of some small molecules: a) pentacene, b) N,N - ditrydecylperylene - 3,4,9,10 - tetracarboxylic diimmide (PTCDI-$C_{13}H_{27}$); c) Allumin oxyquinolina (Alq_3); d) α-sexy-thiophene (T6).

Concerning the transport properties, the majority of organic semiconductor are *p-type* (e.g. α,ω-disubstituted quaterthiophenes with hexyl, named DH4T) (10), but in the last years several *n-type* materials have been produced, as for example perylene derivatives (11). Ambipolar small molecules able to transport both electrons and holes have also been synthesized, even though in a small number (12).

Polymers belong principally to three families: poly(phenylenevinylene) (e.g. MEH-PPV), poly-thiopene (e.g. P_3HT) and poly-fluorenes (e.g. F_8T_2) (see Figure 3.4).
Processability of polymers is usually restricted to wet techniques; this can be an advantage because of the inherently low cost and large area coverage of such techniques, but also a disadvantage as the structural and morphological control of amorphous thin films is limited. The consequence of the intrinsic morphological disorder is that charge mobility in polymeric thin films is typically lower with respect to that of small molecule films.
However, the electrical transport properties of polymers are not only related to their chemical structure; the processing conditions, the choice of electrodes and dielectric material have to be taken in account. Therefore, instead of *p-type* or *n-type* OFET, one should better refer to *p-channel* or *n-channel* transistors.

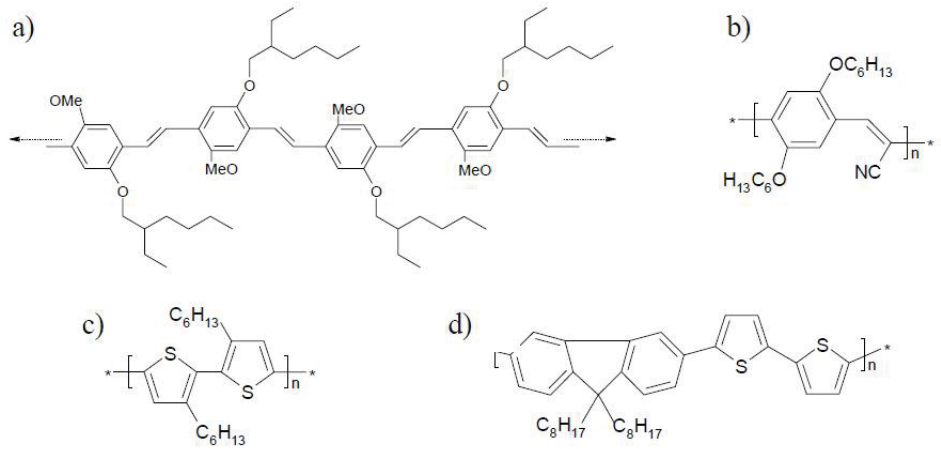

Figure 3.4: Chemical structure of some widely studied organic semiconductor polymers: a) Long chain of Poly[2- methoxy-5-(2-ethylhexyloxy)-1,4-phenylene-vinylene] (MEH-PPV); b) Poly[2,5,2,5-tetrahexyloxy-7,8- dicyano-di-p-phenylenevinylene] (CN-PPV); c) Poly[3-hexylthiophene] (P3HT); d) Poly[9,9-dioctyl-fluoreneco- bithiophene] (F_8T_2).

3.1.2.2 Electrodes

In order to allow the formation of a current flow within the transistor channel, charges have to be injected from the source electrode into the semiconductor: that means, for *n-channel* transistors, injection of electrons into the LUMO level and, for *p-channel* transistors, injection of holes into the HOMO level of the semiconductor.
The contacts, with few exceptions, are based on a direct metal-semiconductor junction without any doping, and it is necessary to align the HOMO or LUMO levels with the Fermi energy of the metal in order to reduce contact resistance, as it was mentioned in Chapter 2. For this reason, the injecting electrodes are usually high work function metals (e.g gold, platinum, etc) for *p-channel* OFETs and low work function metals (e.g. Calcium) for *n-channel* ones.
The gate contact has a different function and it is used to control the portion of the conduction channel open to the current. This electrode can be a metal, a conducting polymer or a layer of highly doped silicon.

3.1.2.3 Gate dielectric

The chemical nature of the dielectric/semiconductor interface is crucial to determine the transport properties of the transistor, since charges flow in the first nanometers of the semiconducting layer. Thus, reducing charge traps formation in this region is

mandatory (8).
The dielectric influences carrier transport since it can affect the morphology of the active layer and the orientation of the molecules, increasing the roughness and modulating the mobility of charge carriers.
In Figure 3.5 are reported the chemical structures of the most widely used dielectric polymers.

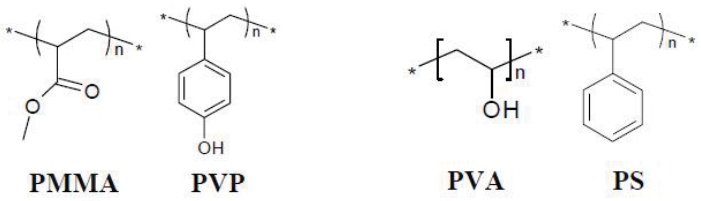

Figure 3.5: Chemical structure of the most widely used dielectric polymers in OFETs: PMMA (polymethylmethacrylate); PVP (polyvinylphenol); PVA (polyvinylalcohol) and PS (polystyrene).

Numerous studies have been done on the insertion of a *Self Assemble Monolayer* (SAM) on the surface of the dielectric. SAMs are highly ordered two-dimensional structures that form spontaneously on a variety of substrates, used as surface modification system that improve the semiconductor molecular alignment (13) (14).
Aside from the dielectric topography, a crucial role for the conduction is played by the value of the *relative permittivity* ε_r, that is proportional to the capacitance C_i according to the formula:

$$C_i = \varepsilon_0 \varepsilon_r \frac{A}{d} \tag{3.1}$$

where ε_0 is the vacuum permittivity (or electric constant), A is the cross-sectional area and d is the insulator thickness (15).
The relative permittivity of the implemented material strongly influences the *threshold voltage* V_{th} of the transistor, that determines the voltage at which the device starts to work.
An high ε_r can be obtained using inorganic dielectric species or hybrid organic-inorganic compounds (16); they allow to obtain high C_i values but the poor compatibility between inorganic and organic materials may introduce additionally trap sites at the interface.

3.2 OFETs working principles

As we have already seen, the dielectric layer is sandwiched between the gate and the semiconductor, and these two materials work as the plates of a plane capacitor. Thus, when a V_G is applied, charges of different sign are accumulated at gate/dielectric and dielectric/semiconductor interfaces.
The most part of charges in the active material are mobile and they move in response to the field applied in between the source and drain electrodes, referred as V_{DS}.
The origin of the gate-induced field effect is clarified in the energy level diagrams showed in Figure 3.6.

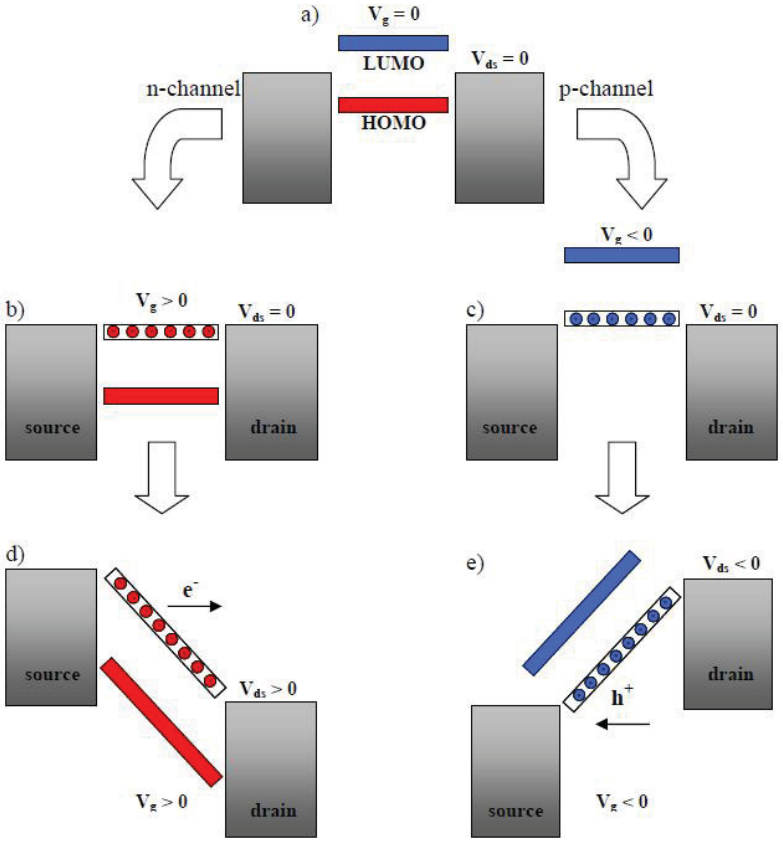

Figure 3.6: a) Schematic energy level diagram of an OFET at V_G=0 and V_{DS}=0; b) and c) electron or hole accumulation; d) and e) electron or hole transport (17).

The position of the HOMO and LUMO levels with respect to the Fermi levels of the contacts are sketched in the case of V_G=0; in this configuration, even if a bias is applied to V_{DS} there would be no conduction because there are no mobile charges in the semiconductor.

Application of a positive V_G leads to electron accumulation at the dielectric/ semiconductor interface and causes the LUMO level alignment with the Fermi levels of the contacts. If a negative bias is then applied between source and drain, an electrical current can flow through the LUMO level.
On the opposite case, when a negative bias is applied to V_G it causes the HOMO and LUMO levels to shift up, such that the HOMO becomes resonant with the Fermi level; electrons are spilled out of the semiconductor into the contacts, leaving holes, that can be treated as positively charged carriers free to move in response to an applied negative V_{DS}.
Usually, the voltage value at which mobile charge carriers are first introduced into the organic film does not correspond to V_G=0. The mismatch between the Fermi level of the metal and the HOMO/LUMO levels that has been mention in Section 2.2.2 may result in charge transfer between the metal and the semiconductor, causing band bending in the organic and the formation of a dipole; thus, the application of a nonzero V_G is necessary to achieve the flat-band condition (17).
Moreover, when starting to apply V_G bias, not all the induced charges are mobile and will contribute to the current, since deep traps have to be filled. A gate voltage higher than a threshold voltage V_{th} has to be applied in order to collect current in the device; the transistor is *on* only when the gate has a potential that overcome this threshold potential.
On the other hand, donor or acceptor states and interface dipoles can create an internal potential at the interface, causing accumulation of charges in the channel when V_G=0; for this reason, in some cases an opposite voltage has to be applied to turn the transistor *off*.

Usually, the biases are applied to the gate contact and to the drain contact, whereas source is grounded. Thus, source can be identified as the charge-injecting electrode, since it is always more negative than the gate electrode when a positive gate voltage is applied (electrons are injected) and more positive than the gate electrode when a negative gate voltage is applied (holes are injected).

3.2.1 Operating regimes

The basic operating regimes of an OFET (*linear*, *pinch-off* and *saturation*) are illustrated in Figure 3.7.
In the linear regime (see Figure 3.7 a), a small voltage superior to V_{th} is applied to V_{DS} that induces a linear gradient of charge density from the injecting electrode to the

drain; here, the current I_D is proportional to V_{DS}.

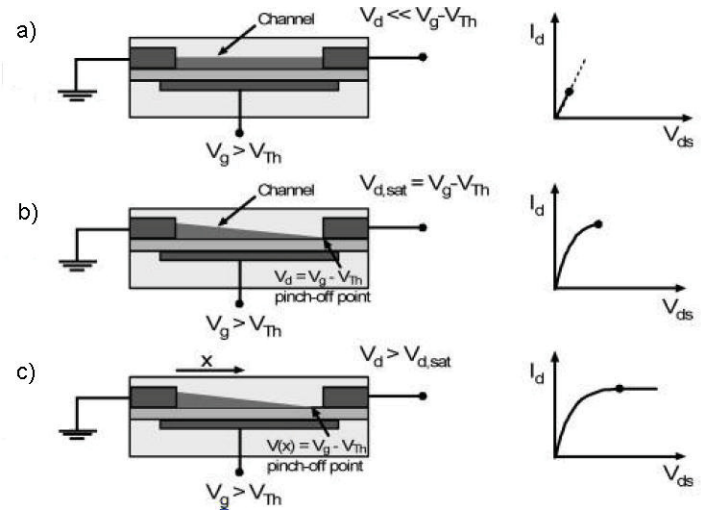

Figure 3.7: Illustration of the operating regimes of an OFET: a) linear regime; b) start of saturation regime at pinch-off; c) saturation regime and corresponding current-voltage characteristic (8).

When the applied bias reaches the value V_{DS}=V_G-V_{th} the channel is *pinched-off* and a depletion region is formed next to drain contact. In this point the difference between the local potential $V(x)$ and the gate voltage is below the threshold voltage and a *space-charge limited saturation current* flow between the contact through the narrow depletion zone.
Further increase in the voltage will not substantially increase the current as it is shown in the current characteristic of Figure 3.7 (c).

Current-voltage characteristics

The current-voltage characteristics can be described analytically in all the operating regimes just indicated, assuming the gradual channel approximation. This assumption is valid for long channel transistors, where the field generated by the gate voltage is much larger than the lateral electric field created by the drain voltage.
In this approximation, the density of the induced mobile charges per unit area Q_{mob} generated at the source contact, is related to V_G and to the position along the channel x as in the following equation (8):

$$Q_{mob} = C_i(V_G - V_{th} - V(x)) \tag{3.2}$$

The source-drain current I_D induced by carriers is:

$$I_D = W\mu Q_{mob} E_x \tag{3.3}$$

where W is the width of the channel, μ the field effect mobility of charges carriers and E_x the electric field at the x position.
By substituting Eq. 3.2 into Eq. 3.3, and integrating the current increment induced by the field E_x=dV/dt from x=0 to the end of the channel x=L (that is from V(x)=0 to V_{DS}) we obtain:

$$I_D = \frac{W}{L}\mu C_i[(V_G - V_{th})V_{DS} - \frac{1}{2}V_{DS}^2] \tag{3.4}$$

This equation is valid under the assumption that mobility is independent on the carrier density and hence on the gate voltage.
In the linear regime, Eq. 3.4 can be simplified to:

$$I_D = \frac{W}{L}\mu C_i(V_G - V_{th})V_{DS} \tag{3.5}$$

that states that the drain current is directly proportional to V_G. The field effect mobility can be written as:

$$\mu_{lin} = \frac{dI_D}{dV_G}\frac{L}{WC_iV_{DS}} \tag{3.6}$$

In the saturation regime, neglecting the channel shortening due to the depletion region, the current becomes:

$$I_{D,sat} = \frac{W}{2L}\mu_{sat} C_i(V_G - V_{th})^2 \tag{3.7}$$

where the square root of the saturation current is directly proportional to the gate voltage, and the mobility is assumed to be independent of V_G.
If this is not the case, a gate dependent mobility is reported:

$$\mu_{sat}(V_G) = \frac{dI_{D,sat}}{dV_G}\frac{L}{WC}\frac{1}{V_G - V_{th}} \tag{3.8}$$

The curves that are useful to describe a transistor behavior in these operating regimes are three: *locus curve*, *output characteristic* and *transfer characteristic*.
In the *locus curve characteristic*, the bias applied between source and drain is kept equal to the one applied between the source and the gate (V_{DS}=V_G). Therefore, the

transistor works in saturation conditions, and the field-effect transport is *n-type* if $V_G < 0$ and *p-type* if $V_G > 0$.
From this kind of characteristic, that is drawn for both the carriers type in Figure 3.8, it is possible to extract the saturation field effect mobility according to the formula 3.7.

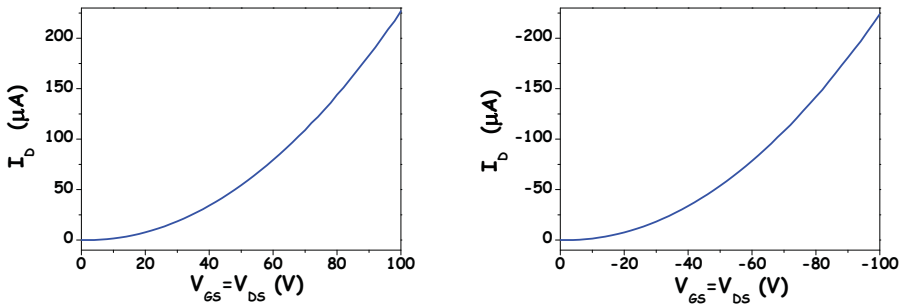

Figure 3.8: Locus curves for an *n-type* (left) or a *p-type* (right) transistor.

In the *output characteristic*, the drain current is displayed versus the applied source-drain voltage for different (but constant) gate voltages, as it is shown in Figure 3.9 (a). The linear regime, obtained for low V_{DS}, and the saturation regime are evident in the picture.

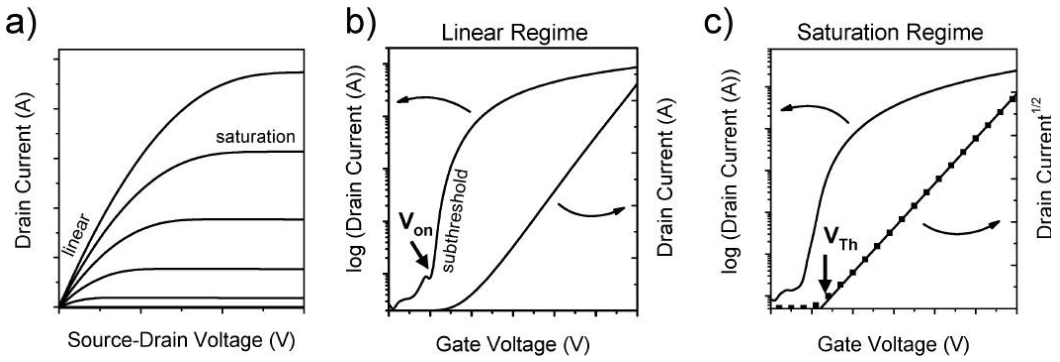

Figure 3.9: I-V characteristic for an *n-type* transistor: a) output characteristic b) transfer characteristic in the linear regime or c) in the saturation regime (8).

In the *transfer characteristic*, the drain current is collected versus the the applied gate voltage, at constant V_{DS}. From this curve in the linear regime (for $V_{DS} << V_G$) is possible to extract the linear mobility (according to the formula 3.6) and the onset voltage V_{on}, that is the voltage at which I_D abruptly increase.
From the transfer curve in the saturation regime it is possible to extract the voltage threshold (see Figure 3.9 c), the saturation mobility and the *on/off ratio*, which is the

ratio of the current while the device saturates for a given applied gate voltage to that of the value of the current when no gate voltage is applied (8).

3.2.2 The ambipolar field-effect transport

An OFET is defined *ambipolar* if it shows accumulation and conduction of both holes and electrons.
As already mentioned, the ambipolar behavior is not only due to the chemical structure of material composing the device active layer, but it is strongly influenced by processing conditions, device architecture and choice of electrodes.
From the scientific perspective, the ability to realize ambipolar OFETs opens new way to improve the understanding of the physical processes that governs these devices; in particular, a direct comparison of hole and electron transport can be done.
Moreover, ambipolar organic materials can be used to produce integrated devices such as inverters and multifunctional light emitting transistors.
For realizing OFETs having efficient ambipolar transport, different approaches can be pursued: *i)* the single-component approach, where a single organic material capable of transporting electrons as well as holes is employed (18), *ii)* a multilayer approach, where two unipolar transport materials are grown one on top of the other (19) or *iii)* a blend approach, where an *n-type* and a *p-type* material are blended together in the same layer (20), even though this approach is being abandoned.
The electrical behavior of ambipolar OFETs can be understood considering the voltage bias applied to all the three electrodes of the device.
Let us assume a transistor at a given positive drain voltage $V_{DS} > 0$, with the source electrode grounded. Let us start with a positive gate voltage $V_G = V_{DS}$; since the gate is more positive than the source electrode, electrons are injected from the source contact.
On the other hand, when $V_G < V_{DS}$, the gate potential is more negative than that of the drain electrode by V_G - V_{DS}; in this case, the drain electrode will inject holes into the channel, as it is sketched in Figure 3.10.

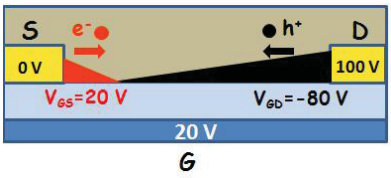

Figure 3.10: Schematic representation of both carriers injection in an ambipolar OFET.

Generally speaking, ambipolar transport occurs if the absolute value of the gate potential is lower than the absolute value of the source-drain potential, $|V_G| < |V_{DS}|$. In this condition, source and drain electrodes feel two local potentials of opposite signs and injection of both charge carriers can occur.
If an ambipolar transistor is realized with an electroluminescent material, electrons and holes that meet in the channel are expected to recombine leading to light emission from a well-defined channel zone. This is at the basis of the working principle of *Organic Light Emitting Transistors* (OLETs) that will be described in Section 3.3.

The I-V characteristics useful to describe ambipolar behavior are the transfer characteristic and the output characteristic.
The locus curves are used to describe the separate unipolar behavior of the two kinds of charge carriers. In the ambipolar case, the locus curves are identical to the one showed in Figure 3.8.
Transfer characteristics of ambipolar transistors, instead, exhibit the typical *V-shape* profile with one arm indicating the electron transport and the other indicating the hole transport regime, as it is shown in Figure 3.11.

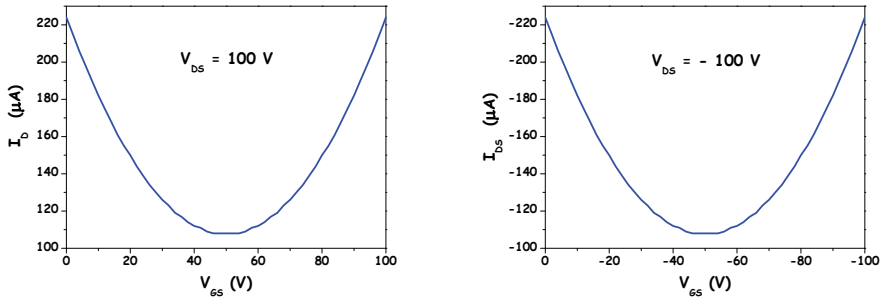

Figure 3.11: Transfer curves for an *n-type* (left) or a *p-type* (right) ambipolar transistor.

A transfer curve is symmetrical for the two polarizations, and the position of the minimum of the current is centered on $V_{GS} = V_{DS}/2$ if the transport properties are well balanced, while if one arm of the curve is less pronounced than the other it means that one of the two carrier presents lower mobility or higher threshold voltage.
The output curve of an ambipolar OFET, shows the contributions of both the unipolar regime (for $|V_G| \geq |V_{DS}|$) and the ambipolar regime (for $|V_G| < |V_{DS}|$).
The curve taken with V_G=0 is unipolar, since only one carrier can be injected from the contact. Increasing $|V_{GS}|$ the curves are composed by an unipolar part, identical to the unipolar output curve showed in Figure 3.9, and by an ambipolar part, where I_D

increases quadratically with respect to V_{DS}.
As in the previous case, the *n-type* and the *p-type* curves are identical if the transport properties of the two charge carriers are perfectly balanced, as it is shown in Figure 3.12.

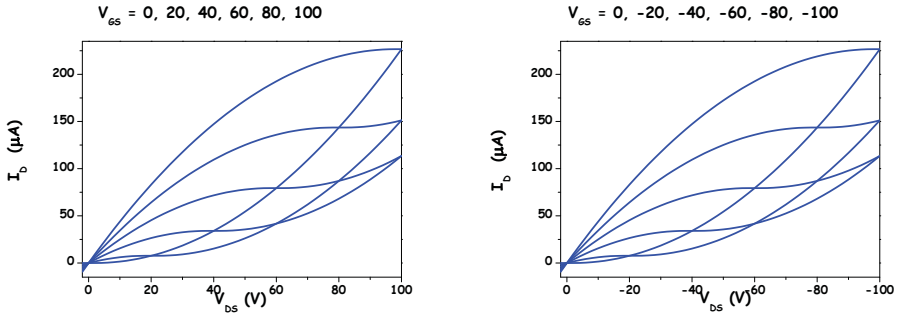

Figure 3.12: Output curves for an *n-type* (left) or a *p-type* (right) ambipolar transistor.

3.3 OLETs

Organic Light Emitting Transistors (OLETs) are multifunctional opto-electronic devices that combine the capability of light generation with the switching properties of OFETs.
They present some fascinating characteristics and unique features that allow the fabrication of novel integrated high-efficiency and high-brightness photonic devices.

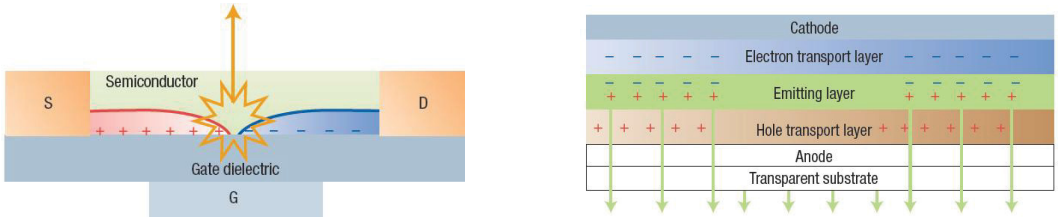

Figure 3.13: Schemes of an ambipolar OLET where is shown the charge transport that occurs parallel to the organic layers (left) compared to the vertical transport displayed in OLEDs (right); the arrows represent the emission of light. (21)

First of all, OLETs provide a unique planar architecture where the field effect transport of charges occurs horizontally with respect to the organic layers.
This is a clear advantage with respect to the vertical architecture displayed in *Organic Light Emitting Diodes* (OLEDs), where bulk transport of charges occurs perpendicularly to the organics, as it is sketched in Figure 3.13.

In this configuration, it is easier to improve the lifetime and efficiency of organic light emitting materials, to reduce the quenching processes and to optimize charge carriers balance (21). The planar architecture offers direct access for high-resolution imaging of the recombination zone, that is useful for probing fundamental optoelectronic properties of organic materials such as charge injection, exciton formation processes and recombination (22). Moreover, in this configuration the device has a superior integration potential and an intrinsically higher field effect mobility with respect to the bulk mobility displayed for OLEDs.

The quenching processes that can happen in a light emitting device can be divided in *static quenching*, that includes charge trapping at the semiconductor/dielectric interface and electrode-induced quenching, and *dynamic quenching*, that take into account exciton-exciton and exciton-charge quenching (23).
To measure if these quenching agents are affecting a light emitting device is used the *External Quantum Efficiency* (EQE), that is one of the most important figures of merit for light generation process, and gives a measure of the degree of conversion of current into light, according to the formula:

$$\eta_{ext} = \gamma \Phi_{QY} \chi \sigma_{out} \tag{3.9}$$

where γ is the ratio of injected electrons with respect to injected holes, Φ_{QY} is the photoluminescence quantum yield of the emitting material, χ is the fraction of excitons formed and σ_{out} is the light outcoupling efficiency.
Usually, the active organic material used for light emission is a singlet emitter, and thus the fraction of exciton formed χ is about 25% (24); the ratio γ is supposed to be equal to one and Φ_{QY} is a fixed value related to the photoluminescence emission efficiency of the light-emitting material.
Hence, a way to improve the EQE is to act on the light outcoupling efficiency σ_{out}, that is a measure of the photons produced inside the device that can be extracted out of it. This value can be increased working on the device configuration, as it will be explained in Chapter 4.

3.3.1 Architectures

The first demonstrated OLET was made by Hepp et al. in 2003, and the emission of light was achieved in an unipolar transistor made of tetracene (25). From that moment, various approaches were tried to obtain efficient light emission from these devices, acting

on the implemented architecture and on the selection of organic materials.

3.3.1.1 Unipolar OLETs

In unipolar transistors, despite the electrical transport is displayed only for one type of charge carrier, emission of light can occur since the local electric field in the proximity of the drain electrode is intense enough to induce the charge of the opposite sign to be injected in the organic layer (26).
Santato et al. assumed that in the case of the tetracene unipolar transistor made by Hepp, the voltage drop at drain electrode caused by a contact barrier, induced a distortion of the HOMO and LUMO levels of the material near the contact, thus determining the conditions for the tunnelling of electrons from the Fermi level of the metal contact to the LUMO of the organic (27).
In the unipolar case, EL takes place in proximity to the electrode, which is though intrinsically quenched by the interaction between excitons and metal. Moreover, the excitons formation and recombination occur in the same spatial region where charges flow, leading to a significant exciton-charge quenching (28); thus, this device architecture does not offer real improvements with respect to OLEDs, and the resulting EQE is very low (29).

3.3.1.2 Ambipolar OLETs

OLETs based on ambipolar single layer semiconductors can provide an effective *p*-*n* junction where charge carriers are accumulated by the gate voltage at the semiconductor/dielectric interface, then flow along the transistor channel under the applied bias and recombine emitting light, as it is shown in Figure 3.13.
The length of each channel and thus the position of the recombination zone depends on the applied gate and source-drain bias voltage and on the mobility ratio (8).
In general, carriers of both signs have to travel for micrometric distances in the channel, hence a stringent degree of molecular order, high ambipolar mobility values and high photoluminescence QY are required for the implemented organic material (23).
A good candidate can be poly(9,9-di-noctylfluorene-alt-benzothiadiazole) (F8BT), which was implemented by Zamuseil et al. for fabricating a device with an EQE of 0.8 % (30).
More recently, the same research group has produced an ambipolar device with EQE $\simeq$ 8% (24); this OLET is based on the same ambipolar active material, and a strong contribution to the enhance of the EQE is due to the utilize of a reflecting silver gate.
In ambipolar single-layer devices, the charge carrier accumulation and the exciton formation zone largely coincide, leading to no negligible exciton-charge quenching. More-

over, even if it is possible to use a low work function metal (e.g. Ca) for the *n-type* injecting electrode and a high work function metal (e.g. Au) for the *p-type* injecting electrode, it is difficult to build a structure where electron and hole transport are well balanced, and usually the recombination zone is located more in proximity to the electrode that injects the 'slowest' carriers.
To overcome these problems, a multi-component approach can be used, where two unipolar transport materials are employed, either blended in the same layer or grown one on top of the other. The latter configuration allows to obtain enhanced charge transport and mobility values, but it does not offer any control on the exciton quenching process due to charges, thus the resulting EQE is still quite low (33).

3.3.1.3 Trilayer approach in OLETs

A trilayer heterostructure approach in OLETs realization was developed in ISMN-CNR institute of Bologna (34).

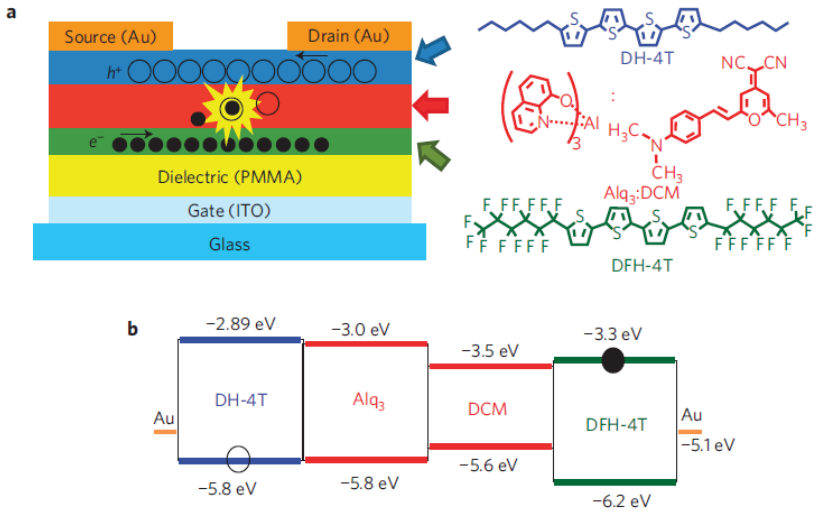

Figure 3.14: a) Schematic representation of the trilayer OLET device with the chemical structure of each material making up the device active region. The field-effect charge transport and the light-generation processes are also sketched; b) Energy-level diagram of the trilayer heterostructure. The energy values of the HOMO and LUMO levels of each molecular material are indicated together with the Fermi level of the gold contacts. (34)

In this configuration, the active layer consists of the superposition of three organic layers: an electron-transporting semiconductor, a light-emitting material and an hole-transporting semiconductor.
By means of this approach it is possible to achieve an EQE of about 5%, given that the

different quenching processes affecting the device efficiency, in particular the exciton-charge quenching, are under control.
In the proposed structure, the transport layers are made of perfluorohexyl (DFH-4T) for electron transport and α,ω-disubstituted-quaterthiophenes with hexyl (DH-4T) for hole transport, whereas the emitting layer is an host:guest matrix made of tris(8- hydroxyquinolinato)aluminium and 4-(dicyanomethylene)-2-methyl-6-(p-dimethylaminostyryl) -4H-pyran (Alq_3:DCM) (chemical structures in Figure 3.14 (a)). These materials were accurately chosen to obtain the best energetic compatibility between their energy levels, as it is shown in Figure 3.14 (b).

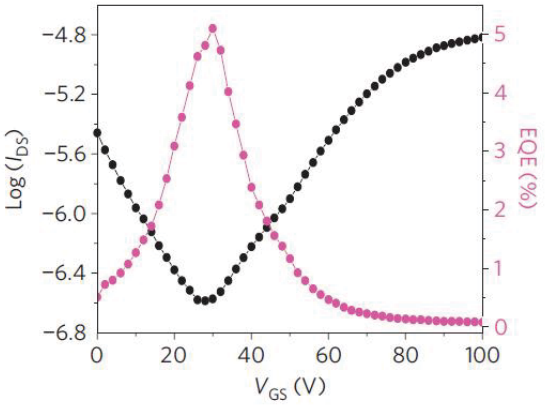

Figure 3.15: Transfer curve and EQE values obtained for the transistor configuration Glass/ITO/PMMA/DH-4T/Alq_3:DCM/DFH-4T (34).

The light-generation process is based on electrons and holes moving in the respective transport layers and percolating in the recombination layer where they form excitons due to mutual electrostatic attraction; then, excitons recombine radiatively.
The transverse electric field generated by electron and hole accumulation in the DFH-4T and DH-4T films, respectively, promotes charge percolation; thus, it is mandatory to avoid the formation of a potential barrier between these layers, and between the organic materials and the injecting contacts.
Furthermore, it is fundamental to control ad optimize the layers surface morphology in the device active stack, given that the field-effect transport is an interfacial process, as we have discussed at the beginning of this chapter.
From the opto-electronic characteristic shown in Figure 3.15 is evident that the device presents well-balance ambipolar transport with the maximum of the electroluminescence efficiency peaked at the minimum of the I_{DS} current (so that in ambipolar conditions).

Moreover, from the optical micrograph of the device channel showed in Figure 3.16, it is evident that the recombination zone (and hence the light emission zone) can be moved far away from the drain electrode by acting on source-gate voltage.

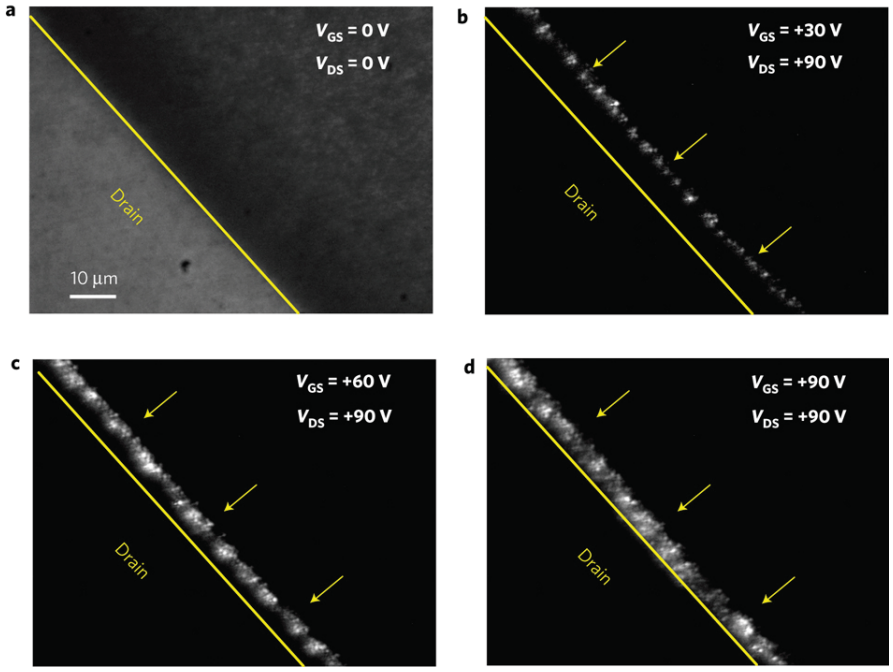

Figure 3.16: Images of the light-emitting area within the OLET device channel. a) optical micrograph of the device channel without bias to be use as reference; b-d) Optical micrographs of the emission zone within the device channel during a transfer scan at V_{DS}=90V and V_{GS} values of b) 30V; c) 60V and d) 90V (34).

In summary, it is possible to assert that the trilayer approach allow to obtain a simultaneous reduction of various exciton quenching processes, since in this configuration *i)* the recombination zone is located far away from the electrodes *ii)* the spatial density of exciton and charges in the recombination layer is reduced *iii)* there is no overlap of opposite charges accumulation layers and *iv)* excitons do not interact with trapped charges; hence, this device configuration allow to obtain an increased EQE. Indeed, it was demonstrated that the corresponding OLED with the same trilayer stack showed an EQE 100x less with respect to the trilayer OLET. This is an indirect demonstration of the reduction of exciton-charge annihilation and electrode photon losses in trilayer OLETs.

Bibliography

[1] J.Bardeen and W.H.Brattain, *Bell Telephone Laboratories*, Murray Hill, New Jersey (1948) 41

[2] A.Tsumara at al., *Appl.Phys.Lett.* **49**, 1210 (1986) 41

[3] V.Podzorov et al., *Phys.Rev.Lett.* **93** (2004) 41

[4] Z.T.Zhu et al., *Appl.Phys.Lett.* **81**, 4643 (2002) 41

[5] H.Sirringhaus et al., *Adv.Mater.* **17**, 2411 (2005) 41

[6] C.D.Sheraw et al., *Appl.Phys.Lett.* **80**, 1088 (2002) 41

[7] A.Facchetti, Cap 10 of *Introduction to Organic Electronic and Optoelectronic Materials and Devices*, Sam-S. Sun and L.R.Dalton Ed., New York (2008) 42

[8] J.Zamuseil and H.Sirringhaus, *Chem.Rev.* **107**, 1296 (2007) xi, 42, 46, 49, 51, 52, 56

[9] J.Zamuseil et al., *Adv.Mater* **18**, 2708 (2006) 43

[10] A.Facchetti, *Materials today* **10**, 28 (2007) 43, 44

[11] E.Di Donato et al., *J.Phys.Chem.B* **114**, 5327 (2010) 44

[12] M.Melucci et al., *Chemistry of materials* **25(5)**, 668 (2013) 44

[13] Y.D.Park et al., *Materials today* **10**, 46 (2007) 46

[14] D.H.Kim et al., *Adv.Funct.Mater* **15**, 77 (2005) 46

[15] J.Piprek, Cap 2 of *Introduction to Organic Electronic and Optoelectronic Materials and Devices*, Sam-S. Sun and L.R.Dalton Ed., New York (2008) 46

[16] Young-geun Ha et al., *J.American Chemical Society* **133**, 10239 (2011) 46

BIBLIOGRAPHY

[17] C.R.Newmann et al., *Chem.Mater.* **16**, 4436 (2004) xi, 47, 48

[18] M.C.Gwinner et al., *Chem.Mater* **21**, 4425 (2009) 52

[19] A.Dodabalapur et al., *Science* **269**, 1560 (1995) 52

[20] M.Loi et al., *Adv.Funct.Mater* **16**, 41 (2006) 52

[21] M.Muccini, *Nat.Mat.* **5**, 605 (2006) xi, 54, 55

[22] S.Zulkarnaen et al., *Adv.Funct.Mater* **19**, 1728 (2009) 55

[23] M.Muccini et al., *Laser Photonics Rev.* **6**, 258 (2012) 55, 56

[24] M.C.Gwinner et al., *Adv.Mat*, 10.1002/adma.201104602 (2012) 55, 56

[25] A.Hepp et al., *Phys.Rev.Lett.* **91**, 7406 (2003) 55

[26] K.Murata, *Appl. Phys. Lett.* **79**, 1193 (2001) 56

[27] C.Sanato et al., *Synth.Met.* **146**, 329 (2004) 56

[28] G.Generali et al., Cap5 of *Optoelectronic Devices and Properties*, Ed.O.Sergiyenko (2011) 56

[29] T.Oyamada et al., *J.Appl.Phys* **98**, 4506 (2005) 56

[30] J.Zamuseil et al., *J.App.Phys* **103**, 064517 (2008) 56

[31] E.B.Namdas et al., *App.Phys.Lett.* **92**, 3304 (2008) 57

[32] S. Zulkarnaen Bisri et al., *Adv.Funct.Mater* **23**, 2753 (2011)

[33] E.B.Namdas et al., *App.Phys.Lett.* **92**, 3304 (2008) 57

[34] R.Capelli et al., *Nat.Mat.* **9**, 496 (2010) xi, xii, 57, 58, 59

4

Light formation and outcoupling in trilayer OLETs

In this chapter I will show the specific optical features of light formation process within the trilayer OLET structure, together with innovative attempts in optimizing light extraction by introducing photonic structures in the active region of the device.

4.1 OLETs Recombination zone width

The majority of the reports that analyzed the *recombination zone width* (W_{RZ}) of OLETs argued that it can be studied on the base of a *p-n junction* model (1).
These studies suggest that W_{RZ} depends on both the structural properties of the active layer and on the overall optoelectronic devices characteristics (2); in particular, this parameter should depend on the accumulation-layer thickness, insulator thickness and on the bimolecular recombination strength, that is proportional to the carriers mobilities according to the Langevin recombination model (3).
Modeling approaches regarding single layers OLETs predict that the maximum extension of the recombination zone is around 500 nm (5). However, the observation of single-layer ambipolar thin film transistors, either by scanning Kelvin probe microscopy or by optical microscopy, showed that the W_{RZ} is 1-2 orders of magnitude larger than the theoretical prediction (6).
This discrepancy is attributed to the failure of the *p-n junction* model (1) and on the deviation from the bimolecular recombination parameter, which is intrinsically correlated to the width of the in-plane interpenetration of the hole and electron concentration profiles (8).

To improve OLETs light emission properties it is necessary to increase the device emission area with respect to the 8-10 μm-width displayed in Figure 3.16.
Indeed, a narrow illumination area is a severe technological drawback for the use of OLET devices in lighting applications, for example in flat panel displays.
Differently from single-layer devices, in trilayer OLETs the emission area is related to the vertical electrostatic interaction between hole and electron flowing in the respective transport layers; thus, in principle it is possible to promote the lateral distribution of the carriers and to improve the balance of hole and electron currents to obtain a wider W_{RZ}.

4.1.1 OLETs with full channel illumination

At ISMN-CNR we have recently shown that the trilayer approach is intrinsically suitable for displaying unconventional broadening of the emission area (8).
The device architecture that allows to obtain a wider W_{RZ} is similar to the one described in Section 3.3.1.3 but with a different light-emitting layer, that in this case is an host:guest system made by tris(8-hydroxyquinolinate) aluminum (Alq_3) and platinum-octaethyl-porphyrin (PtOEP) (see Figure 4.1).

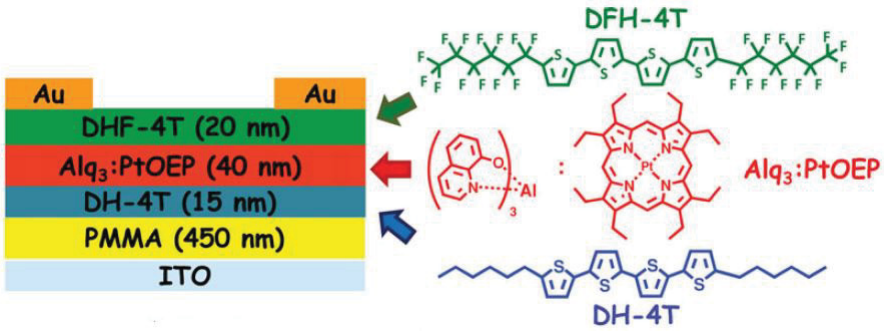

Figure 4.1: Schematic configuration of a three layers OLET configuration that display full channel illumination (8).

The *p-type* transfer curve with the corresponding EQE of the full-channel illuminated OLET is reported in Figure 4.2.
It is clear that the device shows a good ambipolar behavior and a more balanced electron and hole transport with respect to the one showed in Figure 3.15.
Indeed, the *n-type* and *p-type* mobility values calculated in unipolar bias conditions are $\mu_n = 0.20\ cm^2/\text{Vs}$ and $\mu_p = 0.28\ cm^2/\text{Vs}$, with corresponding gate threshold values of

V_{th-n} = 50 V and V_{th-p} = -60 V.

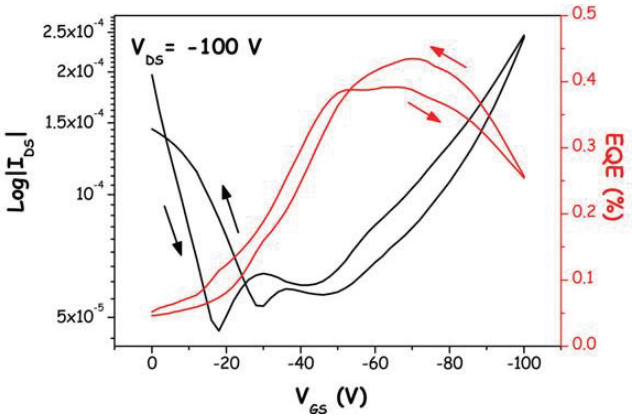

Figure 4.2: Transfer curve and EQE values obtained for the Glass/ITO/PMMA/DH-4T/Alq_3:PtOEP/DFH-4T transistor configuration (8).

The trilayer architecture is the only one that allows to optimize the field-effect charge transport properties of the conducting layers and to avoid the in-plane inter-penetration of the accumulated-charge profiles, and the advancements obtained in the device transport properties are due to an extensive and systematic effort in controlling the layers interface morphologies by acting on the growth parameters.

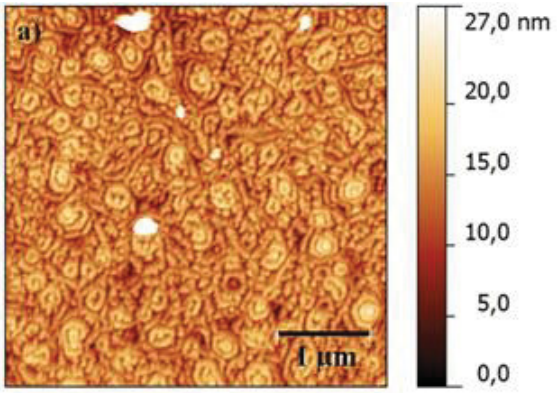

Figure 4.3: AFM topography of 40 nm thick Alq_3 recombination layer grown on top of 15 nm thick DH4T layer, which was deposited onto PMMA/ITO/Glass substrate; the root-mean-square roughness is 3.15 nm.

From picture 4.3 it is evident that the surface morphology of the Alq_3 recombination layer is very regular; in fact the resulted root mean square rougness is 3.15 nm. This value is lower with respect to the one obtained for the Alq_3 layer that has been

implemented in the trilayer structure described in Section 3.3.1.3. In that case, the topography of the material revealed three-dimensional globular aggregates with diameters ranging from 100 nm to 300 nm; for this reason, that structure showed a less developed ambipolar transport (9).

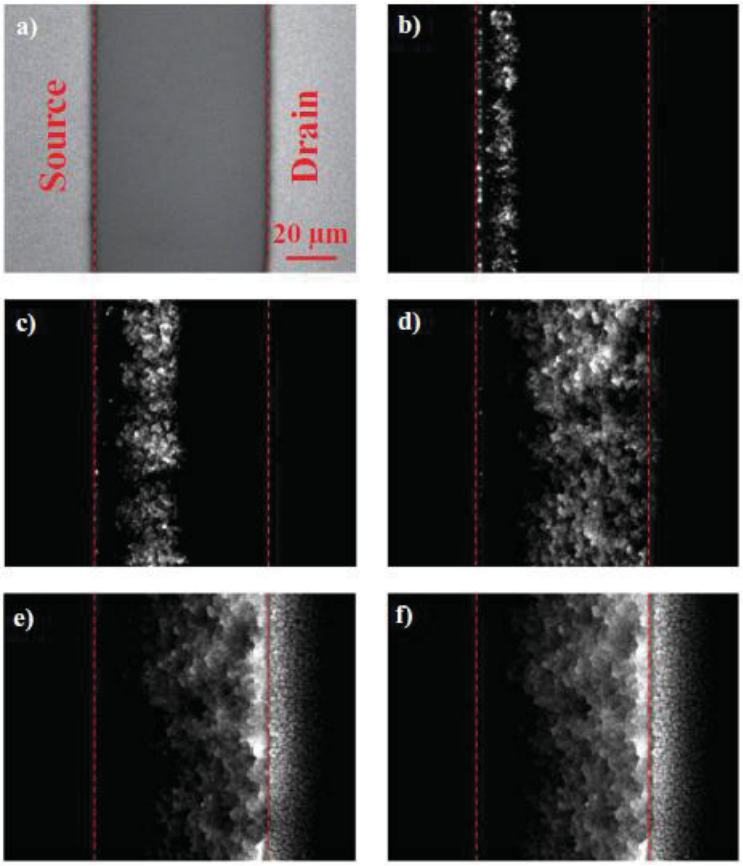

Figure 4.4: Transmission optical microphotograph of the light-emitting area in OLET channel. a) reference b) V_{GS}=-20V; c) V_{GS}=-40V; d) V_{GS}=-60V; e) V_{GS}=-80V and f) V_{GS}=-100V. V_{DS} was kept constant at -100V (8).

In Figure 4.4 are reported the optical microphotographs that highlight the broadening of the emission area in the OLET configuration that displayed the full-channel illumination.
In specific, in Figure 4.4 b) it is shown that applying V_{GS}= -20 V and V_{DS}= -100 V, and therefore working in the electron-injection regime, a 10 μm wide light-emitting region is formed starting from the edge of the source electrode. With increasing $|V_{GS}|$, the emission stripe shifts towards the drain electrode becoming broader and brighter. In ambipolar regime, the emission area covers almost completely the 70 μm channel,

reaching the drain electrode and extending for few microns underneath, as it is shown in Figure 4.4 d).
The emission in the center of the channel is progressively reduced as V_{GS} increases above 60 V. However, the emission zone exceeds 40 μm also in the purely unipolar *p-transport* condition, as it is clear from Figure 4.4 f).
This demonstrates that the electrostatic interaction among accumulated-charge distributions of opposite signs, that is at the basis of the exciton formation process, is enhanced by the balanced electron and hole current densities. Hence, it is possible to obtain an homogeneously distributed light emission area within the channel.

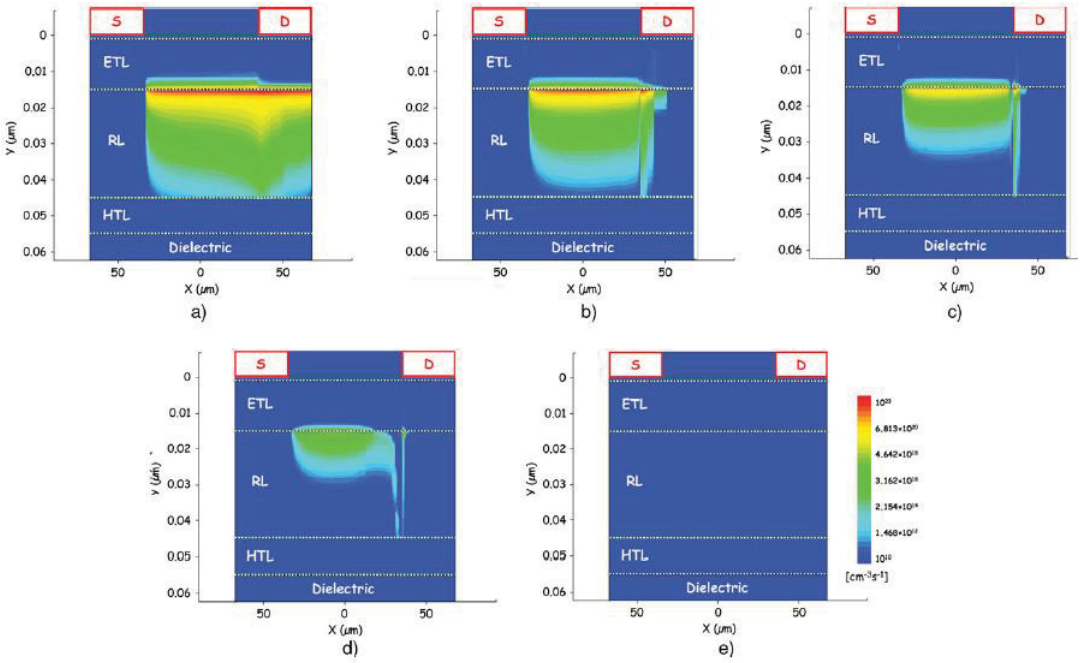

Figure 4.5: Distribution of the exciton radiative annihilation rate per volume unity within a transversal section along the channel length of a trilayer OLET, when the device is biased at: a) V_{GS}= -100V, b) V_{GS}= -80V, c) V_{GS}= -60V, d) V_{GS}= -40V and e) V_{GS}= -20V, while keeping V_{DS}= -100V (8).

In order to gain a deeper insight in the the optoelectronic performances of the OLET trilayer, we have implemented a two-dimensional numerical simulation for investigating the exciton distribution within the device channel at different bias working condition. In particular, the singlet exciton equation related to Frenkel excitons was introduced to account for the device optical properties, besides the simulation of the electrical part consiststed of solving the Poisson and continuity equations (10); the radiative decay of

excitons was set to be governed by a lifetime model.
The following model parameters were used: exciton radiative recombination lifetime $\tau_{rad} = 10^{-8}$ s, exciton carrier capture section $\sigma = 10^{-14}\ cm^2$, horizontal carrier mobility $\mu_o = 10^{-7}\ cm^2$/Vs and vertical mobility $\mu_v = 10^{-5}\ cm^2$/Vs.
The simulation showed that the exciton distribution (and therefore the emitted optical intensity) was almost homogeneously spread along the channel length direction, and localized within the recombination layer (see Figure 4.5). Moreover, we observed that in *p*-unipolar bias condition, the exciton distribution was extending underneath the drain electrode for microns.
The result is in accordance with experimental evidences, as it is clear from the already described optical microphotographs of the trilayer OLET (see Figure 4.4).

4.2 Electroluminescence angular emission profile

In order to experimentally investigate the vertical bulk exciton distribution in the multilayer stack, we performed a comprehensive characterization of the electroluminescence angular emission profiles of the trilayer OLETs.
These measurements were also useful to verify if the broadening of the emission zone obtained experimentally was due to waveguide effects, and to check whether the refractive index mismatch in the multilayer stack can cause *Total Internal Reflection* (TIR) phenomenon, inducing an angular emission profile different with respect to the typical Lambertian profile reported for OLEDs (11).
The home-made setup we have implemented for the collection of the trilayer OLET angular emission profile is described in Section 6.2.2. The setup was used to test different device configurations, and in every case, the sample-detector distance was set to guarantee a 5^o angular resolution and no instrumental modulation of the profile.

4.2.1 Experimental results

In the case of OLET with 70 μm channel length and 15 mm channel width, the device was positioned with the channel length direction either orthogonal or parallel to the rotation axis, in order to investigate whether the anisotropy in the channel dimensions could affected the shape of the angular profile. Moreover, OLEDs based on the same emitting layer were fabricated, to compare also experimentally the OLETs angular emission profiles with respect to the standard ones reported for OLEDs (12).
The angular EL emission profiles collected from the OLET in different rotation positions and from standard OLED are showed in Figure 4.6.

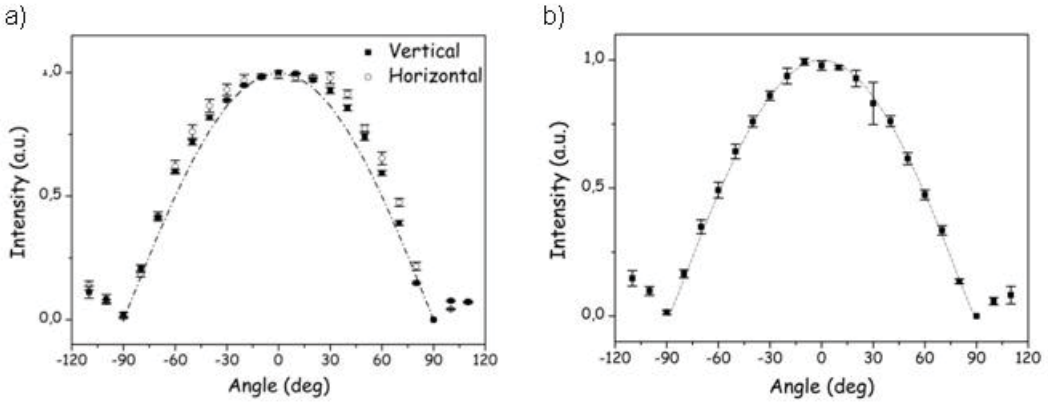

Figure 4.6: EL angular emission profile collected from a) a trilayer OLET with 70 μm x 15 mm channel dimensions, obtained in different rotation positions; b) 1 mm^2-wide OLED composed by glass/ ITO/Alq3-PtOEP/ α-NPB/ Al/ LiF.

From the reported graphs it is evident that the OLET device geometry influences the profile shape, that results slightly modified according to the fact that the device rotates either around (vertical configuration) or orthogonally (horizontal configuration) to the channel length direction.

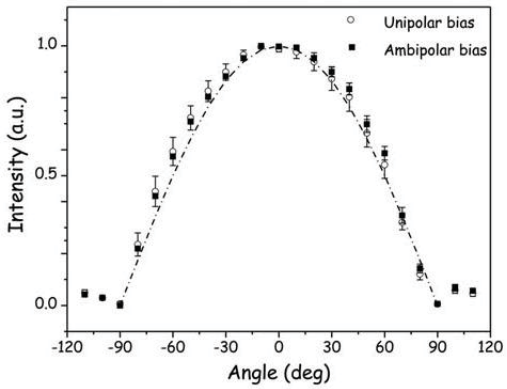

Figure 4.7: EL angular emission profiles for a three layer OLET, biased at V_{DS} =V_{GS} =100 V (unipolar condition) and at V_{DS}= 100 V and V_{GS}= 60 V (ambipolar condition), compared to a lambertian distribution (dashed line) (8).

Thus, OLETs with 70 μm x 1 mm channel dimensions where fabricated, in order to mimic a point-like light-emission source as required in brightness measurements of opto-electronic devices.
In this way it was possible to discriminate whether the broadening in the angular

emission profile obtained in Figure 4.6 a) was only due to the intrinsic anisotropic emission area of OLETs. Indeed, we have verified that the emission profiles of reduced channel-width devices were invariant with respect to the rotation configuration.
The EL angular distribution profiles of one of these 70 μm x 1 mm channel device, biased in unipolar and ambipolar conditions, are showed in Figure 4.7. The profiles are both slightly broader in the 30^o-70^o angular range than the lambertian -cosine curve. Surprisingly, the EL profiles obtained in the different bias regimes almost coincide, despite the fact that in unipolar conditions a portion of EL is clearly emitted underneath the electrode, as it was clarified in the previous section. Hence, we can suppose that the presence of the electrodes does not influence the EL angular profile, and that the slightly broader shape of the spectra are not due to scattering of light at the gold contacts.

4.2.1.1 Optical simulations

To confirm the hypothesis, we performed simulation of the emission profiles by means of a commercial software (SETFOS, *FLUXiM*) typically implemented to simulate light extraction from multilayer opto-electronic devices (13) (14).

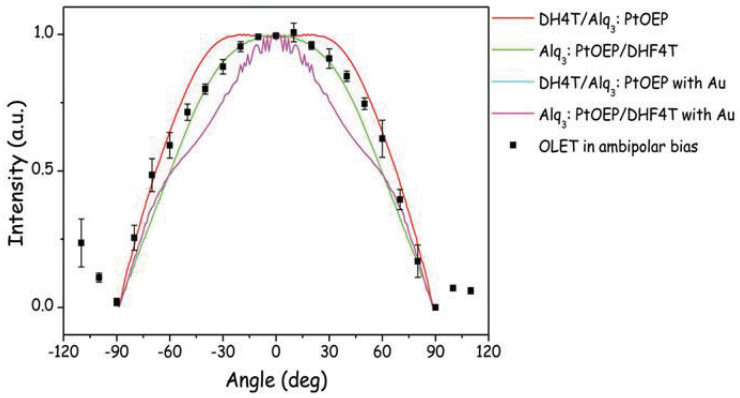

Figure 4.8: EL angular emission profile collected from the OLET in ambipolar condition (square symbols) compared to SETFOS-simulated profiles (solid lines) for a glass/ITO/PMMA/organic multilayer stack. The oscillating dipoles are located at the interface between the recombination and electron-transport layers, with or without the introduction of a top gold electrode (green and magenta lines) or between the hole-transport and the recombination layers (red and cyano lines) (8).

To assess whether the lateral and vertical localization of the recombination zone is expected to modify the angular light distribution, we compared the measured OLET

emission angular profiles in ambipolar bias condition, with the ones obtained by simulating a cathodeless structure formed by a glass/ITO/PMMA substrate and a DH4T /Alq_3:PtEOP/DFH4T organic stack. The top gold electrode was inserted in the simulated multistack for miming the OLET emission profile in unipolar bias conditions.
The position of the radiative recombination of excitons on PtOEP molecular sites in the emission layer was modeled by distributing isotropically oscillating dipoles at the interfaces between the recombination layer and the n-transport layer (Alq_3: PtOEP/ DFH4T interface) or between the recombination layer and the p-transport layer (DH4T/ Alq_3:PtOEP interface).
As it can be observed in Figure 4.8, the simulation of the vertical multilayer stack with the top gold electrode does not fit the experimental data for almost the entire angular range.
On the other hand, if we consider the simulation of the structure without the electrode, the experimental angular emission profile is well-fitted for angles up to 40^o by the simulation having the oscillating dipoles located at the Alq3:PtOEP/ DFH4T interface. For wider angles, the measured data are better described when the emitting dipoles are located at the DH4T/ Alq3:PtOEP interface.
These results suggest that light outcoupling in OLET devices (working in both bias conditions) is almost insensitive to the presence of the gold drain and source electrodes, as it was hypothesized previously.
Moreover, the fact that the experimental angular emission profiles lie in-between the simulated ones calculated imposing exciton recombination at either the DH4T/ Alq3: PtOEP or the Alq3:PtOEP/ DFH4T interface, may suggest that OLET emission zone extends in the bulk of the recombination layer. This hypothesis is also corroborated by the simulation of the distribution of the exciton radiative annihilation rate that has been shown in Figure 4.5.

The EL spectra at different collecting angles were measured in order to check whether wavelength-dependent microcavity effects were present. From the measurements, reported in Figure 4.9, it is clear that the spectrum profile and peak wavelength of the emission do not notably vary with the collecting angles, except for a slight reduction of the FWHM value obtained for the spectrum collected putting the detector almost parallel to the device substrate. This evidence points out that in trilayer OLETs are not present optical microcavity perturbations.
Microcavity effects are often present in light emitting devices (16); even if this is not the case, other effects such as waveguide and TIR process can strongly affect the light

extraction of OLETs, causing photon losses, and preventing the majority of photons that are generated inside the devices to be usable outside (17).
As results, the device external quantum efficiency, and in particular the light outcoupling efficiency σ_{out} (see Formula 3.9), remains low.

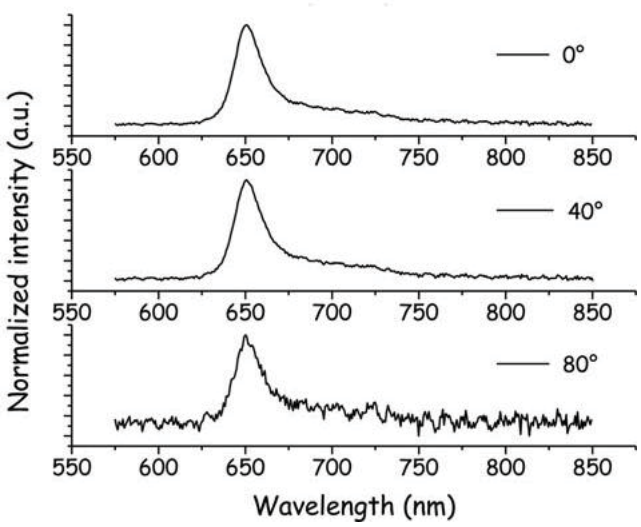

Figure 4.9: OLET EL spectra as a function of the emission wavelength measured at different collecting angles (8).

According to Snell's law, total internal reflection can happen when light, traveling from a medium with a higher refractive index n_1 to one with a lower refractive index n_2, has an incident angle θ_1 bigger than a critical angle θ_c defined as:

$$\theta_c = arcsin\frac{n_2}{n_1} \tag{4.1}$$

Thus, in a multilayer structure, the refractive index mismatch between the layers can induce TIR processes, as it is sketched in Figure 4.10.
If we consider a trilayer OLET as the one already described, we can suppose that the refractive index mismatch between the three organic layers is small, and thus we do not expect strong modification of the light path within this part of the device.
On the other hand, light that has to travel from the organic layers to the PMMA dielectric layer, and from the ITO layer to the substrate, can be total reflected according to Eq. 4.1, as it is drawn in Figure 4.11.
The EL angular light emission profile measurements described in this section were also useful to quantify these effects, and to verify whether they where strongly affect the light outcoupling efficiency of the device.

To conclude this investigation, given that we have demonstrated with optical simulations that the broadening of the spectra are not due to electrode-induced microcavity effects, we can state that the shape of the angular emission profile obtained experimentally for trilayer OLETs are actually due to TIR phenomena, that prevent some light to be extracted from the top part of the device.

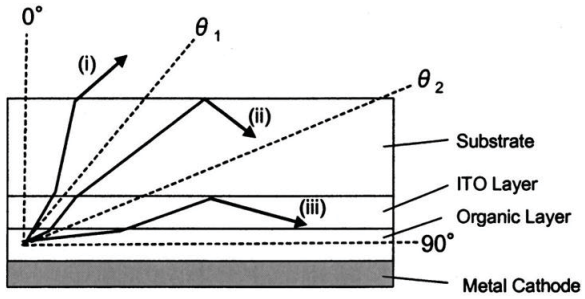

Figure 4.10: Light ray diagram for an OLED where are indicated the critical angles θ_1 and θ_2 and i) the external mode (representing rays that can exit from the device since $0^o \leq \theta < \theta_1$); ii) the substrate mode (representing light trapped by TIR at the glass/air interface that usually propagates to the edge of the glass for $\theta_1 \leq \theta < \theta_2$) and iii) the ITO/organic mode (light trapped at the ITO/substrate interface for $\theta_1 \leq \theta < 90^o$) (18).

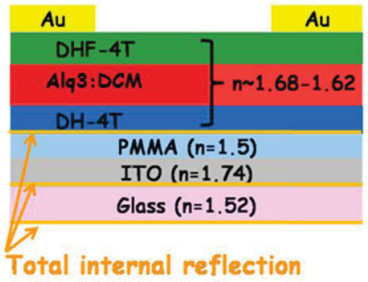

Figure 4.11: Trilayer OLET structure with indicated the refractive index of the materials and the TIR interfaces.

4.3 Photonic structures

Reduction of TIR and thus enhancement of the brightness of light emitting devices can be achieved by introducing microstructures (20), refractive index control (22) or photonic crystal structures, so that the light is manipulated in emission profile and wavelength (23).

Among these structures, *Distributed Bragg Reflectors* (DBR) are 1-D photonic crystals

composed of a regular stack of layers of two dielectric materials having strongly different refractive indexes (see Figure 4.12); each layer boundary causes a partial reflection of light passing the structure, and for the waves whose wavelength is close to four times the *optical thickness* $n_i d_i$ of the layers, the many reflections combine in constructive interference and the structure act as an high-quality reflector, according to the formula (24):

$$\lambda = 2(n_1 d_1 + n_2 d_2) \tag{4.2}$$

where λ is the wavelength of the reflected light, n_i are the refractive indexes and d_i are the thicknesses of the layers.

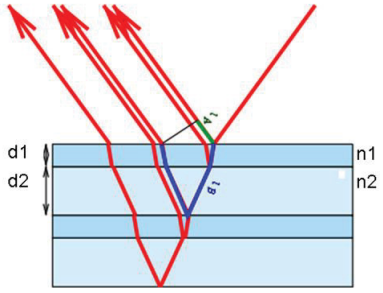

Figure 4.12: Reflection and constructive interference of light in a DBR structure.

4.3.1 Opto-electronic gate dielectric

Thanks to its planarity, a DBR structure can be implemented in a transistor in substitution of the standard gate dielectric layer, if the composing materials present proper dielectric properties. The resulting *Opto-Electronic Gate dielectric* (OEG) can be useful to increase the light outcoupling of the device by reflecting light that would normally be lost, and offers a way to transform the gate dielectric in an optically active component. An interesting example is given by the work of Namdas et al., that developed a DBR composed of three pairs of alternating high and low refractive index materials of quarter wave thickness (SiN_x/SiO_2, $n_{SiNx} = 2.03$ and $n_{SiO2} = 1.48$) to be used as dielectric in organic light emitting transistors.
This structure showed a 90% reflectivity peaked at a wavelength of the OLET electroluminescence spectrum. In this way, it was possible to increment the overall brightness of the device, as it is shown in Figure 4.13 (25).
To implement an OEG as a gate dielectric, the structure has to maintain stringent electrical requirements such as *i)* low gate leakage current, *ii)* ability to sustain high

voltages, *iii)* low trap density, *iv)* high capacitance and *v)* low surface roughness. Moreover, the photonic effect induced by the OEG has to be strong enough and located in a specific spectral range.

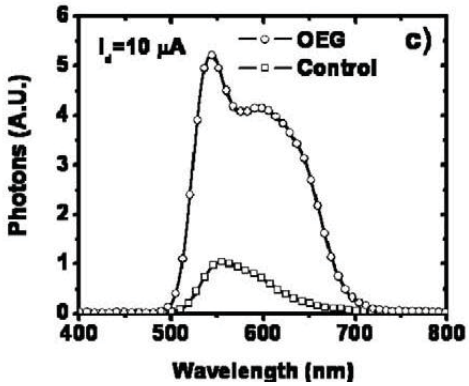

Figure 4.13: EL spectra measured for the *OptoElectronic Gate dielectric* (OEG) and control light emitting transistors for the device reported in Ref. (25).

To obtain a photonic effect implementing organic materials is more difficult, since they usually have a quite low mutual refractive index contrast; though, the realization of a fully organic optically-active OLET can guarantee low cost and easy fabrication techniques, together with the implementation of flexible substrate ad the improvement of photonic integration capability.

4.3.1.1 Organic opto-electronic gate dielectric

In collaboration with Politecnico of Milano, we have built an OLET with an opto-electronic gate dielectric made with cellulose acetate (CA, *Acros Organics*) and polyvinylcarbazole (PVK, *Acros Organics*) (molecular structures in Figure 4.14), two promising organic dielectric materials that exhibit a relatively high Δn between each other (n_{CA}=1.475, n_{PVK}=1.683 $\rightarrow$ Δn=0.208). Indeed, these materials are used for the fabrication of novel laser cavities (26).
Cellulose acetate and PVK are suitable materials to be used in a multilayer (ML) structure, since they are soluble in two orthogonal solvents (diacetone alcohol and chlorobenzene, respectively) and they can be deposited by spin-coating one on top of the other without dissolving.
We have selected a concentration of 53.5 g/L and 24.4 g/L, and the spin-coating parameters were 4000 rpm, 4000 rpm/s x 60 s and 3600 rpm, 3600 rpm/s x 60 s for CA and PVK, respectively. These deposition conditions allowed to obtain layers of 100 nm for

CA, and of 80 nm for PVK; these thicknesses are optimized for achieving constructive interference in the spectral range of the emitting material (e.g. Alq_3).

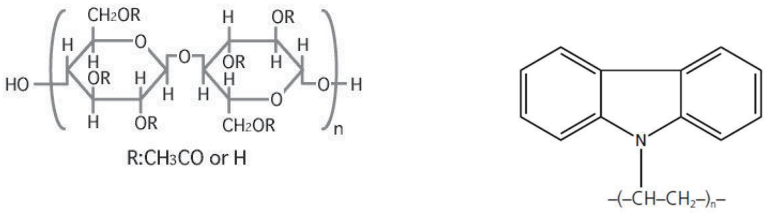

Figure 4.14: Molecular structures of CA and PVK.

We have deposited 5 alternating layers of CA/PVK on top of the standard glass/ITO substrate used to produce a BG - TC device; then the deposition of the hole and electron transport layers (DH-4T and DFH-4T) separated by the recombination layer (Alq_3:DCM_2) has been followed, and the resulting device had the structure showed in Figure 4.15.

Figure 4.15: Structure of an OLET device with the gate dielectric composed of 5 layers of CA and PVK.

The dielectric capacitance of the structure resulted 750 pF; this value allowed field effect transport, and thus the device was working as a normal OLET as it is clear from the locus characteristic and EL emission reported in Figure 4.16.
As expected, the transmittance spectra of the dielectric structure showed a spectral modulation induced by the periodic variation of the refractive indexes (see Figure 4.17), but the photonic effect induced by the organic opto-electronic gate dielectric was not intense enough to modify the EL emission of the device.
Since the the photonic band gap efficiency is proportional to $\Delta n{\cdot}d$ (27), to optimize the structure was necessary to increment the number of dielectric layers, with the consequent drawback of reducing the capacitance C_i of the dielectric, according to the

formula 3.1.

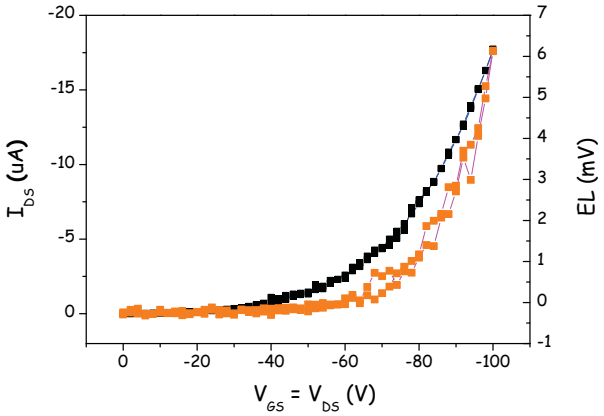

Figure 4.16: Locus curve characteristic of an OLET having the structure sketched in 4.15.

Otherwise, another possible solution for improving the photonic properties of the OEG dielectric was to use a high refractive-index material, while maintaining small the number of the composing layers.

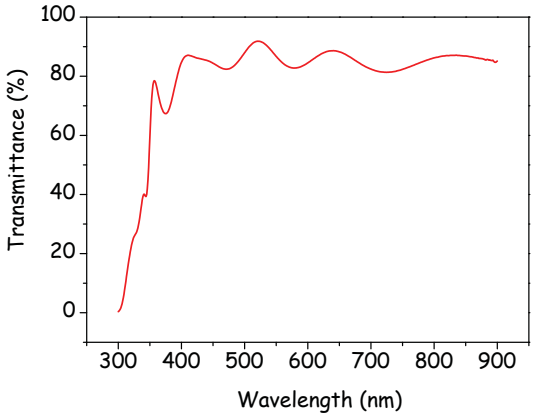

Figure 4.17: Transmittance spectrum of a multilayer composed of 5 layers of CA and PVK.

The first option resulted not feasible because the minimum number of CA/PVK layers necessary to obtain an evident photonic effect was too high to use the structure as a dielectric in a transistor.
An example of the spectral modulation that can be obtained with a ML structure it is

shown in Figure 4.18, where the modification of the PL emission of Alq_3 when deposited on top of CA/PVK stack composed by 27 layers is reported.
This structure is too thick to be inserted in substitution of the gate dielectric, but it has been deposited on the glass substrate of an OLET, to be used as passive optical component for enhancing and vertically guiding light outcoupling.

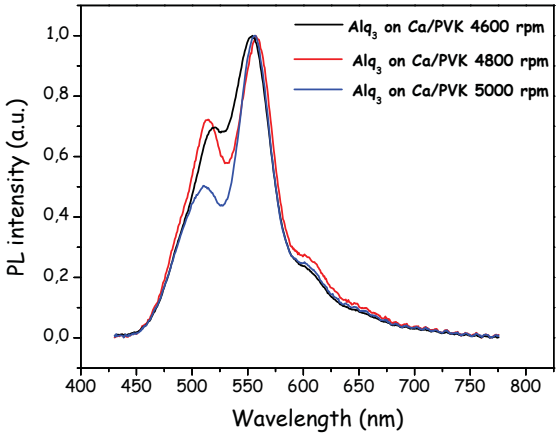

Figure 4.18: Modulation of the PL spectra of ALq3 due to a ML structure composed of 27 layers of CA/PVK; the dielectric layers are deposited varying the spin-coating velocity from 4600 rpm to 5000 rpm.

Furthermore, the second prosed route has been followed by increasing the refractive index contrast in the ML dielectric structure.
The cellulose acetate was substituted with *Cytop*, an amorphous organic fluoropolymer having refractive index n_{Cytop}=1.34; hence, the resulted refractive index contrast with PVK was increased up to $\Delta n_{Cytop/PVK} = 0.34$.
In order to predict the structure-induced photonic effect, we simulated the transmittance spectrum of 5 alternating layers of the two polymers as a function of the wavelength employing the *transfer matrix method* (27).
In the MATLAB simulation, we have considered the system glass/multilayer/air with the light impinging the glass substrate. n_o and n_s are the refractive indexes of the air and glass, respectively, while E_m and H_m are the electric and magnetic fields in the glass substrate.
To determine the electric and magnetic fields in air, E_o and H_o, the following system

has been solved:

$$\begin{vmatrix} E_o \\ H_o \end{vmatrix} = \begin{vmatrix} M_1 & M_2 \end{vmatrix}^{nl} \begin{vmatrix} E_m \\ H_m \end{vmatrix} \tag{4.3}$$

where nl is the number of periods that form the stack and M_j with j=1,2 is the characteristic matrix of each layer:

$$M_j = \begin{vmatrix} cos\phi_j & \frac{i}{n_j} sin\phi_j \\ in_j sin\phi_j & cos\phi_j \end{vmatrix} \tag{4.4}$$

In the case of normal incidence of the probe beam, the phase variation of the wave passing the j fold layer is:

$$\phi_j = \frac{2\pi}{\lambda_o} n_j d_j \tag{4.5}$$

where n_j and d_j are the refractive index and the thickness of the layer j.
By substituting Eq. 4.4 into Eq. 4.3, and using the definition of transmission coefficient, we obtain the formula of the optical transmission (28):

$$T = \frac{4n_s}{n_o(E_o + H_o/n_o)^2} \tag{4.6}$$

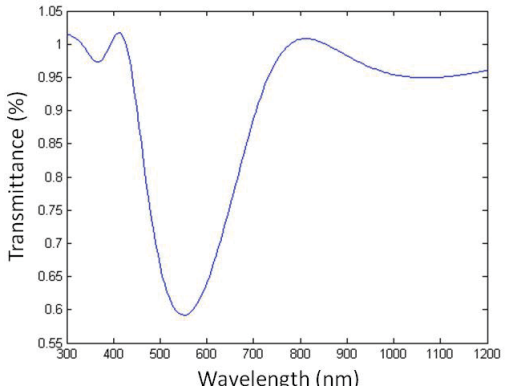

Figure 4.19: MATLAB simulation of the transmittance spectra of 5 layers of Cytop/PVK DBR structure.

The result of the MATLAB simulation, shown in Figure 4.19, highlighted that the periodic variation of the refractive indexes of the dielectric stack made by Cytop and PVK would have induce a 40% decrease in the transmission of light, in correspondence of the peak emission wavelength of the Alq_3 thin film which was considered as recombination layer. Hence, implementing this DBR in a transistor would result in a 40%

increase of a portion of the EL emission in the forward direction.
We have performed many trials to fabricate this specific DBR, though it is not possible to spin coat one polymer on top of the other, since Cytop is only soluble in a special fluorinated solvent, but the wettability of the solution on a PVK layer results very low.

In summary, we have studied the possibility to introduce a full-organic DBR to be used as opto-electronic gate dielectric in an OLET. This structure should be able to maintain the electrical properties of a dielectric and to induce a photonic effect, modifying the EL of the device in emission profile and peak wavelength. Further work is necessary to find a pair of organic materials that can satisfy both the requirements.

4.3.1.2 Next steps

We are currently following a remarkable methodology to fabricate inorganic multilayers with wet chemistry techniques, by depositing metal oxide nanoparticles such as zirconium oxide (ZrOx) and titanium dioxide (TiOx) starting from colloidal dispersions.

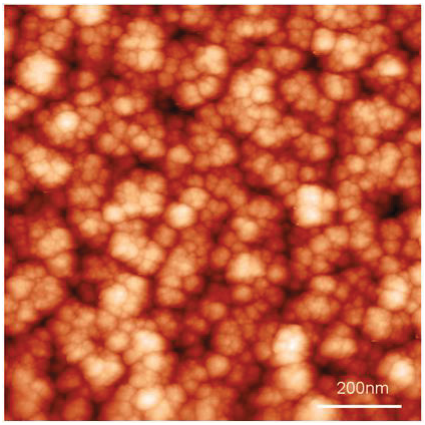

Figure 4.20: AFM topography of a TiOx porous layer; the Z range is 100 nm.

By applying a small external voltage during the deposition of the layers it is possible to modulate periodically the porosity and the thus the dielectric properties of the same oxide materials. Moreover, organic compounds can be inserted between the pores of the nanoparticles in order to form a stratified inorganic/organic hybrid blend.
The transmittance spectrum obtained for two pairs of TiOx layers of different porosity it is shown in Figure 4.21.
The photonic gap result greatly enhanced, thus we are exploring the possibility to insert this inorganic multilayer within the OLET architecture; we use an additional PMMA

layer to be deposited on top of the TiOx stack to improve the dielectric properties of the photonic structure and to obtain a more planar surface.

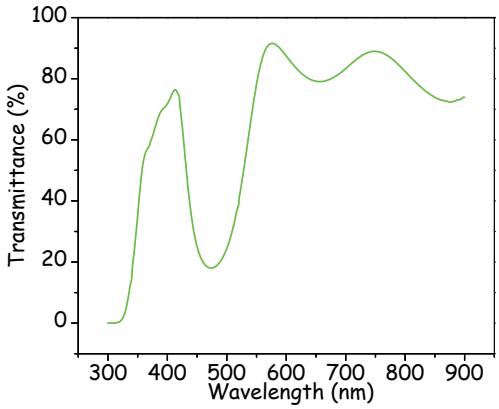

Figure 4.21: Transmittance spectrum of four layers of TiOx stratified photonic crystal.

Another photonic structure that can be inserted into an OLET is a non-planar 1D grating, such as a *Distributed FeedBack* structure (DFB), which will be described in details in Chapter 5.
Although a DFB could offer superior photonic performances with respect to the common multilayer systems, lithographic or UV embossing procedures are necessary to fabricate the grating. Moreover, the introduction of this kind of structure into a field-effect device structure is not trivial given that the semiconductor/dielectric interface has to preserve planarity in order to guarantee efficient charge transport. Nonetheless, different attempts for introducing 1D DFB into the active region of single-layer OLET has been reported (29).
However, given the ease in fabrication of planar alternating layers, DBR remain promising candidate for low-cost technological applications in OLETs.

Bibliography

[1] S.Z.Bisri et al., *Adv.Mater* **23**, 2753 (2011) 63

[2] J.Zamuseil et al., *Adv.Funct.Mater* **18**, 3630 (2008) 63

[3] P.Langevin, *Ann.Chim.Phys.* **7**, 433 (1903) 63

[4] D.L.Smith et al., *Appl.Phys.Lett.* **89** 233519 (2006)

[5] E.Smits et al., *Phys.Rev.B* **76**, 125202 (2007) 63

[6] T.Takahashi et al., *Adv.Funct.Mater.* **17**, 1623 (2007) 63

[7] D.S.H.Charrier et al., *Org.Electron.* **10**, 994 (2009)

[8] S.Toffanin et al., *Laser Photonic Rev.* **7**, 1011 (2013) xii, 63, 64, 65, 66, 67, 69, 70, 72

[9] R.Capelli et al., *Nat.Mat.* **9**, 496 (2010) 66

[10] *Synopsys Inc.*, Sentaurus Device User Guide, F-2011.09, Mountain View, CA, USA (2011) 67

[11] C.L.Mulder et al., *Appl.Phys.Lett.* **90**, 211109 (2007) 68

[12] T.Tsutsui and K.Yamamato, *J.Appl.Phys.* **38**, 2799 (1999) 68

[13] Fluxim AG, Semiconducting emissive thin film optics simulator SETFOS *http://www.uxim.com* 70

[14] B. Perucco et al., *Opt. Express* **21**, A246 (2010) 70

[15] H.G.Peng et al., *J.Appl.Phys* **96**, 1649 (2004)

[16] H. Riel et al., *J.Appl.Phys.* **94**, 5290 (2003) 71

[17] Y.R.Do et al., *J.Appl.Phys* **96**, 7629 (2004) 72

[18] T.Nakamura and N.Tsutsumi, *J.Appl.Phys* **97**, 054505 (2005) xiii, 73

[19] V.Bulovic et al., *Phys.Rev.B* **58**, 3730 (1998)

[20] A.O.Altun et al., *Organic Electronics* **11**, 711 (2010) 73

[21] R.Meerheim et al., *Appl.Phys.Lett* **93**, 043310 (2008)

[22] T. Tsutsui et al., *Adv.Mater* **13**, 1149 (2001) 73

[23] C.Lopez, *Adv.Mater* **15**, 1679 (2003) 73

[24] T.Alfrey et al., *Polym.Eng.Sci.* **9**, 400 (1969) 74

[25] E.B.Namdas et al., *Adv.Mater* **XX**, 1 (2011) xiii, 74, 75

[26] F.Scotognella et al., *Phys.Chem.Chem.Phys.* **12**, 337 (2010) 75

[27] M.Born and E.Wolf, *Principles of Optics*, 7^{th} ed., Cambridge University Press, Cambridge, U.K. (1999) 76, 78

[28] A.Pectu and L.Preda, *Rom.Journ.Phys.* **54**, 539 (2009) 79

[29] M.C.Gwinner et al., *Adv.Funct.Mater.* **19** (2009) 81

[30] F.Scotognella et al., *International Journal of Photoenergy*, Art. ID 389034 (2008)

5

Silk fibroin as active material for photonic structures

Silk spun by spiders and silkworms can be considered as the strongest and toughest natural fibers known, and it has been utilized for centuries for medical sutures.
Nowadays, this widely available natural polymer is inducing renewed interest in various research fields, thanks to its excellent mechanical and optical properties, biocompatibility, biodegradability and implantability; silk has unlimited opportunities of biological integration, functionalization and processing, and it can be used for novel technological applications, such as useful material in realization of photonic structures (1) (2).
Moreover, silk is used as template of biological components (3) and for drug stabilization and release (4) (5). The material has a huge potential to be employed as bio-functional interface in electronic devices that aim to stimulate and control neural network activity, since it has been demonstrated that it support the adherence and neurite outgrowth of dorsal root ganglion neurons, preserving cells biological functions (6).
Furthermore, silk can be used for medical applications, and it shows a controllable degradation lifetime that ranges from weeks to years (7) (8).

5.1 Opto-electronic applications

Silk possesses dielectric properties, and it has been implemented as an efficient gate dielectric in OTFTs and OLETs, as we have recently demonstrated. The device architecture and the electrical characterization of the *n-type* and a *p-type* silk-OFET that have been fabricated in ISMN-CNR laboratory are reporte in Figure 5.1 (10).
To fabricate the device, a 400 nm thick film of silk fibroin was spin-coated from aqueous

solution onto a glass/ITO substrate. Then, a 15 nm thick film of an organic semiconductor (N,N-ditridecylperylene-3,4,9,10-tetracarboxylic diimide (P13) for *n-type* OFET or α,ω -dihexyl-quaterthiophene (DH4T) for *p-type* OFET) was vacuum deposited on top of silk film. After that, 50 nm thick source and drain gold contacts were deposited by thermal vacuum sublimation through a metal mask, thus completing a top-contact organic field effect transistor.

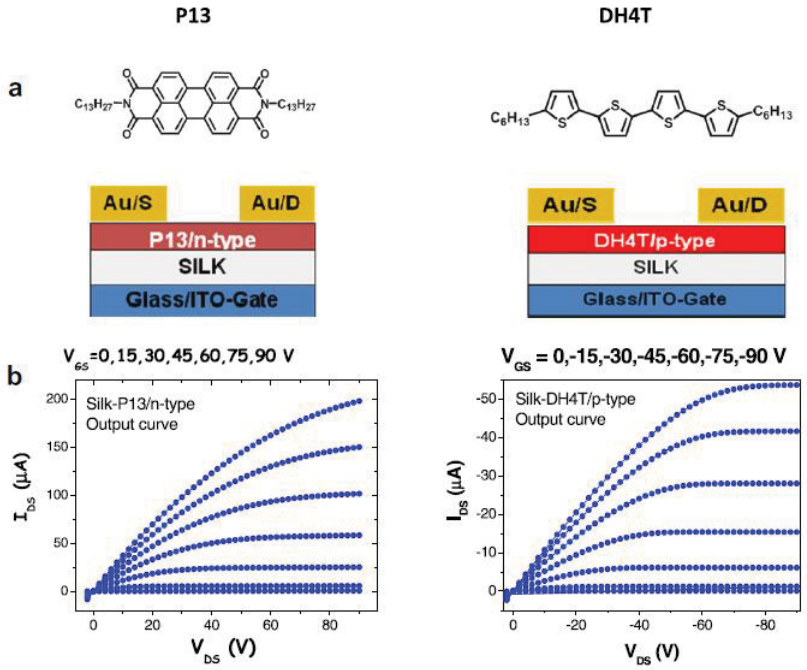

Figure 5.1: (a) Molecular structures, device architecture and (b) electrical characterization of n- and p-type silk-OFET (10).

These devices show the typical field-effect transport behavior of *n-* and *p-type* organic semiconductors, and the obtained charge mobility values are comparable to the ones of thin film OFETs reported in literature (11).
Indeed, the implementation of silk as gate dielectric in flexible electronic is a step toward a more eco-sustainable manufacturing process, that opens the way towards the development of multifunctional optoelectronic devices which in perspective can be made fully biocompatible and biodegradable.

5.2 Silk purification process

The silk wire is composed of two kinds of protein: a fibrous one (named *silk fibroin*) that forms the thread core of the fiber and represent the 70-80% of raw silk fiber mass, and a glue-like one (named *sericin*) that surrounds the fibroin fibers to stick them together.

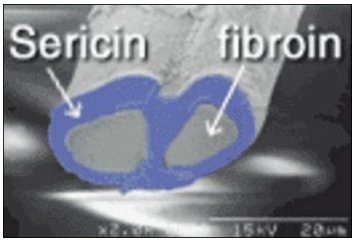

Figure 5.2: SEM image of silk wire.

In order to obtain silk substrates suitable for photonic application, we defined and optimized a specific protocol for extracting silk protein from *Bombix Mory* silkworm cocoons, and for processing the raw material from purification to spin-coating thin-films. The protocol was optimized in collaboration with IBIMET and ISOF institutes at CNR in Bologna.
In particular, an easy *de-gumming* process, that consists of boiling the cocoons in an alkaline solution (see Figure 5.3 step 1) enables to remove sericin from silk, since this protein causes inflammatory responses in humans and prevents the solubilization of the fibers. Therefore, silk fibers can be dissolved (in 9.3M lithium bromide) into an aqueous solution (step 2), which is then purified by removal of the salt by dialysis (step 3). The resulting solution, named *Regenerated Silk Fibroin* (RSF), can then be used as the building block and turned into different forms, ranging from gels and sponges to blocks and films (6).

Figure 5.3: Silk fibroin purification steps.

5.3 Photonic applications

Silk fibroin can be used to produce films (also free standing) that result very attractive for optic and photonic applications, thanks to their transparency, uniformity and surface flatness. Moreover, the capability of the material to replicate patterned substrate features on a length scale comparable to the wavelength of visible light, opens the way to the fabrications of photonic structures as silk diffraction patterns, waveguides and microlens arrays (12) (13).

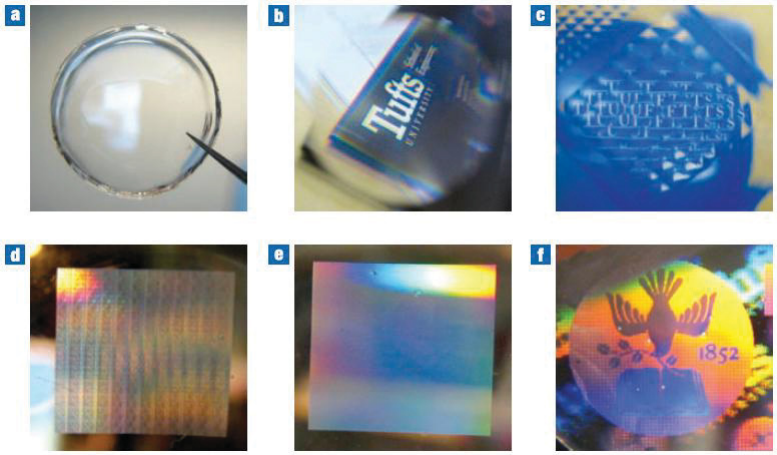

Figure 5.4: Examples of free-standing, 50 μm-thick, optical silk elements. a) a clear film; b) an image through a 1 cm-diameter lens with 60 mm focal length; c) an image through a 66 microlens array; d) a two-dimensional diffractive optical element; e) a 600-grooves-per-millimeter diffraction grating and f) a white-light hologram (1).

In addition, suitably-doped silk can be used as active photonic component, as we have demonstrated in ISMN-CNR institute, by implementing a *Distributed Feedback* (DFB) structure capable of laser emission (14).
The basic working principles of this typology of photonic structures will be introduced in the next section.

5.4 DFB structures

A Distributed Feedback structure is a linear grating fabricated with a gain material. The periodic spatial variation of the refractive index n (or of the gain constant α) of the gain material on a length scale comparable to the wavelength of light, induces backward and forward Bragg scattering of light passing the structure, and thus providing optical

feedback (15).

$$n(z) = n + n_1 cosKz \tag{5.1}$$

$$\alpha(z) = \alpha + \alpha_1 cosKz \tag{5.2}$$

In equations 5.1 and 5.2, are indicated the modulations of the refractive index n or of the gain constant α as a function of the spatial coordinate z; n_1 and α_1 are the modulation amplitudes, while $K = 2\pi/\Lambda$, and Λ indicates the period of the spatial modulation (see Figure 5.5).
A DFB structure will induce optical feedback in the vicinity of a wavelength λ_B given by the Bragg condition:

$$m\lambda_B = 2n\Lambda \tag{5.3}$$

where m is the diffraction order that characterize the direction of the emission with respect to the grating substrate (m=1 parallel emission, m=2 perpendicular emission).

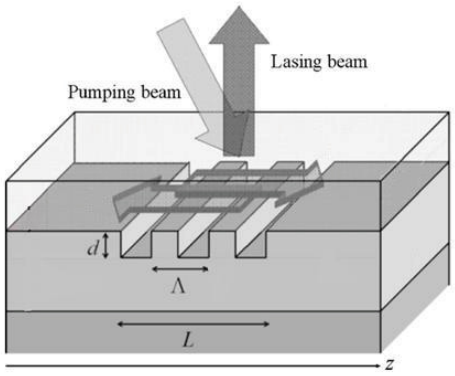

Figure 5.5: Schematic diagram of a DFB laser structure.

The first demonstration of this kind of laser was obtained with a periodic structure made with gelatin and rhodamine 6G, developed by Kogelnik and Shank in 1970 (16). The inventors derived the expressions for the stimulated emission from a coupled-wave analysis of the electromagnetic waves, and assumed that the field E in the device was of the form:

$$E = R(z)e^{-jKz/2} + S(z)e^{jKz/2} \tag{5.4}$$

where $R(z)e^{-jKz/2}$ and $S(z)e^{jKz/2}$ are two counterrunning waves with complex amplitudes R and S, that feed energy into each other due to the modulation of n or α.

A DFB structure allow to obtain a more compact laser-emitting structure with respect to the standard lasers fabricated with the two mirrors configuration, and the use of silk as building material can bring the advantage of the biocompatibility.

5.4.1 Silk/stilbene DFB structures

Silk proteins in solution are expected to be fluorescent given the presence of fluorophores aromatic aminoacids (i.e. tryptophan, tyrosine, phenylalanine) whose emission spectra are strictly correlated to the protein structural conformations (17) (18).
Despite this, the material has to be blended with a gain medium, to obtain the suitable photonic properties necessary to implement a DFB structure.
For this purpose, we have chosen Stilbene 420 from *Coherent Inc.* (molecular structure in Figure 5.6), a small molecule belonging to the subgroup of azo dyes that has shown to have high photoluminescence quantum yield (QY) and low-threshold for optical gain, which is ideally compatible for blending with silk thanks to its water solubility.
The resulting blend is a water solution with 95% QY, that can be spin-coated onto the desired substrate.

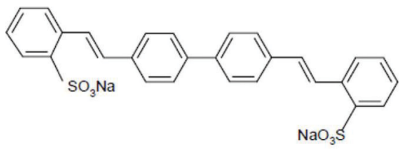

Figure 5.6: Molecular structure of stilbene 420.

The absorption and PL emission spectra of stilbene dispersed in water solution and stilbene-doped silk film are reported in Figure 5.7. With respect to the solution, the film shows a slightly redshifted absorption spectrum and a more structured PL emission profile; this behavior is consistent with the possible conformational stabilization of dye molecules in the solid matrix.

5.4.1.1 Fabrication process

To fabricate a DFB laser presenting this blend as gain material, we have exploited silk capability to replicate patterned substrate features in a range comparable with the wavelength of visible light. Indeed, we have produced a Si/SiO_2 nanopatterned grating

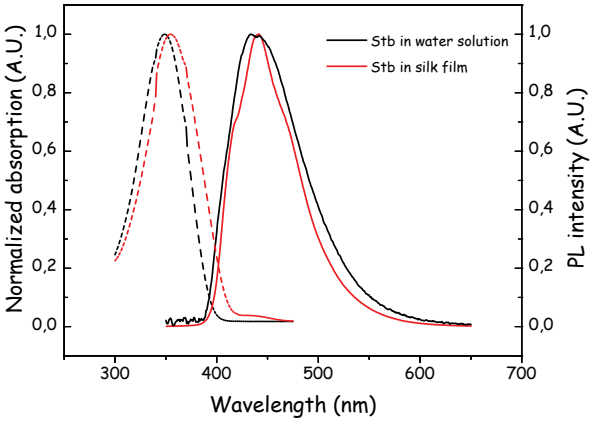

Figure 5.7: Absorption (dashed line) and photoluminescence emission (solid line) of stilbene in water solution and in silk film at 5 wt%.

with a grating period Λ=265 nm, 270 nm and 275 nm.
The grating period was chosen according to Bragg law (eq. 5.3) in order to achieve overlapping of the lasing wavelength λ_B with the gain spectrum of the stilbene dye. To obtain normal-to-surface emission, the diffraction order m was selected equal to 2.

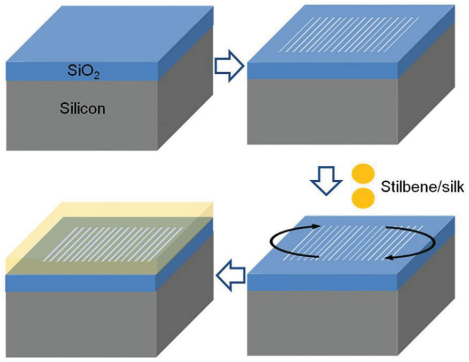

Figure 5.8: Sketch of the procedure for the fabrication of silk/stilbene DFB laser.

The gratings were made starting from a silicon dioxide film, deposited with a thickness of 1.5 μm on a silicon wafer, using a plasma enhanced chemical vapor deposition system. Then, a 1.5 μm thick layer of PMMA resist was spin-coated on the SiO_2 film and 1D grating patterns with 40% and 50% duty cycle were generated by electron-beam lithography onto this layer. The grating pattern was transferred onto the SiO_2 film via reactive ion etching tools and silk/stilbene solution was spin-coated on top of it; the

thickness of the silk/stilbene film was about 1.6 μm.
The fabrication steps of the process are resumed in Figure 5.8, whereas an AFM topography of the resulting structure is shown in Figure 5.9.
From this image it is possible to note that the nanopatterned silk grating results very regular.

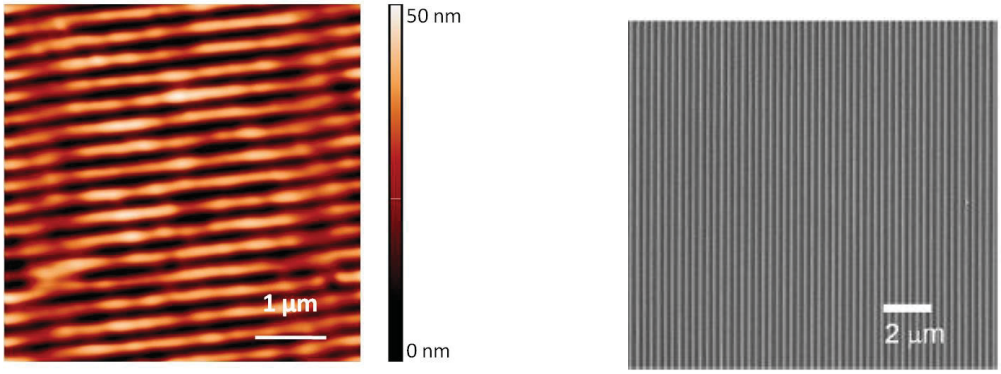

Figure 5.9: AFM image of silk/stilbene grating and SEM image of the grating mold.

5.4.1.2 Optically pumped silk/stilbene lasing

The lasing characterization obtained from stilbene-doped silk DFB gratings with different periods are reported from Figure 5.10 to Figure 5.12. The setup used to perform the measurements is described in Chapter 6.

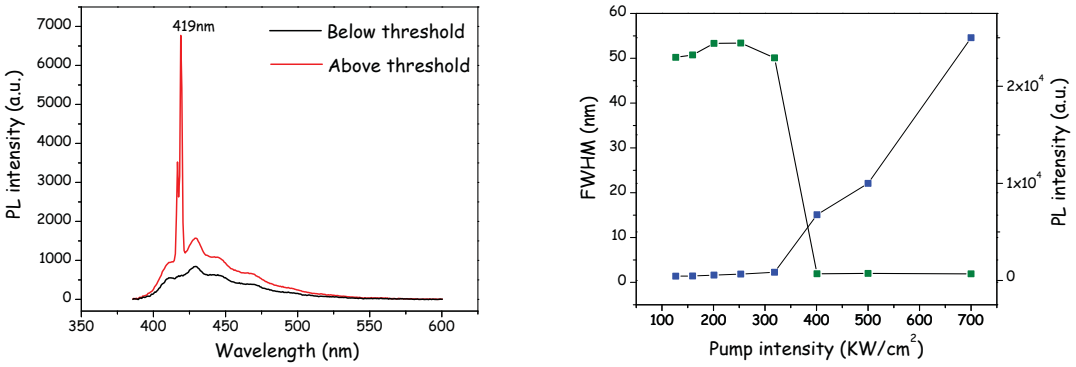

Figure 5.10: Emission spectra of a silk/stilbene grating with Λ=265nm, detected at excitation pump power below and above lasing threshold (left). Dependence of the FWHM and emission intensity on the excitation pump intensity (right); the lasing threshold is 400 KW/cm^2.

In the left part of the images, the emission spectra of silk/stilbene gratings are shown: for pumping below lasing threshold, stilbene emission is broad with a FWHM of about 60 nm; the emission is also partially modulated by internal reflections in the SiO_2/silk/air waveguide slab. For pumping above the lasing threshold a narrow peak emerges with the FWHM value approaching 1 nm.

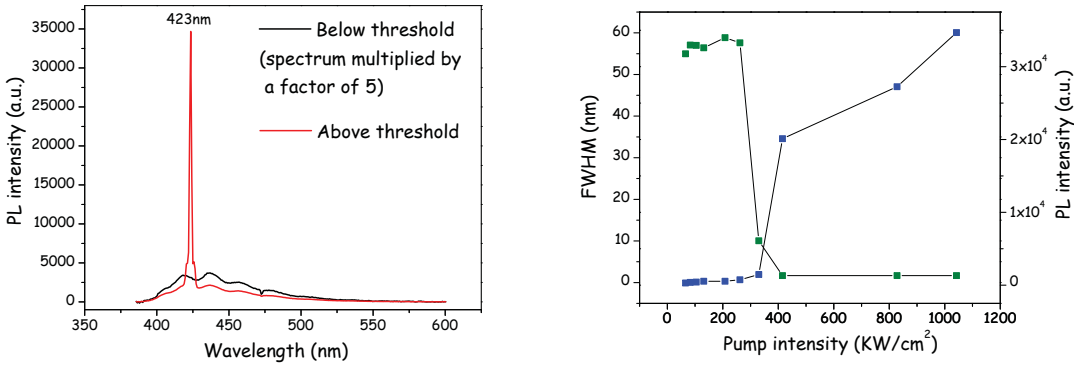

Figure 5.11: Emission spectra of a silk/stilbene grating with Λ=270nm. The lasing threshold is 400 KW/cm^2) .

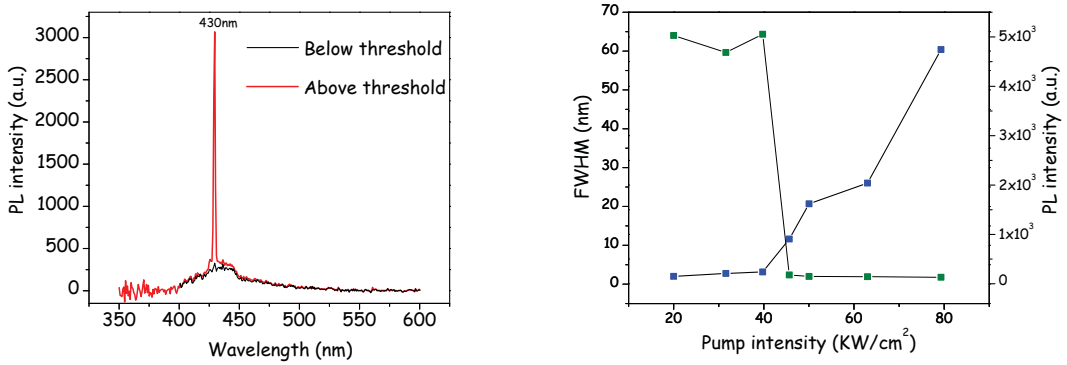

Figure 5.12: Emission spectra of a silk/stilbene grating with Λ=275nm. The lasing threshold is 45 KW/cm^2) .

The lasing threshold is defined by plotting the *Full Width at Half Maximum* (FWHM) of the emission spectra and the emission intensities as a function of pump intensity, as it is shown in the right part of Figures 5.10-5.12.
The threshold value can be visually defined as the pump power for which the FWHM abruptly decrease and the output intensity exponentially increase.

We observe that stilbene lasing wavelength is grating-dependent, since it is red-shifted when the lattice constant of the grating increases, in well accordance with the Bragg's law. Thanks to this evidence it was possible to calculate the refractive index of the blend, as it is reported in Table 5.1.

Table 5.1: Dependence of stilbene lasing wavelength λ_B on the grating periodicity Λ. The refraction index values n calculated from the Bragg's law are reported.

Λ(nm)	λ_B(nm)	n
265	419	1.58
270	423	1.56
275	430	1.56

The threshold values obtained for the different grating step sizes are resumed in Table 5.2.
The lowest lasing threshold is obtained for the 275 nm-grating (see Figure 5.12); in this case, the lasing peak is shifted to a wavelength of 430 nm, that is nearer to the highest gain region of stilbene than the emission peak collected for the other gratings.
Indeed, in single-component gain material, the highest gain region of a medium is usually located in the low energy side of the PL spectrum, far from the absorption edge that would introduce self absorption.

Table 5.2: Lasing threshold values (L_{th}) obtained for the different grating step sizes.

Λ(nm)	L_{th}(KW/cm^2)
265	400
270	400
275	45

The reduction of the emission FWHM to 1 nm and the correlation between lasing wavelength and grating step size, rule out the possibility that the amplification behavior we observed in these measures is due to *Amplified Spontaneous Emission* (ASE), a phenomena already described in Chapter 2.
To have a direct comparison between these two phenomena, we have performed ASE measurements on silk/stilbene films, which were spin-coated in the same conditions

used for the grating but on a flat Si/SiO_2 surface.
For these films the emission peak is red-shifted towards the maximum gain region of stilbene, and the FWHM of the peak is only reducing down to 10 nm, as it is shown in Figure 5.13.

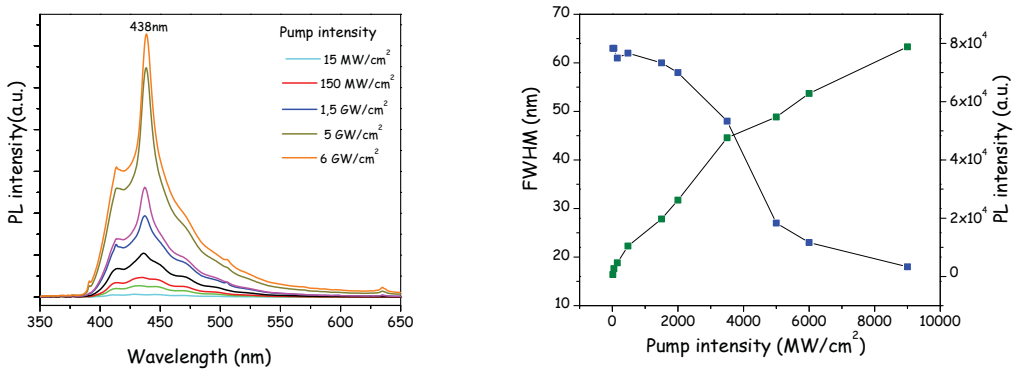

Figure 5.13: ASE measurements performed on silk/stilbene film without grating pattern.

To conclude, we can state that the emission obtained from silk/stilbene DFB gratings was a laser emission.
It is important to underline that the threshold value achieved for the 275 nm-grating (45 KW/cm^2) is almost an order of magnitude lower than those reported for other stilbene-based DFB lasers (20) and two orders of magnitude lower with respect to thresholds obtained from other biocompatible polymers implemented as dispersing matrix for organic lasing dyes, e.g. DNA-CTMA based thin-films (21).
It is evident that the specific chemical-physical interaction between silk and stilbene plays a fundamental role in determining the good photonic properties of the silk-based lasing system (14). In particular, the repulsive electrostatic interaction between the negatively charged stilbene moieties (originated by the SO_3^- anion) and the chains of the silk fibroin, endowed with both acid an basic functional groups (22), could favorably affect the molecular rearrangement of the lasing dye.
Another motivation that possibly justifies the dye stabilization in silk is related to the viscosity of the matrix, that prevents the rotation of the functionalized benzene units around the double bond in the molecule exited state, thus avoiding the stilbene isomerization (represented in Figure 5.14) that can be responsible for fluorescence quenching (23).

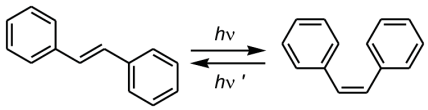

Figure 5.14: Stilbene trans-cis isomerization.

5.4.1.3 Towards optical biocompatible lab-on-a-chip

The nanopatterned silk/stilbene structures can enable novel non-linear detection and imaging schemes, and can be implemented as biological lasers compatible with the support, adherence and outgrowth of cells.
Moreover, the possibility to incorporate biocompatible organic and inorganic dyes in silk matrix can be useful for the realization of label-free optical detection. Indeed, the variation of silk refractive index upon exposure to specific environment or analytes would induce the variation of silk laser characteristics, according to the Bragg's law.
In addition, we can implement silk-based photonic structures in portable lab-on-a-chip devices by patterning directly the photonic lattice on silk thin films. The nanopatterned films can be made also free standing, as it is shown in Figure 5.15.
The final goal is the realization of a silk fibroin high throughput lab-on-a-chip device apt to optofluidic biodiagnostic based on fluorescence detection.

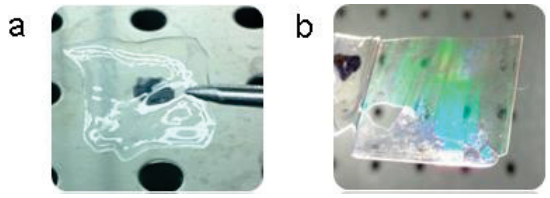

Figure 5.15: Images of free standing silk films fabricated at ISMN-CNR: a) with a flat surface, b) with a patterned DFB structure .

Since the doping procedure is necessary to endow silk with active optical properties so that to be used in laser structures, it is possible to explore innovative route to obtain colored silk, as it will be explained in the next section.

5.5 Silk natural doping

The process of blending silk with an optically active material includes post-production steps necessary to remove excess dye molecules and eventually to restore the properties of silk that are altered during doping.
For these reasons different research groups are trying to obtain intrinsically colored silk,

either by genetically modify the silkworms to get artificially-colored silk proteins (24) or by feeding the silkworm with a dye-added artificial diet (25).
The latter method results very interesting since the doping procedure is sustainable and eco-friendly, and it is possible to take advantage of the biological incorporation of the dye in silk matrix. Moreover, this technique is applicable at large scale production and the obtained colored silk presents optical properties which are under control and statistically reproducible.
Within the consortium concerning the *SILK.IT* project (an Italian Factory of the Future project that aim at developing methods to use silk fibroin for advanced biotechnological applications) a study on silk natural doping has been performed, in strictly collaboration with ISOF and IBIMET institutes at CNR in Bologna.
Three cultures of silkworms have been fed with different dyes, and PL spectroscopy tools have been used to test the effective incorporation of dye molecules; indeed, the dyes posses strongly emitting moieties whose spectral features are strictly correlated to the chemical and physical interaction with the dispersing matrix.
The spectroscopic investigation was performed at every single step along the silk purification route: from the modification of the diet, to the extraction of proteins from different location of the silkworm glands, to the production of regenerate silk fibroin solution.

5.5.1 Silkworm diet protocol

The dye-added lyophilized diet was provided by the *Experiment Institute for Agrarian Zoology* of Padua, whereas the silkworms feeding was performed at the IBIMET-CNR in Bologna.

Figure 5.16: *Bombyx mori* silkworms and cocoons naturally functionalized with different dyes (Rhodamine B, Egyptian blue and Stilbene 420).

The colored cocoons and the *Bombix mory* silkworms fed with Stilbene 420, Egyptian blue and Rhodamine B are shown in Figure 5.16.

Aside from the change of color, we have noted no other differences in naturally-functionalized silk mechanical properties with respect to standard-diet silk.
Although the intrinsic doping of silk with rhodamine B gave us very interesting results, this thesis will be focused only on naturally-functionalized silk based on stilbene, in order to have a direct comparison with the extrinsically doped silk/stilbene blend reported in the previous section.
The intrinsically colored silk was obtained from a population of 50 silkworms; for preparing the diet, 100 g of dried mulberry powder, 260 ml of water and 0.5 g (or 1 g) of stilbene dye were mixed together, cooked in an autoclave for about 40 minutes at 105°C and kept in the refrigerator. The larvae were reared in controlled conditions (26) and fed with the artificial diet until 2^{nd} day of 5^{th} instar to their spinning.
The fibroin extraction from the middle division of silk gland was performed according to Hossain et al. (27), while the posterior parts of the gland were treated according to Mandal and Kundu (28).

5.5.2 Photoluminescence spectroscopy investigation

The photoluminescence spectra were collected from the raw silk fibre, from sericin and fibroin solution extracted from silk glands and finally from regenerated silk fibroin solutions.

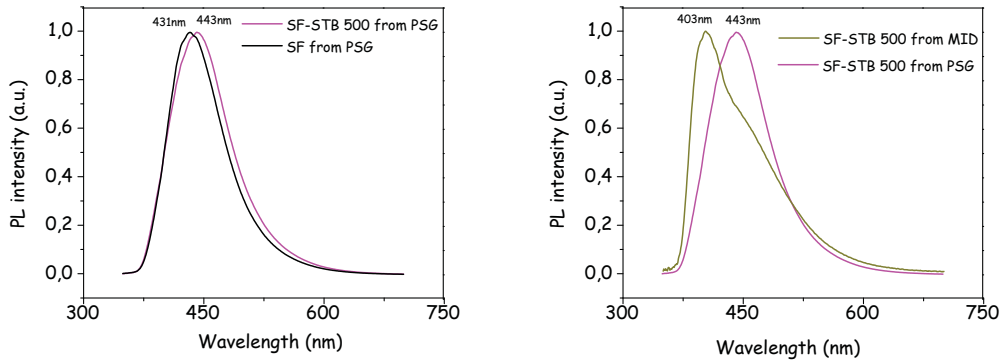

Figure 5.17: PL spectra of silk fibroin extracted from the posterior (left) or middle part (right) of silk glands of larvae fed with 500 mg of stilbene. The spectrum of silk fibroin extracted from the posterior part of the glands of larvae having a standard diet is reported as reference (black line).

Moreover, in order to quantify the effective incorporation of stilbene molecules and to verify whether the amount of the dye in the gland-extracted fibroin was reduced

during the process of reeling and degumming, photoluminescence Quantum Yield (QY) measurements have been performed inside an integrating sphere with a diode-laser at 375 nm as excitation source, as it is described in Chapter 6.
The PL spectra of silk fibroin extracted from gland posterior and middle parts of larvae which were fed with 500 mg of stilbene amount, are reported in Figure 5.17 (the solutions are labeled *SF-STB 500 from PSG* and *SF-STB 500 from MID*, respectively). The corresponding PL spectra of silk fibroin extracted from the glands of larvae having a standard diet are reported as reference (black line labeled *SF from PSG*).
The STB-doped spectrum obtained from the posterior part of silk glands did not show a clear variation in the emission peak wavelength or modulation in the PL profile with respect to the no-doped spectra. Though, a slight increase in the QY values has been obtained when stilbene is included in the silkworm diet (see Table 5.3).
In contrast, when going from the posterior to middle parts of glands (see right part of Figure 5.17) the PL emission spectra were blue-shifted and more structured with respect to the one obtained from the posterior part of the glands. We suppose that the different spectral feature is related to a different conformational arrangements of stilbene molecules in this portion of the glands, where silk fibroin is accumulated.

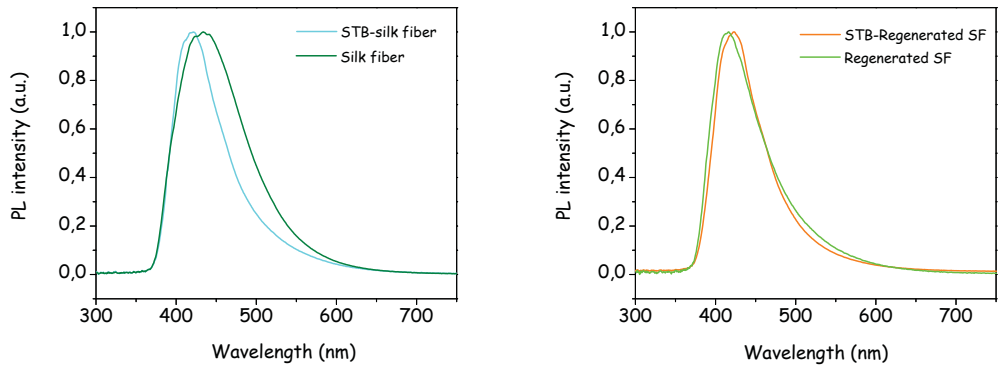

Figure 5.18: Photoluminescence spectra of the fibre (left) and of fibroin regenerated solutions (right) produced by worms fed with stilbene compared to the one produced from worms having a standard diet.

In order to comprehend in more details the possible mechanism of release-out of the dye molecules after the silk production in the glands, in Figure 5.18 are shown the PL spectrum collected from the raw fibre (labeled *STB-silk fiber*), and the spectrum collected from the regenerated silk fibroin solution of silkworm fed with stilbene (i.e. extracted and purified silk fibroin obtained from the cocoons, labeled *STB-regenerated*

SF), compared with the no-doped samples (labeled *Silk fibre* and *Regenerated SF*, respectively).
Interestingly, we observed a reduction of the full-width-at-the-half-maximum value in the raw fibre PL spectrum once stilbene was included in the silkworm diet. This datum is consistent with a possible higher alignment of the emissive moieties (regardless they are either the fiber proteins or the stilbene molecules) once the dye is included within the protein structure.
In the case of the regenerated solutions, the PL spectral features of fibroin solutions were almost invariant with respect the doping procedure. This evidence can be correlated to the intrinsic emission of silk, visible in Figure 5.19.
Do that, steady state PL spectroscopy cannot satisfactorily discriminate itself if dye molecules are released out during the procedure for obtaining regenerated naturally-doped silk.

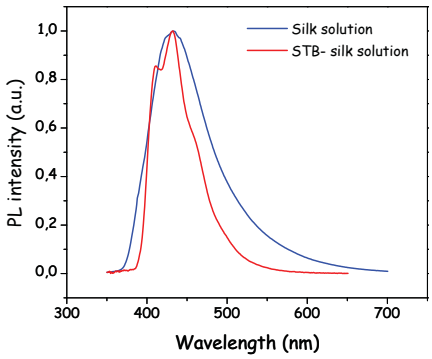

Figure 5.19: Photoluminescence spectra of silk in water solution and of stilbene/silk blend in water solution.

In summary, we can state that a reproducible modulation of the naturally-doped silk fibroin PL spectra is evident in the silkworm gland, according to the fact that the protein is extracted either from the middle or the posterior glands.
Aside from this evidence, no other relevant variation of the emission spectra are caused by the presence of stilbene, given the overlapping of the PL spectra of stilbene molecules and the one of fluorophore moieties in silk. In particular we do not observe the characteristic emission profile of stilbene/silk blend.
The most clear benchmark of the dye-added artificial diet is a systematic and valuable increase of the QY, that is present regardless silk extraction position, as it is reported in Table 5.3.

Comparing the data, it is possible to note that increasing by twice the amount of stilbene dispersed in the diet induces only a small variations in the QY of the solutions. This experimental evidence is likely to be correlated to the fact that the amount of stilbene we introduced in the silkworm diet was exceeding the maximum to be up-taken by the larvae.
Moreover, since the QY of stilbene-doped sericin exhibits an increase with respect to the one of the undoped sericin, stilbene molecules might be present also in this part of silk that is rejected during the purification process, and not only in the commercially valuable part of silk (fibroin).

Table 5.3: Photoluminescence QY of *Silk Fibroin* (SF) obtained from worms fed with stilbene.

QY (%)	Without STB	With 0.5 g of STB	With 1 g of STB
SF from posterior glands	1.8	4.4	5.7
SF from middle glands	1.8	5.6	//
SF regenerated solution	1.3	4.6	//
Sericin regenerated solution	1.6	4.0	//

In conclusion, it is evident that the increase of the QY values is consistent with the presence of stilbene in worms diet, but the obtained enhancement is not enough to use this material to produce active photonic structures such as the one previously reported. This fact can be partially related to the high hydrophylicity of the dye that is released out of the silkworms body.
Moreover, it is clear that the chemical structure of stilbene molecules is not tuned to avoid the accumulation of the dye in the parts of silk that are rejected during purification (i.e. sericin).
Hence, we can state that natural doping is a very interesting procedure to obtain intrinsically colored silk, but the choice of the suitable dye has to take into account different molecular factors such as the structure-dependent hydrophobicity and self-assembly capability of the molecules and of the silk proteins. These factors can determine the uptake of the substance into the polymer.
Further work is necessary the design lasing dyes that result more efficient when inserted in silkworms diet.

5. SILK FIBROIN AS ACTIVE MATERIAL FOR PHOTONIC STRUCTURES

Bibliography

[1] F.Omenetto and D.L.Kaplan, *Nat.Phot.* **2**, 641 (2008) xiii, 85, 88

[2] Lindsay S.Wray et al., *Society for biomaterials*, 89 (2011) 85

[3] H.Tao et al. *Adv.Mater*, 1 (2012) 85

[4] V.Benfenati et al., *Biomaterials* **31**,7883 (2010) 85

[5] A.Wiltz et al, *Biomaterials* **29**, 3609 (2008) 85

[6] V.Benfenati et al., *Adv.Funct.Mat* **22**, 1871 (2012) 85, 87

[7] Y.Yang et al., *Biomaterials* **28**, 5526 (2007) 85

[8] S.Madduri et al., *Biomaterials* **31**, 2323 (2010) 85

[9] C.H.Wang et al., *Adv. Mater.* **23** (2011)

[10] R.Capelli et al., *Organic electronics* **12** (2011) xiii, 85, 86

[11] F.Dinelli et al, *Adv. Mater.* **18**, 1416 (2006) 86

[12] J.P.Mondia et al., *Adv.Mat* **22**, 4596 (2010) 88

[13] S.D.Parker et al., *Adv.Mater* **21**, 1 (2009) 88

[14] S.Toffanin et al., *Appl.Phys.Lett.* **101**, 091110 (2012) 88, 95

[15] G. Kranzelbinder and G.Leising, *Rep.Prog.Phys.* **63**, 729 (1999) 89

[16] H.Kogelnik and C.V.Shank *Appl.Phys.Lett.* **18**, 152 (1971) 89

[17] I. Georgakoudi et al, *Opt.Exp.* **15**, 1043 (2007) 90

[18] Xin-Gui Li et al., *Biopolymers* **89**, 497 (2007) 90

[19] I.D.W.Samuel et al., *Nat.Phot.* **3**, 547 (2009)

[20] K.Yamashita et al., *Appl.Phys.Lett.* **92**, 243306 (2008) 95

[21] L.Sznitko et al., *Appl.Phys.Lett.* **99**, 031107 (2011) 95

[22] F.P.Seib et al., *Biomaterials* **33**, 1017 (2012) 95

[23] D.Tzeli et al., *J.Am.Chem.Soc.* **134**, 4346 (2012) 95

[24] T.Iizuka et al., *Adv.Funct.Mater.*, 10.1002/adfm.201300365 (2013) 97

[25] N.C.Tansil et al., *Adv.Mater.*, **23**, 1463 (2011) 97

[26] L.Cappellozza et al., *Appl.Entomol.Zool.* **40**, 405 (2005) 98

[27] K.S.Hossain et al., *Biomacromulecules* **4**, 350 (2003) 98

[28] Mandal and Kundu, *Biotechnology and Bioengineering* **99**, 1482 (2007) 98

[29] J.DeMello and H.F.Wittmann, *Adv. Mat.* **9** (1997) 111

6

Experimental section

This chapter includes a description of the experimental techniques used to fabricate OLETs, DBR and DFB structures, and to characterized their opto-electronic and photonic properties.

6.1 Film deposition

6.1.1 Spin coating

Spin-coating is a deposition process in which a solution is deposited onto a substrate placed on an horizontal rotating disc, as it is sketched in Figure 6.1.

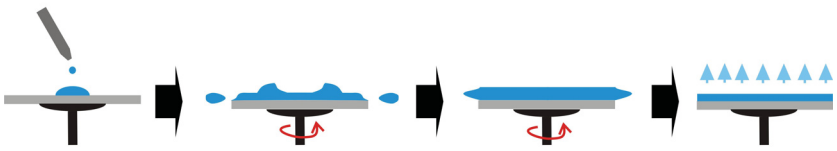

Figure 6.1: Sketch of spin-coating deposition process.

The sheering of the liquid causes a radial flow in which almost the 99% of the material is quickly ejected from the substrate (1); the ejection and evaporation of the solvent leaves a highly uniform film, with a controllable and reproducible film thickness.
The physical parameters that influence the deposition are the centrifugal force of the rotating disk, the viscosity of the fluid and the adhesive forces at liquid-substrate interface.

The thickness is dependent on the solution viscosity, angular velocity, angular acceleration spin time and solution concentration, whereas the solution volume does not strongly influence it.

6.1.2 Physical Vapor Deposition

Physical Vapor Deposition (PVD) is a process in which atoms or molecules from a thermal vaporization source reach and impinge a substrate placed in a vacuum chamber. The main advantages of this technique consist of providing sub-monolayer thickness control during deposition and low level of contamination due to moisture or impurities. Moreover, this technique allows the use of masks to define the area of growth (*line-of-sight deposition*), and to obtain a wide range of deposition rates.
On the other hand, sometimes the line-of-sight deposition gives poor surface coverage and poor uniformity over a large surface area, and the process loads high radiant heat. Another drawback of this technique is the impossibility of processing polymers and, in general, high molecular weight materials.

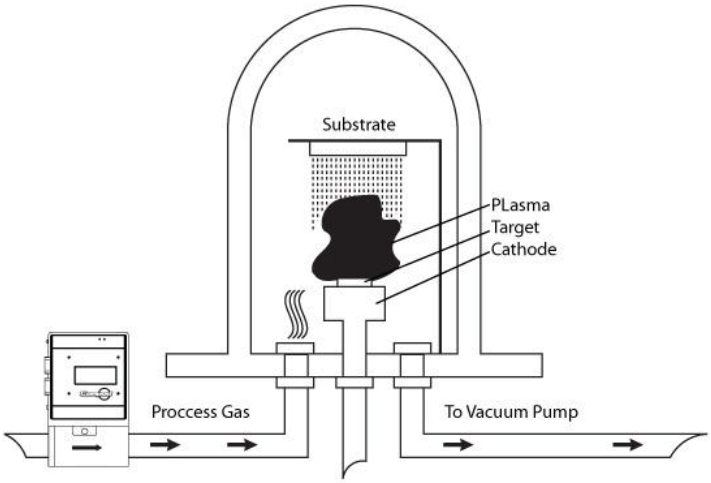

Figure 6.2: Scheme of a vacuum evaporation chamber.

A typical vacuum evaporation chamber is equipped with a vacuum pump, a crucible (where the material is held and heated to sublimate), a heater cell in which the crucible is placed, a substrate mount (also called target), a shutter to control the open/close processes of the substrate target and a quartz crystal micro-balance for measuring the film thickness (see Figure 6.2).
Once the crucible is filled with the material, it is heated since it reaches the sublimation temperature. Then, after having opened the shutters, the sublimed materials exits the

crucible and reach the target, where is deposited onto the desired substrate.
In this PhD thesis two different sublimation systems were used, one home-made and the other a custom-made by *Kurt J. Lesker*. Both the systems were connected to glove boxes in order to avoid moisture contaminations in every step of organic thin-film and device fabrication.

6.2 Opto-electronic characterization

6.2.1 Probe station

For performing opto-electronic device characterization of OLETs immediately after fabrication, a *Süss PM5 Analytical Probe System* was used (see Figure 6.3).

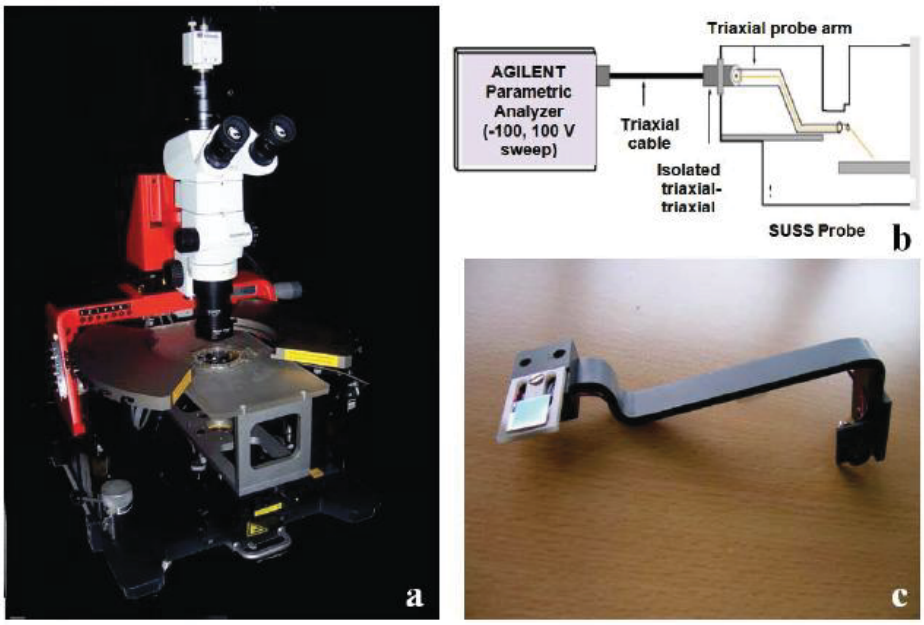

Figure 6.3: a) Süss PM5 Analytical Probe System. b) Scheme of the triaxial cable connection between the Semiconductor Device Analyser and the Analytical Probe System. c) Hamamatsu photodiode used for electroluminescence measurements.

The set-up is placed in a nitrogen-atmosphere glove-box system to avoid the interaction of the device with air moisture and oxygen, that have a very detrimental effect on their opto-electronic characteristics.
The voltage and low-current signals are applied and collected by tungsten tips using an *Agilent* B1500A *Semiconductor Device Analyser*, which is a modular instrument that supports both I-V and C-V measurements; it presents extremely low-current,

low-voltage, and integrated capacitance measurement capabilities with a measurement resolution of 0.1 fA/0.5 μV.
For locating accurately the tungsten tips on the three device electrodes a 70x- magnification optical microscope is mounted vertically on the base plate. Manual probeheads connected to triaxial wires are magnetically blocked onto the plate.
The triaxial-chuck connection (Figure 6.3 b) is created to minimize the chuck leakage current; it is guarded and completely separated from the base machine by a Teflon insulation.
In addition, the devices electrical properties can be correlated to thir EL because of the presence of an *Hamamatsu* photodiode (S1337) placed in the proximity of the device active area.

6.2.2 Electroluminescence angular emission profile setup

In the home-made setup that was built-up for the collection of the trilayer OLET angular emission profile, the sample was mounted on an *Physic Instrument* high precision servo-motor rotational stage located in front of a chopper device, as it is sketched in Figure 6.7.

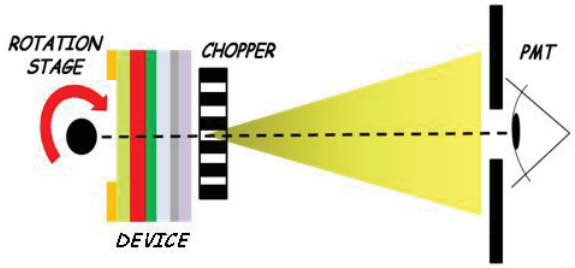

Figure 6.4: EL angular emission profile configuration.

A phase-sensitive *Stanford Research Systems* SR 830 lock-in amplifier was connected to the chopper to guarantee high sensitive measurements.
The EL signal of the device was collected as a function of the angle by a R928 *Hamamatsu* pre-amplified photomultiplier tube (PMT). The instruments communicated through an home made *Labview* software, that correlated the angular position of the rotating device with the PMT voltage signal.

6.3 Optical characterization

6.3.1 Confocal Laser Scanning Microscope

A confocal microscope is an optical microscope where light from a point source probes a very small region of the sample, and a point detector ensures that only light from the very same small volume is detected.

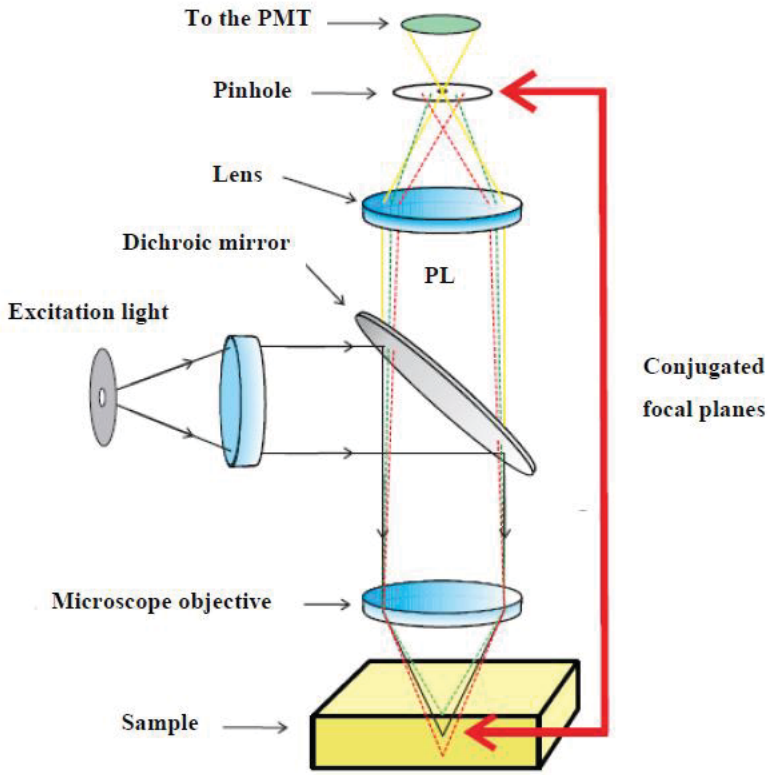

Figure 6.5: Schematic diagram illustrating the operation principle of a confocal microscope.

Figure 6.5 shows a simplified scheme of the working principle of this kind of microscope, that is used for light emitting samples.
The excitation light is reflected by a dichroic mirror and focused by the objective lens on the sample. The PL is recollected by the objective and focused on the spatial filter (pinhole) that prevents the out-of-focus PL rays to reach the detector, that is located in a plane conjugated (confocal) with the point source.
Thus, confocal microscopy is able to reject features that are out of focus, and presents two main advantages with respect to conventional microscopy: *i)* the possibility to

perform optical sectioning and 3-D reconstruction of the emitting specimens and *ii)* an increased in-plane spatial resolution (2).
Since only a diffraction limited point is imaged, the sample or the exciting light must be scanned in order to obtain an image of the desired field of view.
The confocal laser scanning microscope used in this PhD thesis consists of an inverted microscope *Nikon Eclipse TE-2000-E* equipped with a confocal scanning head.
The microscope has a series of *Nikon* infinity-corrected objectives with different characteristics. Those more extensively used are reported in Tab. 6.1, with the respective magnifications and *Numerical Aperture* (NA), that is a parameter that indicates the range of angles over which the system can accept light, and is defined as:

$$NA = nsin\alpha \tag{6.1}$$

where n is the refractive index of the medium between the objective and the sample and α is half of the collecting angle of the objective. To reach a large NA, special immersion fluid can be placed between the sample coverslip and the collecting lens of the objective. In particular, oil with refractive index of 1.52 was used.

Table 6.1: Technical characteristics of objectives used in this thesis.

	Objectives			
Magnification	20x	60x	60x	100x
Characteristic	Plan-Fluor	Plan-Fluor	Plan-Apo	S-Fluor
Numerical Aperture	0.5	0.7	1.4	1.3

Three *continuous wave* (cw) lasers (laser diode 408 nm, Ar^+ 488 nm and He-Ne 543 nm) were used as sources for exciting simultaneously the different chromophores and electronic states.
PL signal was then coupled by a multimode optical fiber to three *PhotoMultiplier Tubes* (PMTs) that detected light in three different spectral ranges.
In order to develop the scanning confocal microscope as a spectroscopic tool, several dichroic mirrors were custom designed to be located in the scanning head; their complementary spectral properties allowed PL spectra measurements in the entire visible range.

6.3.2 Photoluminescence Quantum Yield

The photoluminescence QY is defined as the ratio of the number of photons emitted to the number of photons absorbed by a material, and it is used to define how efficiently a fluorophore emits light, and for determining the radiative and non radiative decay constants.
The QY is measured using an integrating sphere, that is a hollow sphere having its inner surface coated with a diffusely reflecting material (typically barium sulfate).
When a light source is placed in an ideal integrating sphere, the light is redistributed isotropically over the sphere interior-surface, regardless of the angular dependence of the emission. Hence, if N_Ω photons are detected over a solid angle Ω, the total number N of photons emitted is given by:

$$N = N_\Omega \frac{4\pi}{\Omega} \tag{6.2}$$

The integrating sphere is particularly useful in the case of molecular and polymeric materials, for which is not appropriate to assume an isotropic emission, since the random distribution of chromophores can lead to anisotropic distribution of the emitting dipole moments. In addition, thin films can present wave-guiding effects.
The experimental setup to determine the QY is composed of a light source at the appropriate wavelength that is directed on the sample (located in the sphere) through a small entrance hole. Then, an optical fiber connect the sphere exit port with a light detection system; immediately in front of the fiber is a baffle coated with the same material of the inner sphere surface to prevent its direct illumination, as it sketched in Figure 6.6.

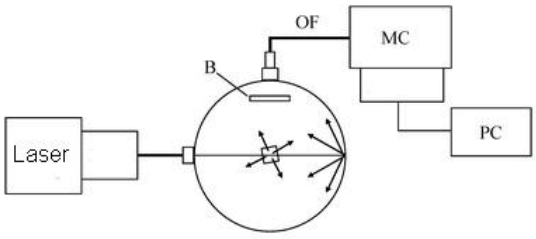

Figure 6.6: Schematic diagram of an integrating sphere instrument for measuring photoluminescence QYs, where MC = monochromator, OF= optical fiber, B=baffle, PC=personal computer (4).

In this thesis, the measure of the photoluminescence QY was made in three steps, following the 'De Mello' method (3). A 15 cm-diameter integrating sphere was used,

that was coupled with either a *cw* dual wavelength 325/442 nm *KIMMON* He-Cd laser, or a *cw* 375 nm *Oxxius* laser diode. The detector was an *Hamamatsu* C7473 *Photonic Multichannel Analyzer* (PMA).

6.3.3 Lasing and Amplified Spontaneus Emission

The lasing thresholds and the ASE properties of small molecules thin films and nanostructured samples were investigated using a 10 Hz repetition rate and 4 ns pulse width Q-switched *Quantel Neodymium ion doped Yttrium Aluminum garnet* (Nd:YAG) laser, having frequency doubled or tripled 532 nm/355 nm wavelengths.
The output intensity of the laser was controlled by inserting calibrated neutral density filters onto the laser beam path and measured using a *Scientech* calibrated laser power and energy meter.
For lasing emission measurements, the laser was focused with a 3x objective lens with 6 cm focal length in a spot of 80 μm, that hit the sample with an angle of about 20^o with respect to the sample substrate normal.
The emitted light was detected by an *Hamamatsu* C7473 *Photonic Multichannel Analyzer* (PMA) placed perpendicularly to the sample substrate, as it is sketched in Figure 6.7. A cut off filter was used to remove the residual pumping laser beam from the signal emitted from the organic laser.

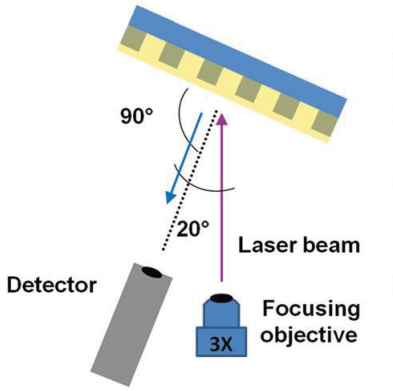

Figure 6.7: Lasing experimental setup.

In the ASE case, a cylindrical lens with 15 cm focal length and an adjustable slit to control the excitation area were used. The resulting stripe-like beam was focused onto the side of the sample at 90^o in respect to the sample's substrate.
When the excitation intensity was sufficiently high, the spontaneously emitted photons

that were waveguided along the stripe region were amplified via stimulated emission. Thus, most of the light was emitted along the direction of the stripe, and in order to efficiently collect this ASE output the fibre bundle was aligned to the sample substrate, and placed close to the sample edge (see Figure 6.8).

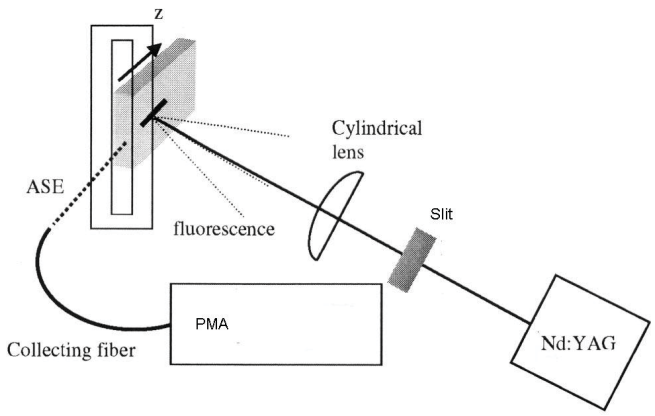

Figure 6.8: ASE setup configuration (5).

In both lasing and ASE measurements, the sample was placed in a small vacuum chamber, were an *Alcatel* Drytel 100 two stage vacuum pump system allowed to obtain 10^{-6} *mbar* vacuum.

Bibliography

[1] N.Sahu et al., *Indian J. Phys.* **86(4)**, 493 (2009) 105

[2] T.Wilson, *Confocal Microscopy*, London: Academic Press (1990) 110

[3] J.C.De Mello et al., *Adv.Mat.* **3**, 231, (1997) 111

[4] K.Suzuky et al, *Phys. Chem. Chem. Phys* **11**, 9850 (2009) xv, 111

[5] K.Geetha et al., *App.Optics* **45(4)**, 806 (2006) xv, 113

7

Conclusions

This PhD thesis was dedicated to the study of the opto-electronic and photonic properties of *Organic Light Emitting Transistors* (OLETs).
In particular, the work was focused on the investigation of light formation and light extraction processes in OLETs presenting a peculiar trilayer configuration, so that the active region of the device consists of the superposition of three organic layers, devoted to the field-effect transport of electrons, holes and to light generation, respectively.
This architecture allows to obtain a superior quantum efficiency for light generation with respect to the one obtained for single-layer device configuration, since it causes a reduction of the exciton-charge and electrode-induced exciton quenching.
Though, a detailed study of the light formation mechanisms and of the optical losses within this structure is mandatory in order to fully unlock the potentiality of OLETs in terms of external quantum efficiency and brightness.
An extensive experimental investigation of these optical and photonic processes was performed in these non-trivial trilayer OLET devices. In particular, a full-channel illuminated OLET was implemented as preferential platform for performing the investigation, given the huge technological potentiality of tens-microns wider light source.
The study of the spatial distribution of light emission was implemented as a standard photonic characterization of OLETs; a one-to-one correlation between experimental characterization and opto-electronic/ photonic simulation activity revealed that the source and drain gold electrodes of OLETs do not influence light extraction and do not cause microcavity effects. Moreover, it was experimentally evidenced that the exciton charge distribution is almost homogeneously spread along the channel length direction and localized only within the recombination layer.
The conclusion of this part of the research was that *Total Internal Reflections* (TIR)

effects prevent a part of light to be extracted from the top of the device.
In order to minimize these light losses and to enhance light collection, a suitable one-dimensional photonic structure (*Distributed Bragg Reflector* (DBR)) was designed and integrated within the device platform.
Indeed, the regular stack of layers that compose the DBR, can induce reflection of light in a certain wavelength range, and thus increase the light extraction by reflecting light that would normally be lost. Furthermore, thanks to its planarity and dielectric properties, a DBR can be implemented in a transistor in substitution to the standard dielectric layer, so that the gate dielectric can be turned into an optically-active component.
This kind of structure was manufacture with two alternating organic dielectric polymers, and integrated into the device structure. The produced transistor preserved good electrical properties, but the photonic effect induced by the DBR was not high enough to modify the electroluminescence angular emission profile of the device. Further experimental work is still going on by introducing high refractive-index contrast materials within the alternating stack.
Then, another interesting typology of unidimensional structure, a *Distributed Feedback* (DFB) structure, was fabricated; in this kind of structure the photonic effect is induced by the spatial variation of the refractive index of the building material.
The grating was made using a blend of silk and stilbene: the first material is an interesting biopolymer that is arousing renewed interest thanks to its excellent mechanical and optical properties, while the second material is a natural dye with very high emission efficiency that was blended with silk to increase its emission properties.
The resulted biocompatible photonic structure showed optically-pumped laser emission, with a lasing threshold two orders of magnitude lower with respect to the one obtained for other biocompatible DFB lasers.
We have pursued in optimizing silk as a photonic active material by obtaining colored silk by means of the natural doping procedure, that consist of feeding directly the silkworm with dye molecules. The stilbene naturally-doped silk was intended for the fabrication of an intrinsic-doped silk DFB structure.
Photoluminescence spectroscopy tools were used to test the effective dye incorporation, and the result of the study was that the naturally-doped silk had *Photoluminescence Quantum Yield* (QY) 30% higher with respect to the undoped silk.
Although this is a good starting point, the obtained QY value was not high enough to utilize this material to fabricate a structure capable of lasing emission; hence, further work is necessary to design more efficiently-incorporated laser dyes.

However, the lasing capability of the optically-pumped silk-based DFB structure is a fundamental step for the realization of novel non-linear detection and imaging schemes which are based on biological organic laser. The silk fibroin photonic structures are intended as key components for the realization of silk fibroin innovative *Lab-on-a-Chip* devices for fluorescence high throughput optofluidic bio-diagnostics.

Acknowledgements

I would like to acknowledge my tutor at the University of Ferrara Prof. Vincenzo Guidi for his help and encouragements.
I thank my tutors from the *Institute for the Study of Nanostructured Materials* (ISMN-CNR) of Bologna, Dr. Stefano Toffanin and Dr. Michele Muccini, and all the people of the *Photonic and Spectroscopy Group*.
I would like to acknowledge the revisers of my thesis, Dr. Francesco Todescato and Dr. Francesco Scotognella, for their interesting and constructive comments.
I thank Dr. Giampiero Ruani, Viviana Biondo, Dr. Raffaella Capelli, Dr. Gianluca Generali, Dr. Eugenio Lunedei, Dr. Giovanna Guidicelli and all my colleagues from Bologna that were very kind and sympathetic to me.
I thank Anna, Assunta, Dr. Tamara Posati, Dr. Valentina Benfenati and the people of the ISOF group, Dr. Camilla Chieco, Dr. Federica Rossi and the people of IBIMET group.
Thanks a lot to Marta, Tanja, Simone, Rick, Marghe and Lauretta for their beautiful friendship, thanks to Edo for the movies and to Lorenz, Chiara and Claudio for the best lunches ever.
I thank my roommates Jesus, Cate and Viola and my ex roommate Stella. Thanks to my beautiful friends from the University, Dany and Anna. Thanks to the wonderful Cecy!!
I would like to thank a lot Gizzu, Jembo, Dobro, Zaochi, Petarda, K, Ari, Gobby, Chiara, Annina, Pava, Misch, Uva and all the friends of *La Saletta* that supported me in this period. I thank Iohe, Iohe, Iohe.
Thanks to my mum and dad, that are so sweet and always ready to help me, and to my beautiful sisters Barbara, Daniela and Annalisa.
Thanks to Udilla, Kikka, Giuliano, Anna, Tonino, my fantastic Gines and Luca. I'm very happy to have you all.